Title

Development of Data Driven Approaches for Understanding Watershed Processes and Environmental Hot Spots and Hot Moments

Author

Chen, Jiancong

Publication Date

2020

Peer reviewed|Thesis/dissertation

Development of Data Driven Approaches for Understanding Watershed Processes and Environmental Hot Spots and Hot Moments

by

Jiancong Chen

A dissertation submitted in partial satisfaction of the

requirements for the degree of

Doctor of Philosophy

in

Engineering – Civil and Environmental Engineering

in the

Graduate Division

of the

University of California, Berkeley

Committee in charge:

Professor Yoram Rubin, Chair
Professor Laurel Larsen
Professor Dennis Baldocchi
Doctor Baptiste Dafflon

Fall 2020

Development of Data Driven Approaches for Understanding Watershed Processes and Environmental Hot Spots and Hot Moments

Abstract

Development of Data Driven Approaches for Understanding Watershed Processes and Environmental Hot Spots and Hot Moments

by

Jiancong Chen

Doctor of Philosophy in Engineering – Civil and Environmental Engineering

University of California, Berkeley

Professor Yoram Rubin, Chair

The study of watershed processes between the hydrosphere, biosphere and atmosphere in response to climate change is critical for modeling dynamics in the hydrologic and biogeochemical cycles. Quantifying the occurrences of environmental hot spots and hot moments (HSHMs) defined as the rare locations or events that exert disproportionate influence over the environment is essential to improve our understanding of watershed dynamics under gradual climate change. This dissertation consists of three different approaches that develop theories and models to statistically characterize HSHMs, improve flux estimation and better identify linkages among aspects of land surface, atmosphere and groundwater interactions.

First, we propose a statistical framework to characterize the spatiotemporal distribution of HSHMs. The statistical framework utilizes indicator random variables to construct a statistical model for HSHMs, which relate the characteristics of HSHMs to the relevant spatial and temporal components. Three categories of HSHMS are identified, including (1) HSHMs defined by only spatial (static) components; (2) HSHMs defined by both spatial and temporal (dynamic) components and (3) HSHMs defined by multiple dynamic components. In order to demonstrate the suitability of the statistical framework, we demonstrate the procedure for constructing the models for each of the category. We further develop a groundwater hydrology example to illustrate the importance of incorporating subsurface heterogeneity in modeling HSHMs occurrences and the corresponding uncertainties. The representation of an HSHM through its spatial and temporal components allows us to relate the HSHM's uncertainty to the uncertainty of its components.

Second, we develop the hybrid-predictive-modeling (HPM) approach to improve estimation of evapotranspiration (ET) and ecosystem respiration (R_{ECO}), especially at mountainous watersheds. The proposed HPM approach integrates meteorological forcing data and remote sensing data to estimate ET and R_{ECO} with the deep learning recurrent neural network long short-term memory as the main driver. HPM can easily incorporate measured data from eddy covariance tower and simulated data from physically-based-models (e.g., Community Land Model). In order to test the performance of HPM, 4 different use cases are developed and tested. Furthermore, we focus on estimating ET and R_{ECO} at the East River Watershed in Colorado and

distinguish the role of small-scale meteorological forcing heterogeneity and vegetation heterogeneity in regulating ET and R_{ECO} dynamics. Estimation results from HPM can then be used as inputs for assessing the occurrences of ecological HSHMs, especially at mountainous watersheds, to improve our understanding of mountainous watershed dynamics.

Third, we recognize the necessity to better understand the intra-annual variability of mountainous watersheds dynamics to better improve our water and resources management. We develop the concept of temporal regimes to identify the sub-annual variability in hydroclimate processes and assess its effects over ET dynamics. We select six mountainous watersheds along the central Rocky Mountain ranges to demonstrate the applicability of temporal regimes. Through the employment of temporal regimes, we identify the temporal boundaries and durations of snow regimes, snowmelt regimes, growing season regimes, monsoon regimes and defoliation regimes from 2005 to 2016. We define within-regime ET as the sub-annual ET contributed from each of the regimes, which enables us to distinguish how the timing and duration of watershed processes regulate ET. High correlation between within-regime ET and regime duration is observed, which suggests intra-annual variability is a major control that regulates the temporal variability of ET at mountainous watersheds. The proposed concept of temporal regimes can further advance of our understanding of how mountainous watersheds evolve under gradual climate change and improve water and energy resources management in the future.

The proposed approaches in this dissertation provide us theories and models to further advance our understanding of watershed dynamics under a rapidly changing environment. Even if we present limited number of examples (e.g., subsurface HSHMs and intra-annual variability of ET), we expect these approaches can be applied towards other ecosystem dynamics.

To my beloved mom and dad
who have been supporting and loving me in their entire life

Contents

List of Figures

List of Tables

Acknowledgements

In the course of my life, I am very grateful for the many people who have made the journey unforgettable and valuable. First and foremost, I would like to thank my Ph.D. advisor, Yoram Rubin, for his guidance throughout my senior year, master year and my Ph.D. years at UC Berkeley. I have learned significantly from him, including the one-minute elevator research talk with the dean of the department ; the morning email exchanges about CE173 and CE202A that integrates my teaching philosophy and the Friday-morning research discussions during which he guides me through the world of stochastic hydrogeology as well as the exploration of environmental hot spots and hot moments. It is his inspiration, care and occasional jokes that have made me this far.

I would also like to the many people at Lawrence Berkeley National Lab, Baptiste Dafflon, Haruko Wainwright, Bhavna Arora, Michelle Newcomer, Nicola Falco, Anh Phuong Tran and Susan Hubbard. Through the years of environmental geophysical meetings and the Watershed SFA meetings, I have received tremendous support from the group that benefit my graduate studies at UC Berkeley. I would also like to thank Professor Laurel Larsen and Professor Dennis Baldocchi for serving on my dissertation committee. I have appreciated your patience and guidance when I shot you an email asking about environmental statistics or eddy covariance methods at Ameriflux sites. Thanks to Professor Sally Thompson and Professor Mark Stacey for serving on my preliminary and qualifying exam committees within the CEE department. And thanks to Shelley Okimoto for having time to listen to my questions and problems. I also want to express my gratitude towards the Jane Lewis Fellowship Committee, the Environmental Division Scholarship Committee at the Society of Mining, Metallurgy and Exploration and the Scientific Focus Area Watershed Functioning project for providing my financial support.

To my fellow brothers and sisters at UC Berkeley, thank you for proving me a love family while I'm away from Panjin. It was Michelle Newcomer, Brad Harken, Heather Savoy, Karina Cucci, and Ching-Fu Chang, who welcomed me to join the group and celebrated all the ups and downs through these years at Berkeley. There is Tianjiao Pu, who renovated 628 Davis Hall later in the season. When I first started my Ph.D., Michelle Newcomer have graduated but she was the one who have guided me through my first year at Berkeley and introduced me to all the other amazing folks at Lawrence Berkeley National Lab. There was also Thanh Thuy Nguyen and Bo Tan, who were willing to check out spicy food on San Pablo Avenue and Bancroft with me. Thank you all.

I would also like to deeply thank my old friends, many of whom started friendship with me since early times. As the first cohort of the Tongji-Berkeley program, I still remember all the joys that we have together playing "80 points", "Who's the murder", and the times we celebrated Chinese New Year together at 1122 University Avenue. Though we are spreading everywhere around the globe now, it is still one of the best memories that I ever have. I also want to thank these people who shared some time with me at Berkeley, Hongxu Ma, Lu Dai, Chenglong Li, Yanghua Duan, Monong Wang, Yuwei Fu, Yadan Zheng, Jiaming Shi and many other dearest friends at Berkeley. I am also fortunate to witness the wedding ceremony of my childhood best friend, Dongye Song, at Dallas. I am also thankful for Qianxiang Sun when he accompanied me to Grand Canyon, Los Angeles, Shanghai, Beijing and many other locations. Even though there are 16 hour differences between us, we still share jokes to keep each other laughing. I also want to thank Huan He, who shared so many secrets with me so that I were able to overcome all the difficulties and darkness that happened during my graduate studies and who have been to the Amoeba music store, Mount Rainer and Olympic National Parks with me. I appreciate the time

that I spent with the 2015-2016 cohort of Environmental Engineering and the mental support that I got from chatting with you.

It is sad that my grandparents were not able to witness my little achievement, and I were not able to go back to China to take my responsibility while fulfilling teaching duties at US. But I am deeply grateful to my parents and my family for their unconditional love and support. It is my parents, 陈树凯 and 袁秀霞, who love me in every second of their life. Without their unconditional love, I could never make this far and become the person I am today.

Chapter 1

Introduction

1.1 Motivations

Environmental Hot Spots and Hot Moments (HSHMs) are defined as the areas (or patches) that show disproportionately higher transport and transformation rates relative to the surrounding area (or matrix) and the short periods of time that show disproportionately transport and transformation rates relative to longer intervening time periods (McClain et al., 2003). HSHMs are important as they represent the unique spatiotemporal components in an ecosystem that potentially carry disproportionately elevated contributions to the whole system. Characterization of HSHM development and occurrence is of great significance for better understanding contaminant transport, biogeochemical cycling, vegetation adaptation and evolvement under extreme conditions, and providing guidance for water resources management and environmental remediation and risk assessments (Arora, Spycher, et al., 2016a; Bernhardt et al., 2017; Henri et al., 2015; Vidon et al., 2010). The occurrences of HSHMs are triggered by various conditions including but not limited to shifts in hydrological dynamics (Vidon et al., 2010), interactions within the biogeochemical cycles (Schiff et al., 2002), occurrences of extreme weather conditions (Sloat et al., 2015), mixing between adjacent ecosystems (Gu et al., 2012). Kuzyakov & Blagodatskaya. (2015) analyzed the potential locations and size of HSHMs in soil related with process rates and microbial activities, and distinguish the significant contributions from rhizosphere, detritusphere, biopores and aggregate surfaces to carbon cycling and microbial activities in soils. Gu et al. (2012) used a numerical modeling approach to simulate how hyporheic exchanges in the riparian zones induced by stream stage fluctuations influences contaminant transport and transformations. Harms & Grimm. (2008) distinguished how the intersection of hydrologic vectors and biologically active regions within the soil profile trigger elevated microbial activities and nutrient chemical cycling at a semi-arid desert landscape. Each of these studies provides unique understanding of HSHM dynamics, however the conditions that trigger HSHMs vary case by case. Thus, it is necessary to find the common similarities and dissimilarities among HSHMs cases, which provides more informative intuition for identification and prediction of HSHMs under different conditions.

As the first step to delineate the combinational effects from multiple processes, Vidon et al. (2010) characterized HSHMs into transport-driven ones and biogeochemical process driven ones. The transport-driven HSHMs focus on HSHM induced by elevated solute fluxes and the biogeochemical process-driven HSHMs are indicated by elevated biogeochemical cycling. This definition further delineated the coupled effects from multiple dynamic processes, however mainly focused on riparian zones and did not incorporate other types of HSHMs beyond nitrogen and carbon. Other research also founds that the interfaces between different systems were also likely to trigger the development and occurrences of HSHMs. Krause et al. (2017) summarized how the ecohydrological interfaces, defined as the dynamic transition zones that develop within ecotones or boundaries between adjacent ecosystems, can substantially alter the movement of water, matter, organisms and energy and hence trigger the occurrences of HSHMs. Examples such as the riparian zones or the hyporheic zones fall into the ecohydrological interfaces, which have been shown to cause HSHM occurrences during the mixing of waters from different sources, such as surface water, groundwater and rainfall. Bernhardt et al. (2017) synthesized the concept of HSHMs and developed the concept of ecosystem control points, which are the areas of the landscape that exert disproportionate influence on the biogeochemical behavior of the system under study. Through their study, they classified control points into permanent, activated, export and transport control points, where permanent control points are landscape patches that possess continuous delivery of reactants that support sustained high rates of biogeochemical activities compared to the surrounding landscape; activated control points are the landscape patches that only support high rates when the delivery of reactants and local conditions are met; export control points are landscape patches where reactants accumulate until a gradient or diffusion threshold is overcome to export and the transport control points are unique for high potential and capacity for water and gas transport within the ecosystem. The smart classification of control points mainly focused on the spatial perspective of Hot Spots, but still did not quantify when Hot Moments are triggered, especially for activated, export and transport control points. Methods to quantify the corresponding processes that lead to the classifications of HSHMs or the control points are still needed. Thus in this study, we will incorporate both the original concepts of HSHMs and the continued expanded definitions, such as ecohydrological interfaces and control points.

Though there is the arising popularity of HSHMs in the field of hydrology, ecohydrology, landscape ecology, biogeochemistry and climate sciences, there are still many missing components that could further advance our understanding of HSHMs and prediction capability due to limited data, unknown processes and large uncertainties. Specifically, as mentioned in Bernhardt et al. (2017), there are currently no studies that focus on developing statistical theories to quantify the uncertainties of HSHMs nor developing data-driven models to predict future occurrences of HSHMs. Processes that govern HSHMs are still quite restricted to certain fields, such as riparian zones, hyporheic zones with limited focus on nitrogen, carbon and other nutrients, which further constrain HSHM theory and model development. Conceptual model uncertainties that arise from the lack of corresponding physical theories for HSHM and the parametric uncertainties that arise from limited data constrain our capabilities to develop statistical models using probability theories and applications. The lack of statistical models to quantify the occurrence of HSHMs further limit our ability to develop early warning systems and predict future occurrences of HSHMs. In addition, as HSHMs can be triggered by various different mechanisms, generic approaches that seek out the similarities are needed for the development of statistical models. For example, HSHMs can be found as the preferential flow

path in the subsurface (Bundt et al., 2001a; Henri et al., 2015), riparian zones or stream corridors (Boulton, 2007; Gu et al., 2012; Vidon et al., 2010), unique landscape in the ecosystem such as hollows and naturally reducing zones (Duncan et al., 2013a; Wainwright et al., 2015); these complicated interactions in hydrology, ecology and biogeochemistry further increase the difficulties in summarizing the similarities and developing statistical frameworks. Spatial heterogeneity within the landscape is a specific source of uncertainties that needs to be incorporated sufficiently in the field of HSHM. Numerical modeling approaches including large scale climate models and reactive transport models are very advantageous as they provide a physical representation of the dynamics that lead to development and occurrences of HSHMs as they incorporate complicated interactions between the hydrosphere and the biosphere. However, these models tend to simplify the topographic structures and subsurface heterogeneity such as the assumption of isotropic homogeneous domain and simplified reaction network due to limited data that are necessary to characterize the spatial variability and computation costs needed to construct finer grids in a numerical model. For example, Dwivedi et al. (2017) develops the first 3-D reactive transport model to simulate HSHMs of nitrogen transformation in the subsurface. This study significantly advances our understanding how riparian corridors control nitrogen speciation and trigger HSHMs. However, they assume a bimodal hydro-stratigraphic units for the subsurface with constant hydrological parameters, including porosity and permeability, which are key parameters for contaminant transport. However, in cases presented in Bundt et al. (2001) and Henri et al. (2015), occurrences of HSHMs are significantly controlled by preferential flow paths and low permeability regions that are caused by the spatial heterogeneity of hydraulic conductivity. In addition, Duncan et al. (2013) concluded the riparian hollows that present as the topographic lowlands can provide up to 99% of nitrogen transformation in certain environment, and thus models that potentially neglect the spatial variability of topography can significantly draw biased conclusions towards the distribution of hot spots. Thus characterization of HSHM occurrences will not only require a well-defined complicated geochemical reaction networks but also incorporate spatial variability in hydrologic parameters and topography.

Other limitations that slow down the advancement of HSHMs come from limited data at larger spatial scales. For example, characterizing the spatial distribution of Hot Spots are essentially important to determine the most influential components within an ecosystem, and is necessary to close the water and energy budget. However, direct data that could be used to quantify HSHM may not be available at such scales, including evapotranspiration and carbon fluxes for HSHMs in ecohydrology, contaminant concentration in biogeochemistry or simply elevated solute fluxes in hydrology. Remote sensing datasets that utilize satellite images provide large scale coverage of the earth surfaces, and can be used to represent the topography (e.g., digital elevation models), vegetation (e.g., normalized differences vegetation index) and many other interpolated attributes including gross primary production through machine learning models. Geophysical techniques, such as electrical resistivity tomography, ground penetration radar, electromagnetic and seismic methods, are related with the soil hydraulic parameters at higher spatial coverage including hydraulic conductivity through petrophysical relations (e.g., Archie's law). These datasets from remote sensing and geophysics cannot be directly used to quantify HSHM development and occurrence, however are very supportive for developing large scale datasets for HSHM attributes of interests such as ET, ecosystem respiration (R_{ECO}), subsurface chemistry and soil moisture dynamics. However, these datasets are difficult to be incorporated into physically based models, which limit their applications for large scale mapping and determination of HSHMs. Thus data-driven models that utilize these data are strongly

needed to provide datasets at high spatiotemporal resolutions with enlarged coverage of the ecosystem being studied.

Evapotranspiration (ET) and ecosystem respiration (R_{ECO}) are key components of ecosystem water and carbon cycles. As the important link between atmosphere-biosphere-hydrosphere compartments, dynamic changes dynamic changes in ET can affect precipitation, soil moisture, and surface temperature, leading to uncertain feedbacks in the environment (Jung et al., 2010; Seneviratne et al., 2006; Teuling et al., 2013). R_{ECO} describes the sum of autotrophic respiration and respiration by heterotrophic microorganisms in a specific ecosystem and plays a vital role in the response of terrestrial ecosystem to global change (Jung et al., 2017; Reichstein et al., 2005; Xu et al., 2004). HSHMs of ET and R_{ECO} have disproportionate contributions to the global scale water, energy and carbon balances as well as vegetation evolutions under climate change. Quantifying the occurrences of HSHMs of ET and R_{ECO} is not only necessary to improve our predictability of ecosystem evolution, but also significant for us to develop strategies and approaches to improve resources management with ongoing climate change and extreme climate conditions.

Current methods that focus on estimating ET, R_{ECO} and other ecosystem fluxes include direct sampling approaches such as the eddy covariance method and chamber method; physically-based models that numerically solve differential equations; and data-driven models that can integrate meteorological forcing data and remote sensing datasets. However, it is difficult to deploy eddy covariance towers to capture dynamics happening at different parts of a watershed with high installation and maintenance costs. Ground based flux chambers may affect the microclimate of the surrounding environment leading to decrease in data quality. Physically-based models might be biased due to the underlying assumptions. Data-driven models are advantageous as they could integrate datasets at different spatiotemporal scale, however still heavily rely on data quality and spatiotemporal availability. Thus it is still necessary to develop hybrid approaches that could integrate direct measurements and mechanistic models with data-driven methods to advance our predictability of ecosystem flux and scalar estimation.

The development of statistical frameworks and the increasing availability of data and model simulation results provide revenues to improve our understanding of watershed dynamics and HSHMs occurrences. Still, climate change poses difficulties into capturing and modeling HSHM phenomena due to its uncertain effects on hydrology, ecology and biogeochemistry in ecosystems. Studies have found significant changes in snowmelt dynamics in western US mountainous watersheds (Blankinship, 2014; Rauscher et al., 2008; Stocker et al., 2013), which causes increasing occurrences of fore-summer drought (Sloat et al., 2015) and multi-year droughts (Avanzi et al., 2019; Rungee et al., 2019) that further result in changes in evapotranspiration and ecosystem carbon fluxes. Temperature increases due to climate change also alter the percentage between snow precipitation and rainfall precipitation, and have been found to have significantly impacts over streamflow fluctuations and soil moisture storage in the subsurface and potentially alter the earth surface energy balance (Jasechko et al., 2016; Foster et al., 2016; Rood et al., 2008). The effects caused by climate change have significant impacts over hydrologic dynamics and ecosystem functioning within an ecosystem; however the corresponding HSHMs induced by such changes are still uncertain. Characterization of the corresponding of HSHMs in ET, R_{ECO} and other fluxes within an ecosystem will also rely on better understanding of how watershed hydrologic dynamics and ecosystem functioning evolve under climate change.

1.2 Research Objectives

Identification and prediction of HSHMs rely on data and improved understanding of the ecosystem dynamics. The overarching goal of this dissertation is to develop approaches that overcome the aforementioned challenges. Specifically, this dissertation aims to contribute with the following research objectives,

a. How can we incorporate statistical concepts into modeling HSHMs and the associated uncertainties?

b. How can we estimate important and relevant parameters and attributes for HSHMs when direct data are not available, in particular evapotranspiration (ET) and ecosystem respiration (R_{ECO})?

c. How does quantification of HSHMs further advance our understanding of hydrological and ecological dynamics and what are the implications for inter-annual and intra-annual variability of these processes under climate change?

1.3 Scope of the Dissertation

Following the motivations discussed in previous sections, this dissertation centers around HSHMs, from identifying the key processes; quantifying uncertainties of HSHMs; predicting key attributes when data are sparse to furthering our understanding of ecohydrological processes. The following chapters are organized as follows,

Chapter 2 introduces a statistical formulation to quantify HSHMs and the associated uncertainties. The major novelty in this approach is to use indicator random variable to decompose complex HSHMs dynamics into relevant processes and attributes, which enables us to relate HSHMs' uncertainties to the uncertainty of their components. Additionally, it provides a formulation, well established by Bayesian statistics theories, for conditioning the HSHM probabilities on in-situ measurements as well as on information borrowed from ecohydrologically similar sites. This approach enables us to define HSHMs based on the contributing factors, including HSHM defined by static contributors; HSHMs defined by dynamic indicators and HSHMs requiring the coupling of static and dynamic contributors. For each category, the HSHM stochastic formulations is expressed in terms of the stochastic formulations of the relevant contributors. Groundwater HSHMs that occur in the subsurface are studied using the proposed framework, where we derive, analyze and demonstrate the process of developing such framework, assessing HSHM uncertainties and identifying the key attributes.

Chapter 3 describes a Hybrid Predictive Modeling (HPM) approach that is used to estimate key attributes and dynamics important for HSHM applications, such as evapotranspiration (ET) and ecosystem respiration (R_{ECO}), which are difficult to obtain over large spatiotemporal domain. HPM integrates eddy covariance measurements and mechanistic model based simulation results for model development and takes meteorological forcing data (i.e., air temperature, precipitation and solar radiation) and remote-sensing derived data (i.e., normalized differences vegetation index; NDVI) to estimates ET and R_{ECO} under various climate conditions. HPM utilizes deep learning models, such as long short-term memory (LSTM), to establish relationships among ET, R_{ECO} and input features (i.e., meteorological attributes and NDVI). Effectiveness of HPM are investigated at FLUXNET sites and the East River Watershed in Colorado. We demonstrate the HPM approaches through various Use Cases, including: estimating ET and R_{ECO} over time; data-driven HPM for estimation over space; physical-model-driven HPM for estimation over space; and HPM applications at the East River Watershed. With the aid of HPM, ET and R_{ECO} estimation become available, which enables us to assess the corresponding ecological HSHMs. Further, HPM-based estimations are extremely helpful for mountainous watersheds, where ET and R_{ECO} data are typically difficult to obtain. We also assess how small-scale (i.e., hillslope

scale) heterogeneity factors (e.g., vegetation type) control ET and R_{ECO} dynamics at the East River Watershed.

Chapter 4 proposes the method of temporal regimes to quantify the temporal variability of biogeochemical and ecohydrological dynamics and assess environmental hot moments. Temporal regimes are defined as a specific period of time when watershed dynamics are controlled by a certain set of relevant attributes (i.e., hydroclimate or biogeochemical) and the joint distributions of these attributes are statistically different compared to other temporal regimes. Hydroclimate attributes, such as air temperature, soil temperature, precipitation and radiation, are used to identify hydroclimate regimes, and assess the intra-annual variability of ET. Biogeochemical attributes, such as concentration of chemical elements, are used to determine the biogeochemical regimes and assess the corresponding environmental hot moments. The method of regimes is advantageous as it quantitatively describes the intra-annual variability of biogeochemical and ecohydrological dynamics and assesses the contributions from each regime to the annual cycle, which provides significant insights for analyzing the limiting factors for inter-annual dynamics. This approach is applied at mountainous watersheds along the Central Rocky Mountain to analyze the intra-annual variability of ET, including multiple FLUXNET sites and East River Sites.

Finally, chapter 5 summarizes the key findings and conclusions from the previous chapters and generalizes the major contributions from this dissertation to the field of environmental HSHMs. Appendices at the end of this dissertation include necessary derivations and discussions mentioned in this dissertation.

Chapter 2

Statistical Characterization of Environmental Hot Spots and Hot Moments with Applications in Groundwater Hydrology

2.1 Introduction

In this chapter, we present a novel statistical framework for analyzing environmental hot spots and hot moments (HSHMs) and the uncertainties. Environmental hot spots and hot moments (HSHMs) were originally defined as rare locations or events that support or induce disproportionately high activity levels (e.g., chemical reaction rates) compared to surrounding areas or preceding times (McClain et al., 2003). Vidon et al. (2010) further classified HSHMs into either transport-driven or biogeochemically-driven HSHMs, based on the mechanisms causing the HSHMs. Bernhardt et al. (2017) derived the concept of ecological control points (CPs) related to HSHMs, defining CPs as areas of the landscape that exert a disproportionate influence on the biogeochemical behavior of an ecosystem under study. These definitions have mainly focused on HSHMs related to elevated biogeochemical activities triggered by hydrological or biogeochemical processes, or a confluence of both processes. The concept of HSHMs is also used in climate science, where it is related to elevated greenhouse gas emissions or specific locations that are subject to extreme natural hazards (e.g., sea-level rise, floods, hurricanes, or earthquakes) caused by climate change (Arora et al., 2020; Shrestha & Wang, 2018). Further, Henri et al. (2015) related HSHMs to locations experiencing elevated environmental risks and developed the incremental lifetime cancer risk (ILCR) model to quantify the effects of hot spots on human health. Overall, these studies have focused on quantifying the consequences of HSHMs by way of environmental risks and costs while also emphasizing the importance of characterizing the occurrences of environmental HSHMs. In this chapter, we combined these definitions such that, henceforth, HSHMs are referred to as rare locations or events that could exert a disproportionate influence on an ecosystem and which are associated with heightened health or environmental risks.[1]

Characterizing HSHMs dynamics is useful for understanding hydrological and ecological dynamics related to nutrient cycling, contaminant transport, and accurate assessment of

[1] This chapter is based on a manuscript submitted to the journal of Hydrology and Earth System Science

ecosystem and hydrological perturbations under climate change. For example, Duncan et al. (2013) demonstrated that riparian hollows, which represent less than 1.0% of the landscape but contribute to more than 99% of total denitrification of a whole catchment area, function as hot spots. Additionally, wetlands have been considered biogeochemical hot spots for mercury mobilization and methylation production since the early 1990s (Vidon et al., 2010). The spatial patterns of methylmercury (MeHg) hot spots in wetlands can vary significantly across space. Indeed, the MeHg concentration at the interface between upland and peatland can be 100 times greater than a different patch within the same wetland (Mitchell et al., 2008). In managed temperate peatlands, drainage ditches that account for less than 5% of a land area can act as hot spots and can contribute to over 84% of total greenhouse gas emissions (Teh et al., 2011). Ecohydrological interfaces, the dynamic transition zones between adjacent ecosystems, substantially influence migration of water, nutrients, and organisms and hence triggers occurrences of HSHMs (ADD KRAUSE CITATION). Though riparian zones and hyporheic zones only account for a small percentage of ecosystem, these interfaces significantly contribute to nitrogen and carbon cycling between the biosphere, hydrosphere and atmosphere. The disproportionate contributions from HSHMs to the overall hydrological and ecological dynamics strongly indicate the necessities of characterizing HSHMs.

Quantifying HSHMs has also been recognized as important for assessing the consequences after catastrophes and the environmental risks, such as water crises (Baum et al., 2016) or nuclear disasters (Kamidaira et al., 2018; Morino et al., 2011; Showstack, 2014). The migration of contaminants after a catastrophe creates zones of different toxicity levels and poses disproportionate threats to the surrounding natural and urban environment. In contrast, existing HSHMs caused by the leakage of nuclear waste or heavy metals largely influence site characterization needs and the remediation efforts needed to minimize environmental and economic losses (Bao et al., 2014; Harken et al., 2019). Thus far, studies in this area have focused on the environmental implications and usefulness of characterizing HSHMs. However, special tools for characterizing and modeling HSHMs are still needed, such as physically-based and statistical models, which can provide additional benefits to capture the disproportionate effects of an HSHM on a whole ecosystem.

Reactive transport models have been used to understand and predict HSHMs. Dwivedi et al. (2017), for instance, developed a 3-D high-resolution numerical model to investigate whether organic-carbon-rich and chemically-reduced sediments located within the riparian zone act as denitrification hot spots. Their study demonstrated a significantly higher potential (~70%) of the naturally reduced zones (NRZs) to remove nitrate than the non-NRZ locations. Arora et al. (2016) used a 2-D transect model and showed that temperature fluctuations constituted carbon hot moments in a contaminated floodplain aquifer that resulted in a 170% increase in annual groundwater carbon fluxes. Gu et al. (2012) developed a Monte Carlo reactive transport approach and discovered how denitrification HSHMs are triggered by river stage fluctuations. Despite these studies, clear statistical conventions of HSHMs are missing, which significantly limits the transferability of these approaches. In fact, distinguishing HSHMs based on statistical formulations has been identified as a major gap in the current HSHM literature (Bernhardt et al., 2017; Arora et al., 2020).

Statistical approaches offer multiple advantages for furthering the HSHM concept. First, statistical approaches can develop common formulations that integrate biogeochemical and hydrogeological knowledge from multiple HSHMs studies. Once developed, these formulations can be readily applied to identify HSHMs at similar sites. Second, statistical approaches can

easily incorporate categorical indicators that represent spatial heterogeneity and quantify the uncertainty of HSHM occurrences tied to these features. Such approaches can be used as predictive tools to estimate future occurrences of HSHMs, and provide an alternative to computationally-expensive high-resolution mechanistic models. This would greatly aid decision-makers in identifying scenarios (e.g., changes in the climate or in environmental conditions) that increase risks associated with the occurrence of HSHMs phenomena.

Statistical concepts and models have been widely applied in hydrology and hydrogeology, including but not limited to modeling flow and contaminant transport, quantifying subsurface heterogeneity and the associated uncertainties, developing strategies for site characterization, and providing informative priors for ungauged watersheds. For example, Rubin (1991) described a Lagrangian approach to obtain the summary statistics of contaminant concentrations in the subsurface, including mean, variance and covariance. These statistical moments are necessary to define the probability distribution of contaminant concentrations over space and time, and thus, quite useful for quantifying HSHMs. Statistical terms, such as concentration mean and variance, concentration cumulative density function (CDF), exceedance probabilities, and exposure time CDF also provide significant guidance to assess the environmental risks associated with HSHMs (Rubin et al., 1994). Although there is a lack of conventional statistical approaches in current HSHM studies, we believe it is feasible and valuable to develop statistical formulations to characterize HSHMs dynamics.

Successful characterization of HSHMs through physically-based models or statistical approaches relies on experts' knowledge of a site, intensive field characterization, and possibly continuous field sampling to provide the data to develop and validate these approaches. Understandably, intensive site characterization and long-term sampling can be quite challenging due to the associated costs and efforts. Thus, it is necessary to develop approaches that could simplify but still effectively and efficiently represent the underlying structure of HSHMs. In this regard, indicator statistics that take value 0 or 1 depending on whether a HSHM occurs or not, can be useful, on two counts. First, it is suitable for modeling bimodal situations. For example, a situation where an event might or might not take place. Indicators are also appealing in applications because of the sparsity of the Bernoulli probability model. Indicator statistics have previously been applied to model flow and transport phenomena in groundwater (Rubin & Journel, 1991), where indicators were used to model the spatial distribution in a sand-shale formation. Rubin (1995) applied an indicator spatial random function to model contaminant flow and transport in bimodal heterogeneous formations. Ritzi et al. (2004) developed a hierarchical architecture to represent the spatial correlation of permeability in cross-stratified sediment using indicator statistics. Wilson and Rubin (2002) and Bellin and Rubin (2004) used indicator statistics that describe whether particles were captured by sampling points to characterize the level of aquifer heterogeneity. These studies suggest that the simplification of the system's structure through indicator formulation significantly lowers the number of measurements needed, and thus reduces the costs associated with site characterization, while maintain sufficient information for modeling flow and contaminant transport. In addition, indicator formulation is useful in that it allows to aggregate multiple variables (e.g., all HSHM relevant variables) into a single random variable. Instead of characterizing the full distributions of each parameter, indicator formulation only requires knowledge of the critical condition for relevant parameters. Such indicator random variable (RV) will take a value of 1 if the critical conditions are met, regardless of the original distribution for the parameters. With indicator formulations for HSHMs, researchers can focus on identifying the most relevant parameters for

HSHMs quantification, which can significantly reduce the efforts and costs required for intensive site characterization.

In this chapter, we present the statistical framework to quantify HSHMs occurrences and uncertainties. The developed statistical framework can help determine HSHM-occurrence probabilities under user-defined scenarios. It can also be used for estimating future occurrences of HSHMs. Based on the mechanisms that drive HSHM occurrences, we determined three categories of HSHMs: (1) those triggered only by spatial (static) contributors, (2) those triggered by both spatial (static) and temporal (dynamic) contributors, and (3) those triggered by multiple dynamic contributors. Within each category, cases from existing studies were used to illustrate the procedures for constructing the statistical formulations. We focused specifically on HSHMs applications in groundwater, where we derived analytical solutions for the statistical formulation of HSHMs and analyzed the probabilities of HSHM occurrences and their corresponding levels of uncertainty using synthetic case studies.

2.2 Statistical Formulation of HSHMs

HSHMs represent rare places or events with increased hydrobiogeochemical rates or fluxes that are significantly elevated above the background condition, thus exerting disproportionate influences over an ecosystem's dynamics. We define $(\boldsymbol{\Omega}^*, t^*)$ as the jointly distributed RVs for HSHMs, and $\boldsymbol{\Omega}^*$ and t^* represent the spatial components of hot spots and temporal components of hot moments, respectively. An indicator random variable, $I_{HSHM}(\boldsymbol{\Omega}^*, t^*)$, is used to represent whether the pair $(\boldsymbol{\Omega}^*, t^*)$ is an HSHM or not. If there exists a pair of $(\boldsymbol{\Omega}^*, t^*)$ that satisfies the critical conditions of an HSHM, $I_{HSHM}(\boldsymbol{\Omega}^*, t^*) = 1$, and the pair $(\boldsymbol{\Omega}^*, t^*)$ represents the location and time of the HSHM.

Following the original definition by McClain et al. (2003), in our method, $I_{HSHM}(\boldsymbol{\Omega}^*, t^*)$ can take the value of 0 or 1, depending on the concentration or reaction rate measured at $(\boldsymbol{\Omega}^*, t^*)$, respectively:

$$I_{HSHM}(\boldsymbol{\Omega}^*, t^*) = \begin{cases} 1, if\ C(\boldsymbol{x}, t^*) > C_{th};\ \boldsymbol{x} \subseteq \boldsymbol{\Omega}^* \\ 0, \quad otherwise \end{cases}, \text{ or}$$

$$I_{HSHM}(\boldsymbol{\Omega}^*, t^*) = \begin{cases} 1, if\ R(\boldsymbol{x}, t^*) > R_{th};\ \boldsymbol{x} \subseteq \boldsymbol{\Omega}^* \\ 0, \quad otherwise \end{cases}. \tag{2.1}$$

where $C(\boldsymbol{x}, t^*)\ and\ R(\boldsymbol{x}, t^*)$ are the concentration and reaction rate at the position $\boldsymbol{x}$ and time t^*, respectively. $C_{th}\ and\ R_{th}$ represent the concentration and reaction rate thresholds, respectively. Defining indicators with concentration, or reaction rate depends on the target of HSHM. Similar definitions can be introduced based on the regulatory limits or the interest of the investigator, using the mean concentration or the solute mass within the volume $\boldsymbol{\Omega}^*$.

The critical values, C_{th} and R_{th}, are key to an effective application of the above framework and should be determined based on the specific scenario. For example, for contaminants that are associated with significant environmental or health risks (e.g., nuclear waste or a cancerous substance), $C_{th} = 0$ can be used so that the HSHM will be triggered as soon as there is the presence of such contaminants. As an alternative, a limit in the total accumulated mass within hot spots may be set, such as suggested by EPA (USEPA, 2001), but in this case the definition (1) of the indicators should be modified. For water quality parameters, $C_{th} = MCL$ can be assigned, where MCL represents the maximum concentration limit for a specific solute. Alternatively, $C_{th} = C^*$ can be used in cases where C^* is chosen based on the experts' domain knowledge. This approach requires that such decisions be made before deriving any solutions to determine HSHM occurrences.

Given the definition of $I_{HSHM}(\boldsymbol{\Omega}^*, t^*)$, we observe that $I_{HSHM}(\boldsymbol{\Omega}^*, t^*)$ follows a Bernoulli distribution, such as $I_{HSHM}(\boldsymbol{\Omega}^*, t^*) \sim Bernoulli(< I_{HSHM}(\boldsymbol{\Omega}^*, t^*) >)$, where $< . >$ is the operator indicating the ensemble mean of the indicator represented as a random variable. An important characteristic of the Bernoulli distribution is that all the statistical moments of the RV $I_{HSHM}(\boldsymbol{\Omega}^*, t^*)$ can be expressed as a function of the ensemble mean $< I_{HSHM}(\boldsymbol{\Omega}^*, t^*) >$. For example, the variance is given by $var\big(I_{HSHM}(\boldsymbol{\Omega}^*, t^*)\big) = < I_{HSHM}(\boldsymbol{\Omega}^*, t^*) > * (1 - < I_{HSHM}(\boldsymbol{\Omega}^*, t^*) >)$.

Characterization of the spatiotemporal distribution of $I_{HSHM}(\boldsymbol{\Omega}^*, t^*)$ requires the incorporation of the mechanisms that govern the development and occurrence of HSHMs. However, the direct quantification of $< I_{HSHM}(\boldsymbol{\Omega}^*, t^*) >$ can be difficult in both time and space domain. Thus, to facilitate this undertaking, we propose to decompose $I_{HSHM}(\boldsymbol{\Omega}^*, t^*)$ into a Type-A (static) indicator random variable—$I_s(\boldsymbol{\Omega}^*)$—and a Type-B (dynamic) indicator random variable—$I_d(\boldsymbol{\Omega}^*, t^*)$. Definitions of the Type-A and Type-B contributors are as follows:

- **Type-A (Static) Contributors.** This category covers discrete spatial elements (and their associated critical states) that could trigger an HSHM once they come into contact with Type-B contributors (see discussion below). Critical states are the range of values needed to trigger an HSHM (either in standalone mode or when coupled with Type-B contributors).
- **Type-B (Dynamic) Contributors**. This category covers dynamic variables (and their associated critical states) that could trigger an HSHM once they come into contact with Type-A contributors. This category includes, for example, mass transport variables. It also includes changes in local hydrological and environmental conditions (e.g., water table fluctuations). The displacement of solutes in the subsurface (trajectories and travel times) from below- and above-ground processes are prime examples of Type-B contributors.

As an example, naturally reduced sediments (Type-A contributor) occurring next to the river corridor at Rifle, Colorado were identified as carbon export hot spots (Arora et al., 2016; Wainwright et al., 2015). Studies showed that these hot spots were triggered when temperature conditions (Type-B contributor) varied in the subsurface, resulting in a 170% increase in groundwater carbon export from the floodplain site to the river (Arora et al., 2016). In another example, topographic features, such as the backslope of the lower montane hillslope (Type-A contributor) within the East River Watershed (Hubbard et al., 2018), were considered denitrification hot spots, which can have a significant impact on the watershed-scale nitrogen loss pathway. These hot spots were often triggered by spring snowmelt and storm events (Type-B contributor).

Both indicators of the Type-A and Type-B contributors assume a value of either 0 or 1. If one of these indicators takes a value of 1, it can be viewed as an HSHM contributor. However, for an HSHM to occur, both indicators must have a value of 1 at the same location and time. This idea can be expressed as follows:

$$\begin{aligned} P(I_{HSHM}(\boldsymbol{\Omega}^*, t^*) = 1) &= P(I_s(\boldsymbol{\Omega}^*) = 1, I_d(\boldsymbol{\Omega}^*, t^*) = 1) \\ &= P(I_s(\boldsymbol{\Omega}^*) = 1) * P(I_d(\boldsymbol{\Omega}^*, t^*) = 1 | I_s(\boldsymbol{\Omega}^*) = 1) \\ &= P(I_d(\boldsymbol{\Omega}^*, t^*) = 1) * P(I_s(\boldsymbol{\Omega}^*) = 1 | I_d(\boldsymbol{\Omega}^*, t^*) = 1). \end{aligned} \quad (2.2)$$

In equation (2.2), $P(I_d(\boldsymbol{\Omega}^*, t^*) = 1 | I_s(\boldsymbol{\Omega}^*) = 1)$ is the probability of observing a dynamic HSHM within $\boldsymbol{\Omega}^*$, at time t^* conditional to the fact that $\boldsymbol{\Omega}^*$ is a static hotspot and $P(I_s(\boldsymbol{\Omega}^*) = 1 | I_d(\boldsymbol{\Omega}^*, t^*) = 1)$ is defined similarly. Based on the mechanisms of HSHMs, we can classify HSHMs into three different categories as discussed below. These categories can be

used to guide the application of the above statistical framework in a variety of complex HSHM scenarios, and they can also be used to develop analytical or numerical solutions for both static and dynamic indicators. Furthermore, the three categories provide guidance on using indicator approaches for both transport-driven and biogeochemically-driven HSHMs, as discussed by Vidon et al. (2010).

2.2.1 HSHMs induced by type-A (static) indicators

In this section, we consider HSHMs that are defined by static indicators only (Figure 2.1a). This list can include zones of high, persistent concentration and reactivity that are due to the subsurface or the ecosystem's unique hydrological and biogeochemical properties (e.g., microsites). For example, the accumulation of contaminants in the subsurface (e.g., the high nuclide concentration in the subsurface at the Hanford Nuclear Production Site, Washington) could lead to the evolution of persistent, high reactivity zones. An aquifer's heterogeneity is another example that could distinguish certain regions with high reactivity from surrounding areas (Loschko et al., 2016). Such high reactivity spots (hereafter denoted as $\boldsymbol{\Omega}^*$) can be characterized by static indicator RVs due to the persistence of high concentration or reactivity. The static indicators are defined as follows:

$$I_{HSHM}(\boldsymbol{\Omega}^*) = I_s(\boldsymbol{\Omega}^*) = \begin{cases} 1, & if\ Z(\boldsymbol{\Omega}^*) \subseteq Z_s^* \\ 0, & otherwise \end{cases}, \tag{2.3}$$

where $Z_s{}^*$ represents the conditions needed to trigger a hot spot at $\boldsymbol{\Omega}^*$, and $Z(\boldsymbol{\Omega}^*)$ represents the corresponding local conditions at $\boldsymbol{\Omega}^*$.

2.2.2 HSHMs induced by type-A (static) and type-B (dynamic) indicators

HSHMs can also result from dynamic processes encountering specific conditions at $\boldsymbol{\Omega}^*$ (Figure 2.1b). This is the situation described by equation (2.2), where the static indicators are determined first, and then used jointly with the dynamic indicators for complete HSHM characterization. For example, Bundt et al. (2001) concluded that preferential flow paths are biological hot spots for soil microbial activities. Preferential flow paths in such cases are candidate hot spot locations ($\boldsymbol{\Omega}^*$). Meanwhile, dynamic factors, such as snowmelt, control contaminant transport via the preferential flow paths, and thus, they determined the hot moment component. The duration of these events presents the temporal component of the HSHM.

For an HSHM induced by both static and dynamic indicators, the static locations are selected first, based on their HSHM-related properties. After this, we can focus on characterizing the HSHM dynamics as they relate to the relevant locations. A selected location, $\boldsymbol{\Omega}^*$, could become an HSHM site based on characteristics defined through the following static and dynamic indicators, respectively:

$$I_s(\boldsymbol{\Omega}^*) = \begin{cases} 1, & if\ Z_s(\boldsymbol{\Omega}^*) \subseteq Z_s^* \\ 0, & otherwise \end{cases}, \tag{2.4}$$

$$I_d(\boldsymbol{\Omega}^*, t^*) = \begin{cases} 1, & if\ Z_d(\boldsymbol{\Omega}^*, t^*) \subseteq Z_d^* \\ 0, & otherwise \end{cases}, \tag{2.5}$$

$$I_{HSHM}(\boldsymbol{\Omega}^*, t^*) = \begin{cases} 1, & if\ Z_s(\boldsymbol{\Omega}^*) \subseteq Z_s^*, and\ Z_d(\boldsymbol{\Omega}^*, t^*) \subseteq Z_d^* \\ 0, & otherwise \end{cases}, \tag{2.6}$$

where Z_d^* represents the critical conditions needed to characterize a hot moment, and $Z_d(\boldsymbol{\Omega}^*, t^*)$ represents the local condition at t^* and $\boldsymbol{\Omega}^*$. The statistical model of $I_{HSHM}(\boldsymbol{\Omega}^*, t^*)$ can be expressed using the statistical models of I_s and I_d, as shown in equation (2.2).

2.2.3 HSHMs induced by multiple type-B (dynamic) indicators

Various dynamic processes could jointly evolve into an HSHM (Figure 2.1c). Unlike the previous scenarios where static locations can be determined through known characteristics

provided by geophysical or other types of data, HSHMs can also emerge due to the confluence of dynamic processes. This situation is described in equation (2.7). For example, Gu et al. (2012) analyzed how streamflow fluctuations could trigger a nitrogen HSHM. In their example, the dynamics of the streamflow and groundwater controlled the transport and mixing of the chemical reactants, thus triggering the occurrences of HSHMs. For this case, the static locations of $\boldsymbol{\Omega}^*$ are determined by the confluence of multiple dynamic processes.

We can consider the case where an HSHM is predicated on m dynamic processes, d_j, where $I_{d,j}(\boldsymbol{\Omega}^*, t^*)$ is the dynamic indicator representing the action (or inaction) of d_j at $\boldsymbol{\Omega}^*$ and time t^*. The hot spot location $\boldsymbol{\Omega}^*$ is determined by the confluence of all dynamic processes at time t^*. These dynamic processes are not necessarily independent. Therefore, generally, the statistical model for the comprehensive dynamic indicator (which covers all dynamic contributors) assumes the following form:

$$P[I_d(\boldsymbol{\Omega}^*, t^*) = 1] = P\left[I_{d,1}(\boldsymbol{\Omega}^*, t^*) = 1, \dots, I_{d,m}(\boldsymbol{\Omega}^*, t^*) = 1\right]. \tag{2.7}$$

In situations where the various dynamic contributors can be viewed as independent (e.g., Destouni & Cvetkovic, 1991)—where the reactants travel via different paths—then, assuming independence, we can state that

$$P(I_d(\boldsymbol{\Omega}^*, t^*) = 1] = \prod_{j=1}^{m} P\left[I_{d,j}(\boldsymbol{\Omega}^*, t^*) = 1\right]. \tag{2.8}$$

Here, the mean of the dynamic indicator becomes

$$< I_d(\boldsymbol{\Omega}^*, t^*) > = \prod_{j=1}^{m} < I_{d,j}(\boldsymbol{\Omega}^*, t^*) >. \tag{2.9}$$

If $\boldsymbol{\Omega}^*$ is a hot spot, then equation (2.9) also defines $< I_{HSHM}(\boldsymbol{\Omega}^*, t^*) >$. However, if $\boldsymbol{\Omega}^*$ is not a hot spot, then we need to resort to coupled statistical modeling, as suggested by equation (2.2).

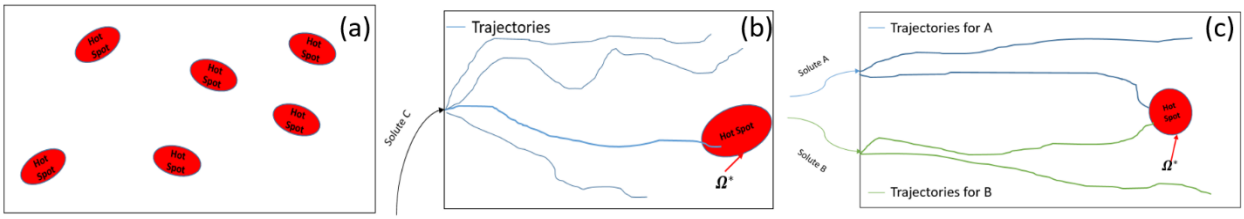

Figure 2.1 Identified categories of HSHMs. Panel (a) presents HSHMs resulting from only Type-A (static) indicator; panel (b) presents HSHMs resulting from coupled action (static + dynamic) and panel (c) presents HSHMs resulting from multiple (two) dynamic indicators

2.3 Examples of the statistical formulation of HSHMs with case studies

In this section, we selected numerous examples from published research to present how our approach can be used to derive statistical representations for the HSHMs investigated in these studies. We grouped these studies into three categories based on the similarities of their underlying HSHM mechanisms, as described in section 2.2. We also characterized the environmental risk levels and impacts based on their target HSHMs. Table 1 presents a summary of these cases. The indicator formulation is constructed in sections 2.3.1–2.3.3.

Reference	HS Location	Category	Seasonality	Environmental Risk	Causes	Impact	Static Mechanism	Dynamic Mechanism	HSHM Action	Metrics for threshold	Equation(s)
Examples of static only mechanisms											
Wainwright et al. (2015)	Naturally reducing zone	Subsurface	--	Short-term low risk; long-term high risk	Anthropogenic + Natural	Negative	Mineralological and lithological differences	--	Vanadium, uranium, metallic minerals	Concentration	(3)
Sassen et al. (2012)	Reactive facies	Subsurface	--	Short-term low risk; long-term high risk	Anthropogenic + Natural	Negative	Lithological differences	--	Uranium and other isotopes	Concentration	(3)
Examples of static + dynamic mechanism											
Andrews et al. (2011)	Shale hill	Subsurface + Surface	Snowmelt and fall flushing periods	Low risk	Natural	Neutral	South-facing concave hillslopes	Snowmelt and fall flushing periods	Organic carbon	Concentration	(4) – (6)
Henri et al. (2015)	Preferential flow path	Subsurface	--	High risk	Anthropogenic	Negative	Subsurface heterogeneity	Contaminant transport and travel time distribution	Chlorinated compounds	Concentration	(4) – (6)
Duncan et al. (2013)	Microtopography	Surface	Unimportant	High risk	Natural	Positive	Riparian hollows	Transport and retention of reactants	Nitrogen	Concentration or reaction rate	(4) – (6)
Arora et al. (2016)	Naturally reducing zone-induced transport	Subsurface	Temperature and water table fluctuation	Low risk	Anthropogenic + Natural	Neutral	Naturally reduced zones	Temperature and water table fluctuation	Carbon fluxes	Concentration or reaction rate	(4) – (6)
Examples of multiple dynamic mechanisms											
Hill et al. (2000)	Riparian zone	Subsurface	--	High risk	Natural	Positive	Interfaces in the riparian zone	Supply of electron donor and acceptor from flow transport	Nitrogen and carbon	Concentration or reaction rate	(7) – (9)
Mitchell et al. (2008)	Peatlands	Subsurface + Surface	Summer periods	High risk	Natural	Negative	Upland-peatland interfaces induced by flow	Interactions between upland and peatland flow	Methylmercury	Concentration	(7) – (9)
Frei et al. (2012)	Microtopography	Surface	--	Neutral	Natural	Neutral	Flowpaths induced by microtopography	Biogeochemical evolution along flow paths	Organic matter and nitrogen	Concentration or reaction rate	(7) – (9)
Gu et al. (2012)	Mixing zones	Subsurface + Surface	River discharge + Water table fluctuation	High risk	Natural	Positive	Mixing zones caused by river stages	Interaction between surface water and groundwater	Nitrogen	Concentration or reaction rate	(7) – (9)

Table 2.1 Example cases considered in this chapter for constructing the statistical formulation of HSHM.

2.3.1 HSHMs triggered by static contributors only

In this section, we use Wainwright et al. (2015) as an example to illustrate our process to construct $I_{HSHM}(\boldsymbol{\Omega}^*, t^*)$ following equation (2.3), where an HSHM is triggered by static contributors only (section 2.1). NRZs within floodplain environments at Rifle, Colorado are considered biogeochemical hot spots because they represent elevated concentrations of uranium, organic matter, and geochemically reduced minerals and they have been found to contribute to significant carbon fluxes to the atmosphere and to local rivers (Arora et al., 2016). Due to its characteristics, we considered the spatial distribution of an NRZ to be a static-mechanism-based hot spot for many constituents and processes, such as reducing minerals and denitrification. Wainwright et al. (2015) used geophysical data (e.g., induced polarization) to map the distribution of an NRZ at the subsurface level. In their study, the phase shift (ϕ) of electrical resistivity from the induced polarization data is a good indicator for mineralogical-geochemical properties. They found that (ϕ) was within $[4.5, 5]mrad$ for NRZ locations, compared to non-NRZ locations at $\phi \subseteq [1, 3.5]mrad$. Thus, ϕ can be used to construct the static indicator with a critical condition of $[4.5, 5]mrad$. Therefore,

$$I_s(\boldsymbol{\Omega}^*) = \begin{cases} 1, & if\ Z_\phi(\boldsymbol{\Omega}^*) \subseteq [4.5, 5]\ mrad \\ 0, & otherwise \end{cases}. \quad (2.10)$$

Other static attributes, including but not limited to elevation, hydraulic conductivity, and resistivity, can also be used to define the critical conditions to construct the static indicator for hot spots through Bayesian conditioning.

2.3.2 HSHMs occurring when dynamic contributors coincide at locations defined by static contributors

The second case we present here utilizes equations (2.4)–(2.6), where HSHMs are triggered when dynamic contributors coincide at hot spots determined by static contributors. Here, we present the case investigated by Duncan et al. (2013), where riparian hollows representing less than 1% of the total catchment area contributed to more than 99% of the total denitrification within the watershed. In their study, the denitrification rates peaked during the base flow (midsummer) period, when the riparian hollows were partially oxygenated and the hydrologic fluxes were at a minimum. The site was considered to have low inorganic N availability, and thus, nitrate was supplied via nitrification. The highest rates of denitrification were therefore tied to nitrification and the partially aerated conditions.

The static indicator needs to be constructed based on the microtopographical features within the riparian zone. Specifically, the topographic wetness index (TWI) (Beven & Kirkby, 1979; Sørensen et al., 2006) was used in Duncan et al. (2013) to delineate the riparian hollows from other riparian locations. Terrain analysis indicated a TWI threshold value of 6.0 and 8.0 for riparian hollows under wet and dry conditions, respectively, whereas 4.8 and smaller TWI values corresponded to other riparian locations (e.g., hummocks). Thus, the static indicator can be constructed using the TWI values within the riparian zone to determine the hot spot locations—the hollows. Hence,

$$I_s(\boldsymbol{\Omega}^*) = \begin{cases} 1, & if\ Z_{TWI}(\boldsymbol{\Omega}^*) > 6\ (wet\ condition) \text{ or } 8\ (dry\ condition) \\ 0, & otherwise \end{cases}. \quad (2.11)$$

Multiple dynamic processes control the denitrification rate at the riparian hollows. As examined by Duncan et al. (2013), a partially aerated condition ($C_{O_2} > 5\%$) is needed to support nitrification, which supplies the nitrate for denitrification. As quiescent, non-storm periods during base flow favor the coupled nitrification-denitrification mechanism, this is another key process that needs to be represented by a dynamic indicator. Although Duncan et al. (2013) did

not mention specific concentration ranges for nitrogen species, the major components, such as organic N, should be available. Therefore, we can construct the dynamic indicators as follows:

$$P[I_d(\boldsymbol{\Omega}^*, t^*) = 1] = P\left[I_{d,O_2}(\boldsymbol{\Omega}^*, t^*) = 1, I_{d,Hydro}(\boldsymbol{\Omega}^*, t^*) = 1, I_{d,N}(\boldsymbol{\Omega}^*, t^*) = 1\right], \quad (2.12)$$

where $I_{d,Hydro}(\boldsymbol{\Omega}^*, t^*)$ is the dynamic indicator representing the streamflow stages; this will be 1 if the base flow conditions are met. Additionally, here, $I_{d,N}(\boldsymbol{\Omega}^*, t^*)$ is the dynamic indicator for the transport of the nitrogen species in the subsurface that support the coupled nitrification-denitrification mechanism.

$$\begin{aligned} I_{d,O_2}(\boldsymbol{\Omega}^*, t^*) &= \begin{cases} 1, & if\ C_{O_2}(\boldsymbol{\Omega}^*, t^*) > 5\% \\ 0, & otherwise \end{cases}, \\ I_{d,Hydro}(\boldsymbol{\Omega}^*, t^*) &= \begin{cases} 1, & if\ t^* \subseteq base\ flow\ periods \\ 0, & otherwise \end{cases}, \\ I_{d,N}(\boldsymbol{\Omega}^*, t^*) &= \begin{cases} 1, & if\ C_N(\boldsymbol{\Omega}^*, t^*) > 0 \\ 0, & otherwise \end{cases}. \end{aligned} \quad (2.13)$$

It is noted that these dynamic processes are not statistically independent. Usually, when one condition is met (e.g., base flow conditions), other conditions may consistently be satisfied (e.g., the transport of nitrogen in riparian hollows). Alternatively, numerical modeling approaches are more feasible to construct the dynamic indicators based on the critical conditions at riparian hollows ($\boldsymbol{\Omega}^*$), where we could directly target N_2 fluxes using a Monte Carlo approach. The statistical formulation used here is constructed specifically for the mechanisms described by Duncan et al. (2013). Thus, the detailed threshold limits could change under other denitrification HSHMs cases, such as the case presented in Hill et al. (2000), who focus on desert landscapes, or the one by Harms and Grimm (2008), where the monsoon season is influential for the nitrogen transport. Nonetheless, the general formulation of HSHMs using indicators is still applicable.

2.3.3 HSHMs occuring when multiple dynamic processes converge in space

HSHMs can also be triggered by the confluence of multiple dynamic processes that lead to the convergence of complementary reactants at $\boldsymbol{\Omega}^*$. Accumulation of complementary reactants is mobilized and transported via different hydrologic flowpaths. They converge at hot spot locations and trigger hot moments during the mixing. Following the statistical framework developed in this chapter, equations (2.7) to (2.9) are suitable for this condition. In order to illustrate how the dynamic indicators are constructed, we consider here the case reported by Gu et al. (2012), where high biogeochemical activity was observed at the interface of groundwater and surface water during the stream stage fluctuations, which resulted in significant in-stream denitrification and NO_3^- removal.

In their study, hot spots form around the near-stream-riparian subsurface during river stage fluctuations, where active biogeochemical reaction (e.g., denitrification) requires both O_2 depletion and the simultaneous presence of NO_3^- and the dissolved organic carbon (DOC). Specifically, the spatiotemporal distribution of denitrification hot spots coincides with an O_2 depletion zone along the DOC infiltration flowpaths. In order to determine the mixing of groundwater and surface water during stage fluctuations, Gu et al. (2012) defined bank storage volume $V(t)$ and maximum bank storage volume V_{max}. The flood hydrograph was subdivided into the rising limbs, recession limbs and return flow, the latter representing the slow restitution of part of the water that infiltrated during the previous stages. Considering the different dynamics of these components, they observed that the largest infiltration rate occurred prior to the maximum stage rise, while $V_{max} = 5m^3m^{-1}$ (critical condition) occurred in the recession limb of the flood event. Instead, maximum return flow occurred toward the end of the recession curve before stream hydrograph stabilizes. Maximum NO_3^- rate removal occurred when return flow

phase was almost complete and then decreased until the depletion of NO_3^-. Through statistical analysis, they found that V_{max}, viewed as an integrated index for hydrological exchange, could explain 64% of the variation in the NO_3^- removal. Thus, V_{max} can be used as the critical state to determine whether or not the hyporheic dynamics are sufficient to enhance relevant biogeochemical processes. In order for the hot moments to be a trigger, the stream-riparian zone should also be microbially active. Based on these conditions, the dynamic indicators can be constructed as follows:

$$P[I_d(\boldsymbol{\Omega}^*, t^*) = 1] = P\big[\, I_{d,Hydro}(\boldsymbol{\Omega}^*, t^*) = 1, I_{d,Chem}(\boldsymbol{\Omega}^*, t^*) = 1\big], \tag{2.14}$$

where $I_{d,Hydro}(\boldsymbol{\Omega}^*, t^*)$ represents the dynamic process induced by the hydrologic conditions (e.g., stage fluctuation), and $I_{d,Chem}(\boldsymbol{\Omega}^*, t^*)$ represents the dynamic process controlled by the transport and accumulation of chemical reactants. Based on the critical values or ranges, we formulate the indicators as follows:

$$I_{d,Hydro}(\boldsymbol{\Omega}^*, t^*) = \begin{cases} 1, & Z_{V_{max}}(\boldsymbol{\Omega}^*, t^*) \geq 5m^3m^{-1} \\ 0, & otherwise \end{cases},$$

$$I_{d,Chem}(\boldsymbol{\Omega}^*, t^*) = \begin{cases} 1, & if\ C_{O_2}(\boldsymbol{\Omega}^*, t^*)\ is\ small\ and\ C_{NO_3^-}(\boldsymbol{\Omega}^*, t^*) > 0\ and\ C_{DOC}(\boldsymbol{\Omega}^*, t^*) > 0 \\ 0, & otherwise \end{cases}. \tag{2.15}$$

Typically, because of the complexity of the processes, no analytical solutions are available for formulating the indicators. However, Monte Carlo simulations can be useful in constructing such indicators. For this case, an HSHM at any given location and time $(\boldsymbol{\Omega}^*, t^*)$ will only be triggered when all of the conditions are met and the ensemble mean of the indicator assumes the following form:

$$< I_d(\boldsymbol{\Omega}^*, t^*) > = \frac{1}{N}\sum_{i=1}^{N} I_{d,i}(\boldsymbol{\Omega}^*, t^*)\ , \tag{2.16}$$

where $I_{d,i}(\boldsymbol{\Omega}^*, t^*)$ is the value that the indicator assumes in the i^{th} realization and N is the total number of simulations.

Overall, our choices of the three studies should not limit the generalizability of the indicator statistics approach for deriving statistical formulations for HSHM applications. The critical conditions chosen to construct the indicators are determined solely on the findings from these selected studies, and they will vary under different scenarios.

2.4 HSHM applications in groundwater hydrology

Processes occurring within the subsurface are important factors leading to HSHM occurrences. Among others, these processes include the migration of groundwater carrying reducing substrates, nuclear waste transport within the subsurface, the accumulation and transport of dense non-aqueous phase liquid (DNAPL) and other biogeochemical processes. Some current modeling approaches that focus on subsurface HSHMs assume simplified hydrologic structures (e.g., homogeneous and isotropic domains) in quantifying contaminant fate and transport in the subsurface. However, such an assumption neglects the effect of the heterogeneity in the subsurface, leading to the underestimation of the uncertainties in the HSHM occurrences. Thus, in this section, we focus on HSHM applications in groundwater hydrology, with a particular emphasis on spatial variability in the subsurface. Specifically, we consider several situations often encountered in groundwater contamination studies and present the indicator statistical formulations of HSHMs. With these results, we can determine the probability of HSHMs occurrences in the subsurface at a given time and space. Further, we are able to

determine how spatial variability influences HSHM occurrences and how this is translated into environmental health risks.

2.4.1 Importance of spatial variability in the subsurface

The heterogeneous structure of hydraulic conductivity leads to significant variability in the contaminant transport in the subsurface, which further results in the heterogeneity of biogeochemical cycling, such as the development of NRZs, reactive facies, and heterogeneity in aquifers' reactivity (Li et al., 2010; Loschko et al., 2016; Sassen et al., 2012; Wainwright et al., 2015).

Figure 2.2 demonstrates the uncertainty associated with HSHMs by looking at the flow fields in two-dimensional log-hydraulic conductivity ($Y = ln(K)$) fields with streamlines resulting from a uniform mean head gradient, left to right. The three panels differ in terms of the variance, σ_Y^2, of the log-conductivity. The covariance function used for generating the fields is exponential and isotropic. σ_Y^2 is shown to have a profound impact upon the conductivity field. As the variance increases, regions of high and low log-conductivity emerge, creating preferential flow paths bypassing the low conductivity zones as shown by particle trajectories. At smaller variance (i.e., $\sigma_Y^2 = 0.1$), particles mainly travel along the mean flow direction with very limited departure from the mean trajectory, which are the straight lines connecting the left and right boundaries. In this situation, the arrival times of solute particles to critical locations (i.e., $\boldsymbol{\Omega}^*$))are predictable. With large variances (i.e., $\sigma_Y^2 = 2$), the streamlines assume a very irregular, hard-to-predict geometry, and we can observe the emergence of flow channels, where particles can move fast, next to stagnant flow regions. Arrival times become more uncertain, because the exact geometry of the streamlines is hard to predict unless the Y field is known deterministically. However, in another realization of the Y field, the situation may be totally different, resulting in significant uncertainties in predicting the particle travel times. Thus, spatial variability of log-conductivity is a major uncertainty-inducing factor, by extension, obviating the need for stochastic modeling of HSHMs in situations where the associated processes and attributes are subject to uncertainty. In the following sections, we will present illustrative examples to analyze how subsurface spatial variability influences $< I_{HSHM}(\boldsymbol{\Omega}^*, t^*) >$, including variance and anisotropy ratio of the log-conductivity.

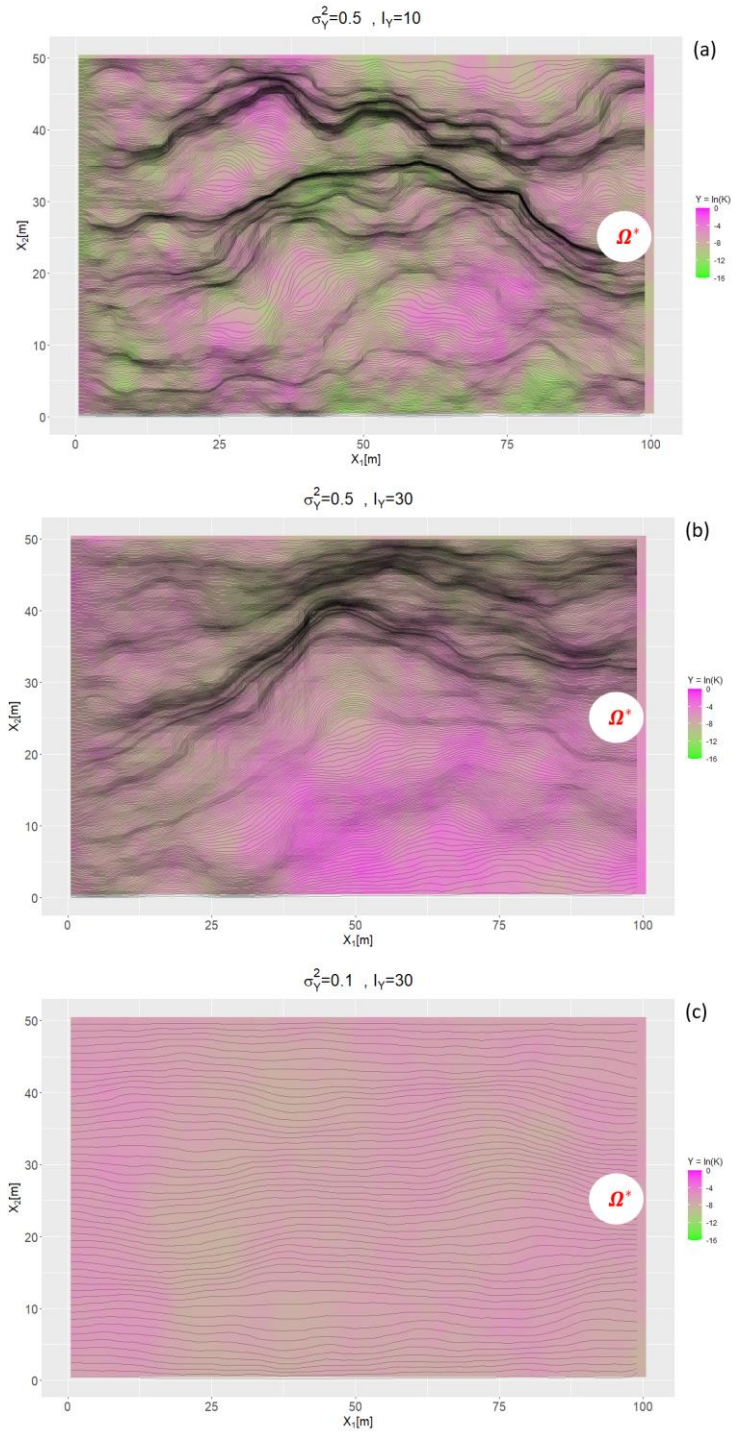

Figure 2.2 Illustrative example of a heterogeneous log-hydraulic conductivity field and solute particle transport. Black lines represent simulated particle travel paths.

2.4.2 Geostatistics and Lagrangian Approaches to Flow and Solute Transport

Assuming steady, uniform in the average flow with mild heterogeneity of the log-hydraulic conductivity field with Gaussian displacement, the displacement pdf in the longitudinal direction (x_1) is given by the following equation (Dagan and Nguyen, 1989; Dagan and Rubin, 1992):

$$f_{X_1(t^*)}(x_1) = \frac{1}{\sqrt{2\pi X_{11}(t^*)}} \exp\left[-\frac{1}{2}\frac{(x_1 - Ut^*)^2}{X_{11}(t^*)}\right]. \quad (2.17)$$

Additionally, the displacement pdf in the transverse directions (x_2 and x_3) is given by

$$f_{X_i(t^*)}(x_i) = \frac{1}{\sqrt{2\pi X_{ii}(t^*)}} \exp\left[-\frac{1}{2}\frac{x_i^2}{X_{ii}(t^*)}\right], i = 2,3. \quad (2.18)$$

Dagan (1984) developed a solution for the displacement variances for an exponential and axisymmetric covariance function:

$$C_Y(\boldsymbol{r}) = \langle (Y(\boldsymbol{x}) - \langle Y\rangle)\,(Y(\boldsymbol{x}+\boldsymbol{r}) - \langle Y\rangle)\rangle = exp\left[-\sqrt{\frac{r_1^2+r_2^2}{I_{Yh}^2} + \frac{r_3^2}{I_{Yv}^2}}\right], \quad (2.19)$$

$$\begin{aligned} X_{11} = \sigma_Y^2 I_Y^2 \Bigg\{ & 2t^* + 2[\exp(-t^*) - 1] \\ & + 8e \int_0^\infty [\bar{J}_0(Kt^*) - 1] \\ & \times \left[\frac{1}{(1+K^2-e^2K^2)^2} - \frac{eK}{(1+K^2-e^2K^2)^2(1+K^2)^{0.5}} \right. \\ & \left. - \frac{eK}{2(1+K^2-e^2K^2)(1+K^2)^{1.5}}\right] dK - 2e \int_0^\infty [\bar{J}_0(Kt^*) - \frac{\bar{J}_1(Kt^*)}{Kt^*} - \frac{1}{2}\Bigg] \\ & \times \left[\frac{e^3K^3(e^2K^2-5-5K^2)}{(e^2K^2-1-K^2)^{1.5}} + \frac{1+K^2-5e^2K^2}{(1+K^2-e^2K^2)^3}\right] dK, \end{aligned} \quad (2.20)$$

$$\begin{aligned} X_{22} = & -2e\sigma_Y^2 I_Y^2 \\ & \int_0^\infty \left[\frac{\bar{J}_1(Kt^*)}{t^*} - \frac{K}{2}\right]\left[\frac{e^3K^2(e^2K^2-5K^2-5)}{(e^2K^2-1-K^2)^3(1+K^2)^{1.5}} + \frac{1+K^2-5e^2K^2}{K(1+K^2-e^2K^2)}\right] dK, \end{aligned} \quad (2.21)$$

$$\begin{aligned} X_{33} = & -4e\sigma_Y^2 I_Y^2 \int_0^\infty [\bar{J}_0(Kt^*) - 1] \\ & \times \left\{\frac{1}{(e^2K^2-1-K^2)^2}\left[\frac{1}{2} + \frac{2e^2K^2}{1+K^2-e^2K^2} + \frac{eK(e^2K^2+3+3K^2)}{2(e^2K^2-1-K^2)(1+K^2)^{0.5}}\right]\right\} dK. \end{aligned} \quad (2.22)$$

where $\boldsymbol{r}$ is the two-point separation distance and $\langle Y\rangle$ the ensemble mean of the log-conductivity $Y = \ln K$. $\bar{J}_0$ and $\bar{J}_1$ are, respectively, the zero and first order of the first kind Bessel functions.

Dagan (1984) provided analytical solutions for longitude and transverse displacement variances. This is a special case for the anisotropic case with $e = 1$.The solutions are as follows:

$$X_{11} = \sigma_Y^2 I_Y^2 \left\{2t^* - 2 * \left[\frac{8}{3} - \frac{4}{t^*} + \frac{8}{t^{*3}} - \frac{8}{t^{*2}}\left(1 + \frac{1}{t^*}\right)\exp(-t^*)\right]\right\}. \quad (2.23)$$

$$X_{22} = X_{33} = 2\sigma_Y^2 I_Y^2 \left[\frac{1}{3} - \frac{1}{t^*} + \frac{4}{t^{*3}} - \left(\frac{4}{t^{*3}} + \frac{4}{t^{*2}} + \frac{1}{t^*}\right)\exp(-t^*)\right]. \quad (2.24)$$

2.5 Case studies and expansions of indicators

2.5.1 Single-particle I_d within Ω^*

Consider the case of a point source release of non-reactive tracer originating from $(\boldsymbol{x_0}, t_0)$. The dynamic indicator depends on parcel being within $\boldsymbol{\Omega}^*$ at time t^* or not. If local (pore scale) dispersion is neglected, the dynamic indicator is defined as follows:

$$I_d(\boldsymbol{\Omega}^*, t^*) = \begin{cases} 1, & if\ \boldsymbol{X}(\boldsymbol{t}^*) \subseteq \boldsymbol{\Omega}^*\ at\ t^* \\ 0, & otherwise \end{cases}, \tag{2.25}$$

given that the particle does not change its volume while traveling. The expected value of this dynamic indicator at t^* is therefore:

$$< I_d(\boldsymbol{\Omega}^*, t^*) >= \int_{\Omega^*} f_{\boldsymbol{X}(\boldsymbol{t}^*)}(\boldsymbol{a}|\boldsymbol{x}_0, t_0) d\boldsymbol{a}, \tag{2.26}$$

where $f_{\boldsymbol{X}(\boldsymbol{t}^*)}(\boldsymbol{a}|\boldsymbol{x}_0, t_0)$ is the probability distribution function (pdf) of the particle's trajectory at t^* (Dagan & Nguyen, 1989; Rubin, 2003). Other situations may be addressed by using the same framework. For example, for an instantaneous injection within a source volume V_0, the ensemble mean of the dynamic indicator assumes the following form:

$$< I_d(\boldsymbol{\Omega}^*, t^*) >= \frac{1}{V_0} \int_{V_0} \int_{\Omega^*} f_{\boldsymbol{X}(\boldsymbol{t}^*)}(\boldsymbol{a}|\boldsymbol{x}_0, t_0) d\boldsymbol{a} d\boldsymbol{x}_0. \tag{2.27}$$

2.5.2 Concentration-based I_d within $\boldsymbol{\Omega}^*$

When considering local dispersion, or in case of a reactive tracer, the condition that the particle is inside the volume $\boldsymbol{\Omega}^*$ does not suffice to define the dynamic indicator and a concentration threshold C_{th} should be introduced:

$$I_d(\boldsymbol{\Omega}^*, t^*) = \begin{cases} 1, & if\ \boldsymbol{X}(t^*; \boldsymbol{x}_0, t_0) \subseteq \boldsymbol{\Omega}^*\ and\ C(\boldsymbol{X}, t^*) > C_{th} \\ 0, & otherwise \end{cases}. \tag{2.28}$$

In the absence of local dispersion and for a reactive solute decaying at a (spatially) constant rate k, the ensemble mean assumes the following expression (Cvetkovic & Shapiro, 1990):

$$< I_d(\boldsymbol{\Omega}^*, t^*) >= \left\{1 - H\left[t^* - \frac{1}{k}\ln(\frac{C_0}{C_{th}})\right]\right\} \int_{\Omega^*} f_{\boldsymbol{X}(\boldsymbol{t}^*)}(\boldsymbol{a}|\boldsymbol{x}_0, t_0) d\boldsymbol{a}, \tag{2.29}$$

where C_0 is the initial concentration and $H[\cdot]$ is the Heaviside step function. The ensemble mean (2.29) is the product of the probability that the particle assumes a concentration larger than the threshold at t^* (given that reaction rate k is constant, this probability is either 0 or 1) and the probability that at the same time t^* the particle is within the hot spot $\boldsymbol{\Omega}^*$. In other words, equation (2.29) expresses the fact that a particle inside $\boldsymbol{\Omega}^*$ contributes to the hot moment only if its concentration is greater than the threshold. Equation (2.29) can be generalized to the cases of instantaneous injection into a source of volume V_0, as discussed before for the non-reactive case. For other complex situations, such as that in which k is spatially variable and complex reaction networks, the ensemble mean of the indicators can be addressed by equation (2.16) in a Monte Carlo framework.

2.5.3 Assessing the duration of hot moment and probabilities

The probability that the hot moment persists over the interval $[t_1, t_2]$ at $\boldsymbol{\Omega}^*$ can be formally computed as follows:

$$< I_d(\boldsymbol{\Omega}^*, t_1, t_2) >= P(t_1, \boldsymbol{\Omega}^*) P(t_2|t_1, \boldsymbol{\Omega}^*), \tag{2.30}$$

where $P(t_1, \boldsymbol{\Omega}^*)$ is the probability that the particle is inside $\boldsymbol{\Omega}^*$ at time $t^* = t_1$ and $P(t_2|t_1, \boldsymbol{\Omega}^*)$ is the probability that the particle is still inside $\boldsymbol{\Omega}^*$ at time $t^* = t_2$, provided that at time t_1, it was also inside $\boldsymbol{\Omega}^*$. If the particle exits $\boldsymbol{\Omega}^*$ during interval $[t_1, t_2]$, this time interval will not be qualified as hot moment; and thus the probability computation needs to ensure the particle stays within $\boldsymbol{\Omega}^*$ during the entire time interval.

Under the First-Order Approximation (FOA) (see e.g., Dagan, 1989; Gelhar 1993; Rubin, 2003), the pdf of the particle displacement is normal with mean $< \boldsymbol{X}(t^*; \boldsymbol{x_0}, t_0) >$ and auto-covariance tensor of the residual displacements $\boldsymbol{X}'(t^*) = \boldsymbol{X}(t^*) - \langle \boldsymbol{X}(t^*) \rangle$ defined by

$\boldsymbol{X}_{ij}(t^*; \boldsymbol{x}_0, t_0) = \langle \boldsymbol{X}_i'(t^*; \boldsymbol{x}_0, t_0) \boldsymbol{X}_j'(t^*; \boldsymbol{x}_0, t_0) \rangle,\ i,j = 1,2,3.$ For simplicity in the following, we assume $\boldsymbol{x}_0 = 0\ and\ t_0 = 0$. Under these assumptions,

$$< I_d(\boldsymbol{\Omega}^*, t_1, t_2) >= \int_{\boldsymbol{\Omega}^*} \int_{\boldsymbol{\Omega}^*} f_{\boldsymbol{X}(t_1)}(\boldsymbol{a}) f^c_{\boldsymbol{X}(t_2)}(\, \boldsymbol{b} | \boldsymbol{X}(t_1) = \boldsymbol{a})\, d\boldsymbol{b}\, d\boldsymbol{a}, \tag{2.31}$$

where the conditional pdf $f^c_{\boldsymbol{X}(t_2)}(\boldsymbol{b}|\boldsymbol{X}(t_1) = \boldsymbol{a})$ is multi-normally distributed with conditional mean and variance tensor given by

$$\langle \boldsymbol{X}(t_2) |\, \boldsymbol{X}(t_1) = \boldsymbol{a}) \rangle = < \boldsymbol{X}(t_2) > + Cov[\boldsymbol{X}'(t_2), \boldsymbol{X}'(t_1)] \cdot Var[\boldsymbol{X}'(t_1)]^{-1} \cdot (\boldsymbol{a} - < \boldsymbol{X}(t_1) >), \tag{2.32}$$

and

$$\boldsymbol{\sigma}(t_1, t_2) = Var[\boldsymbol{X}'(t_2)] - Cov[\boldsymbol{X}'(t_2), \boldsymbol{X}'(t_1)] \cdot Var[\boldsymbol{X}'(t_1)]^{-1} \cdot Cov[\boldsymbol{X}'(t_1), \boldsymbol{X}'(t_2)], \tag{2.33}$$

respectively, which further yields the following,

$$f^c_{\boldsymbol{X}(t_2)}(\, \boldsymbol{b} | \boldsymbol{X}(t_1) = \boldsymbol{a}) = exp\left[-\frac{1}{2} \left[\boldsymbol{b} - \langle \boldsymbol{X}(t_2) |\, \boldsymbol{X}(t_1) = \boldsymbol{a}) \rangle \right]^T \cdot \boldsymbol{\sigma}(t_1, t_2)^{-1} \cdot \left[\boldsymbol{b} - \langle \boldsymbol{X}(t_2) |\, \boldsymbol{X}(t_1) = \boldsymbol{a}) \rangle \right] \right] * \{ 8\, \pi^3 \cdot |\boldsymbol{\sigma}(t_1, t_2)| \}^{-\frac{1}{2}}, \tag{2.34}$$

where $|\cdot|$ indicates the determinant, exp is the exponential function and the exponent T indicates the transpose of the vector.

In equations (2.31) and (2.32), $\boldsymbol{X}'(t^*) = \boldsymbol{X}(t^*) - \langle \boldsymbol{X}(t^*) \rangle$ stands for the departure of the particle's displacement with respect to the ensemble mean trajectory, and $Var[\boldsymbol{X}]^{-1}$ is the auto-covariance tensor of the residual displacement whose elements are defined above. Similarly, $Cov[\boldsymbol{X}'(t_1), \boldsymbol{X}'(t_2)]$ is the covariance tensor of residual displacement which elements are: $\boldsymbol{X}_{ij}(t_1, t_2; \boldsymbol{x_0}, t_0) = \langle X_i'(t_1)\, X_j'(t_2) \rangle, i,j = 1,2,3$. Note that in the general three-dimensional case $\langle \boldsymbol{X}(t_2) |\, \boldsymbol{X}(t_1) = \boldsymbol{a}) \rangle$ is a three-dimensional vector and $\boldsymbol{\sigma}(t_1, t_2)$ is a 3×3 second-order tensor. For $t_2 \to t_1$, $f_{X(t_2)}[\boldsymbol{b}|\boldsymbol{X}(t_1) = \boldsymbol{a}] \to \delta(\boldsymbol{b})$, where $\delta(\cdot)$ is the Dirac Delta, such that $P(t_2|t_1, \boldsymbol{\Omega}^*) \to 1$. On the other hand, for $t_2 \gg t_1$, $Cov[\boldsymbol{X}'(t_1), \boldsymbol{X}'(t_2)] \to 0$ and $P(t_2|t_1, \boldsymbol{\Omega}^*) \to P(t_2, \boldsymbol{\Omega}^*)$ the marginal probability that the particle is within $\boldsymbol{\Omega}^*$ at time $t^* = t_2$. Equations (2.31) to (2.34) are obtained under the FOA approximation and assuming that the particle can enter $\boldsymbol{\Omega}^*$ only once. Such assumption is needed to obtain analytical solutions and is reasonable for situations with small to mild subsurface heterogeneity (e.g., $\sigma_Y^2 \leq 1.6$), such as the cases presented in Bellin et al. (1992, 1994); Cvetkovic et al. (1992). In particular, FOA assumes small heterogeneity and under this assumption the particle trajectory deviates slightly from its ensemble mean, which is directed along the regional hydraulic head gradient. For a regular volume $\boldsymbol{\Omega}^*$, this reduces the probability of the particle entering the hot spot more than once. This probability reduces further if in horizontal and vertical transverse directions $\boldsymbol{\Omega}^*$ is much larger than the respective integral scales, because the probability of observing negative longitudinal velocity components (i.e., along the mean flow field) is much smaller than in the transverse directions (Bellin et al., 1992) and vanishes as formation heterogeneity reduces.

If the hotspot $\boldsymbol{\Omega}^*$ is the volume confined between two planes at $x_1 - \frac{l_1}{2}$ and $x_1 + \frac{l_1}{2}$, with the other two dimensions much larger than the transverse horizontal and vertical integral scales: $l_2 \gg I_h$, $l_3 \gg I_v$, equation (2.34) simplifies to:

$$< I_d(\boldsymbol{\Omega}^*, t_1, t_2) >= \int_{x_1 - \frac{l_1}{2}}^{x_1 + \frac{l_1}{2}} \int_{x_1 - \frac{l_1}{2}}^{x_1 + \frac{l_1}{2}} f_{X_1(t^*)}(a_1) f^c_{X_1(t^*)}(\, b_1 | X_1(t_1) = a_1)\, db_1\, da_1, \tag{2.35}$$

where X_1 is the longitudinal component of the particle's trajectory and $f^c_{X_1(t^*)}$ is its conditional pdf, which is normal with conditional mean and variance given by

$$\mu[a_1] = \langle X_1(t_2) | X_1(t_1) = a_1) \rangle = < X_1(t_2) > + \frac{X_{11}(t_1, t_2)}{X_{11}(t_1)} (X_1(t_1) - < X_1(t_1) >), \quad (2.36)$$

and

$$\sigma^2(t_1, t_2) = X_{11}(t_2) - \frac{X_{11}(t_1, t_2)^2}{X_{11}(t_1)}, \quad (2.37)$$

respectively. Consequently, $f_{X^c(t^*)}$ in equation (2.35) assumes the following form:

$$f^c_{X_1(t^*)}(b_1 | X_1(t_1) = a_1) = \frac{1}{\sqrt{2\,\pi\,\sigma(t_1, t_2)}} Exp\left[-\frac{1}{2}(b_1 - \mu[a_1])^2\, \sigma(t_1, t_2)^{-1}\right]. \quad (2.38)$$

Substituting equation (2.37) into equation (2.35) allows us to compute $< I_d(\boldsymbol{\Omega}^*, t_1, t_2) >$. For situations where the FOA assumptions are not valid (e.g., large heterogeneity), Monte Carlo simulation framework is still applicable as alternative approach to construct the dynamics indicators (see equation 16).

2.6 Illustrative example and indicator formulation

Following sections 2.5.1 and 2.5.2, we present here synthetic case studies that demonstrate the statistical formulation of the indicators using methods developed in stochastic hydrogeology. The choice of the synthetic case studies does not limit our approaches to broader applications where stochastic modeling with Monte Carlo simulations are applicable. In most applications, the locations of hot spots ($\boldsymbol{\Omega}^*$) are determined by static indicators, such as riparian hollows (Duncan et al., 2013) and reactive facies (Sassen et al., 2012), and NRZs (Wainwright et al., 2015). The static indicator is constructed according to the corresponding critical conditions provided by ancillary data such as topography, remote sensing, and/or geophysical data. Hence, in this case, assuming the boundaries of $\boldsymbol{\Omega}^*$ are determined by a static indicator, we consider a hot spot ($\boldsymbol{\Omega}^*$) to be confined within the following volume: $w_1 \leq x_1 \leq w_1'; w_2 \leq x_2 \leq w_2'; w_3 \leq x_3 \leq w_3'$.

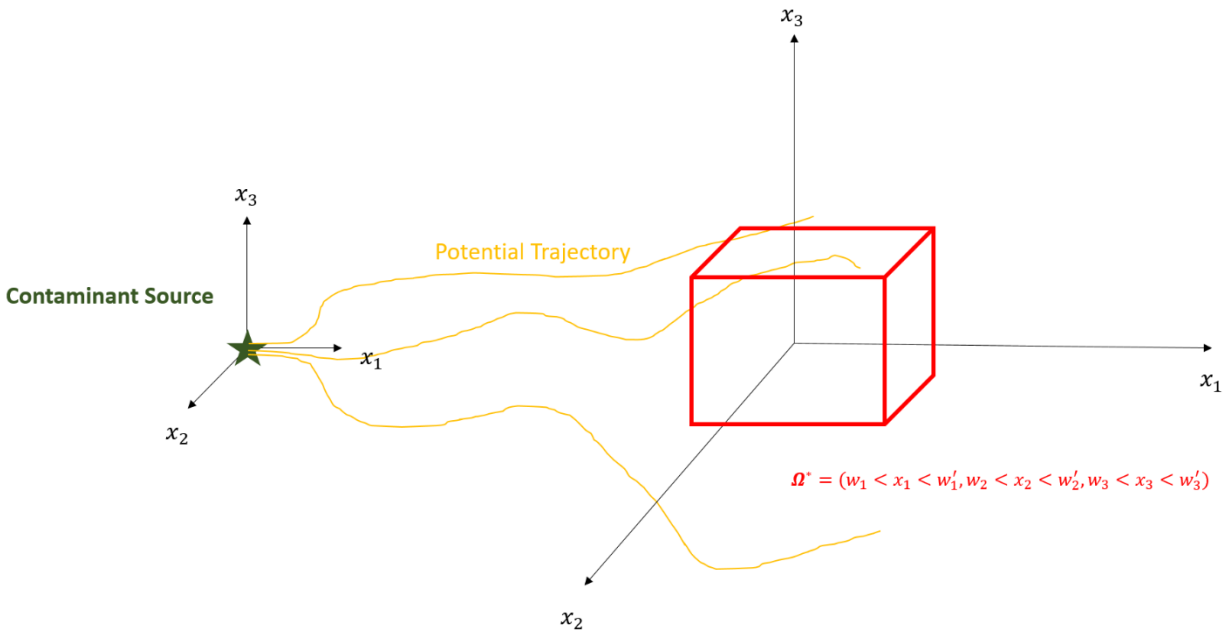

Figure 2.3 Configuration of the synthetic case study. Parcels originate from source denoted by star. Yellow lines represent potential trajectories. Red cube is assumed to be hot spot location, $\boldsymbol{\Omega}^*$.

Given this case, the hot moment will be triggered only when the contaminant particle is found within $\boldsymbol{\Omega}^*$. The probability of finding the contaminant particle within $\boldsymbol{\Omega}^*$ is given by

$$prob\,\{\boldsymbol{X}(t^*) \subseteq \boldsymbol{\Omega}^*\}$$
$$= \prod_{i=1}^{m} prob\{w_i \le X_i(t^*) \le w_i'\} = \prod_{i=1}^{m} \int_{w_i}^{w_i'} f_{X_i(t^*)}(a_i|x_0,t_0)da_i, \qquad (2.39)$$

where *m* denotes the space dimensionality. Equation (2.39) defines the dynamic indicator for this case. If $\boldsymbol{\Omega}^*$ is already identified as a hot spot location, then equation (2.39) provides $< I_{HSHM}(\boldsymbol{\Omega}^*, t^*) >$. Otherwise, the static indicator should be incorporated to determine the boundaries of $\boldsymbol{\Omega}^*$ in order to compute $< I_{HSHM}(\boldsymbol{\Omega}^*, t^*) >$ as shown in equation (2.10) where geophysical data is used to identify the spatial context of $\boldsymbol{\Omega}^*$. If we also assume steady, uniform in the average flow with mild heterogeneity of the log hydraulic conductivity field with Gaussian displacement pdf—then we can compute $< I_{HSHM}(\boldsymbol{\Omega}^*, t^*) >$ analytically using the following equation:

$$< I_{HSHM}(\boldsymbol{\Omega}^*, t^*) > = < I_s(\boldsymbol{\Omega}^*) > < (I_d(\boldsymbol{\Omega}^*, t^*) >$$
$$= prob(I_d(\boldsymbol{\Omega}^*, t^*) = 1) = prob\,\{X(t^*) \subseteq \boldsymbol{\Omega}^*\}$$
$$= \prod_{i=1}^{m} \int_{w_i}^{w_i'} f_{X_i(t^*)}(a_i|x_0,t_0)da_i$$
$$= \int_{w_1}^{w_1'} f_{X_1(t^*)}(a_1|x_0,t_0)da_1 \int_{w_2}^{w_2'} f_{X_2(t^*)}(a_2|x_0,t_0)da_2 \int_{w_3}^{w_3'} f_{X_3(t^*)}(a_3|x_0,t_0)da_3$$
$$= \frac{1}{(2\pi)^{\frac{3}{2}}\sqrt{X_{11}(t^*)X_{22}(t^*)X_{33}(t^*)}} \int_{w_1}^{w_1'} \exp\left[-\frac{1}{2}\frac{(a_1 - Ut^*)^2}{X_{11}(t^*)}\right]da_1$$
$$* \int_{w_2}^{w_2'} \exp\left[-\frac{1}{2}\frac{a_2^2}{X_{22}(t^*)}\right]da_2 \int_{w_3}^{w_3'} \exp\left[-\frac{1}{2}\frac{a_3^2}{X_{33}(t^*)}\right]da_3. \qquad (2.40)$$

which can be integrated to yield :

$$< I_{HSHM}(\boldsymbol{\Omega}^*, t^*) > = \frac{1}{8}\left[erfc\left(\frac{w_1 - Ut^*}{\sqrt{2X_{11}(t^*)}}\right) - erfc\left(\frac{w_1' - Ut^*}{\sqrt{2X_{11}(t^*)}}\right)\right]$$
$$* \left[erfc\left(\frac{w_2}{\sqrt{2X_{22}(t^*)}}\right) - erfc\left(\frac{w_2'}{\sqrt{2X_{22}(t^*)}}\right)\right] *$$
$$\left[erfc\left(\frac{w_3}{\sqrt{2X_{33}(t^*)}}\right) - erfc\left(\frac{w_3'}{\sqrt{2X_{33}(t^*)}}\right)\right]. \qquad (2.41)$$

The form of the displacement variances is controlled by the spatial distribution of the hydraulic conductivity in the subsurface. Equations (2.17)-(2.24) of the appendix show the displacement variances for an axisymmetric exponential covariance function of the log-conductivity (2.20).

2.7 Implications for HSHMs

In the following sections, we present the results from the case study described in section 2.6. Specifically, in section 2.7.1 and 2.7.2, we explore how heterogeneity of log-hydraulic conductivity influences the probability of HSHM occurrences. To make results as general as possible, lengths are made dimensionless with respect to the integral scales (I_{Yh} in the two horizontal directions and I_{Yv} in the vertical one) and time with respect to the following advective time scale: I_{Yh}/U, where U is the mean velocity). In the following, we explore the effect of the remaining parameters, i.e. the anisotropy ratio $e = \frac{I_{YV}}{I_{YH}}$ and the variance of the log-conductivity σ_Y^2, on the emergence of HSHM. We placed $\boldsymbol{\Omega}^*$ along the mean trajectory at $(21I_{YH}, 0, 0)$ with dimensions as $(2I_{YH}, 2I_{YH}, 2I_{YV})$. The dimensions of the hot spot are therefore of two integral scales in the three coordinate directions $(x_1, x_2, x_3)$and is placed at a dimensionless distance of 21 from the point source.

2.7.1 Dependence of $< I_{HSHM}(\boldsymbol{\Omega}^*, \boldsymbol{\tau}) >$ on variance in the spatial correlation structure of the log-conductivity

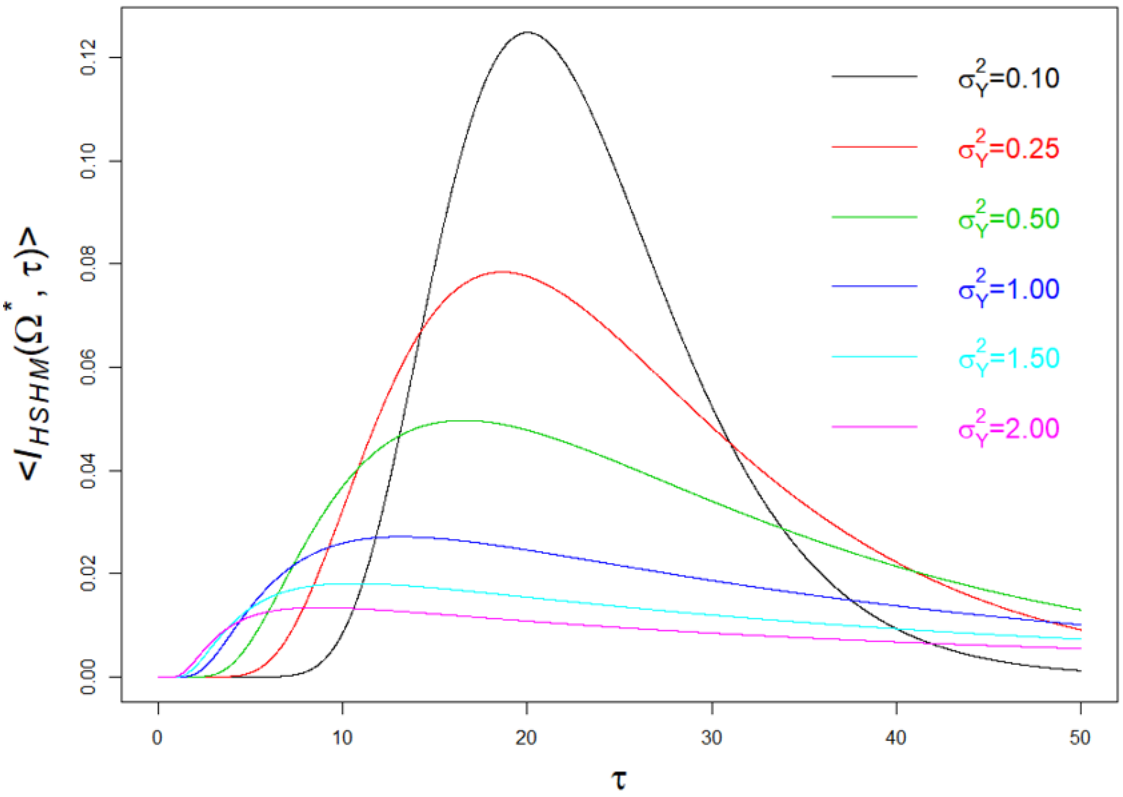

Figure 2.4 Dependence of $< I_{HSHM}(\boldsymbol{\Omega}^*, \boldsymbol{\tau}) >$ on $\boldsymbol{\sigma_Y^2}$. Smaller $\boldsymbol{\sigma_Y^2}$ lead to greater peak $< I_{HSHM}(\boldsymbol{\Omega}^*, \boldsymbol{\tau}) >$ and less spread over time, whereas greater $\boldsymbol{\sigma_Y^2}$ and greater spread of $< I_{HSHM}(\boldsymbol{\Omega}^*, \boldsymbol{\tau}) >$ over time are observed.

Isotropic heterogeneity ($e = 1$ and the particle moments given by Eqs. (2.23) and (2.24)) was considered to investigate the dependence of $< I_{HSHM}(\boldsymbol{\Omega}^*, \tau) >$ on σ_Y^2 with results presented in Figure 2.4. $\tau = tU/I_{Yh}$ is the dimensionless time. At early time (e.g., $\tau < 5$), larger probability $< I_{HSHM}(\boldsymbol{\Omega}^*, \tau) >$ is observed with increase in σ_Y^2. At intermediate time, i.e., at times comparable with the mean travel time $\tau = 21$, $< I_{HSHM}(\boldsymbol{\Omega}^*, \tau) >$ is inversely proportional to σ_Y^2. At late time (e.g., $\tau > 40$), the largest $< I_{HSHM}(\boldsymbol{\Omega}^*, \tau) >$ occurs at intermediate σ_Y^2. We observe that σ_Y^2 regulates the timing of the peak in $< I_{HSHM}(\boldsymbol{\Omega}^*, \tau) >$, which is located in the

proximity of the mean travel time, $\tau = 21$, for weak heterogeneity, and shifts towards earlier times as σ_Y^2 increases.

These effects relate to the relationship between travel times (from the source to $\boldsymbol{\Omega}^*$) and σ_Y^2. The key point to note is that σ_Y^2 controls the spread of the travel time around the mean travel time. Larger variance enhances channeling effects (Fiori & Jankovic, 2012; Moreno & Tsang, 1994, also in Figue 2), which in turn enables earlier arrival times. But at the same time, large σ_Y^2 also leads to the low-conductivity zones. Streamlines of the solute tend to bypass low hydraulic conductivity zones; however, the small amount of solute that actually penetrates these zones by advection and diffusion gets trapped for long time before being released and this results in an extended tailing with low concentration and therefore low $< I_{HSHM}(\boldsymbol{\Omega}^*, \tau) >$. Thus, with an increase in σ_Y^2, we notice an increase in the probability to observe both increasingly earlier and increasingly delayed arrival times, which widens the probability distribution. On the contrary at small variance, particles deviate little from the ensemble mean trajectory, because of the small contrast in conductivity between high and low conductivity zones. This results in small particle spreading and travel times that differ only slightly from the mean travel time ($\tau = 21$), and a probability distribution with less spread around the mean, where the peak is observed.

In summary, hydraulic conductivity contrast between low and high conductive lithofacies increases with σ_Y^2, leading to the emergence of organized high conductivity pathways sneaking through surrounding low conductivity zones with the latter acting as "trapping" elements. This causes the emergence of both early and late arrival times. Early arrival times are controlled by the connected high conductivity pathways and the late arrival times are influenced by the low conductivity zones, which act as low-release reservoirs for solutes.

2.7.2 Dependence of $< \boldsymbol{I_{HSHM}(\Omega^*, \tau)} >$ on on anisotropy in the spatial correlation structure of the log-hydraulic conductivity

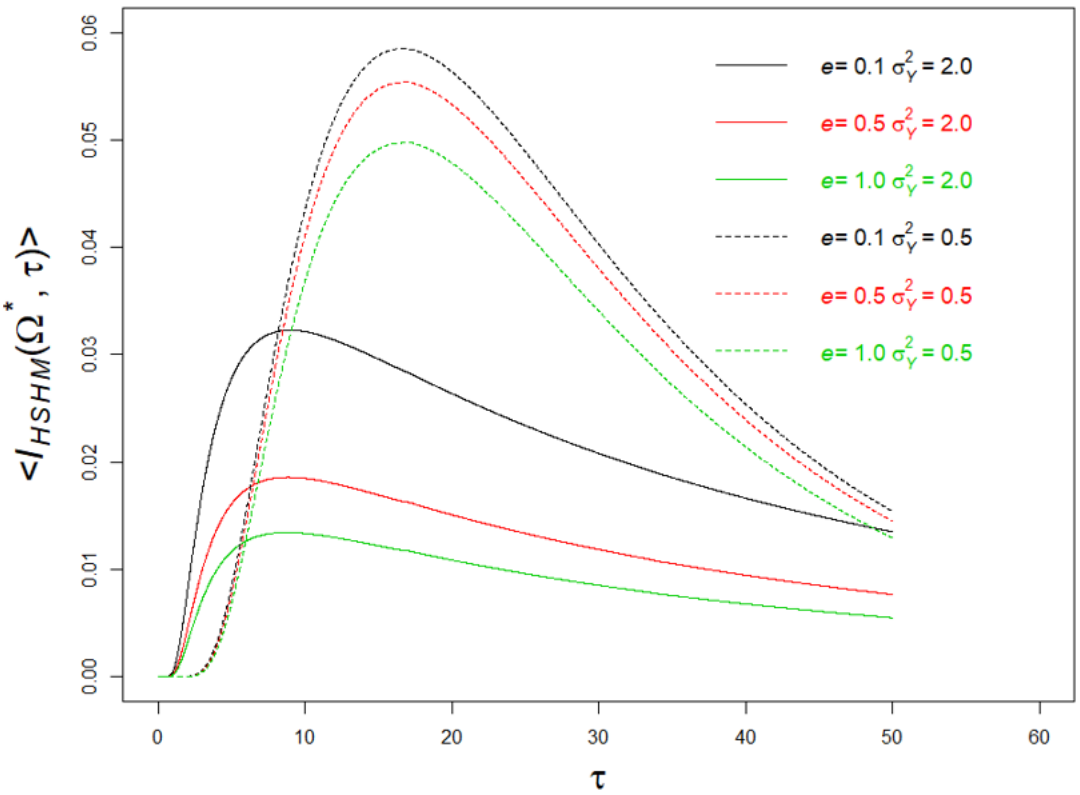

Figure 2.5 Dependence of $< I_{HSHM}(\boldsymbol{\Omega}^*, \boldsymbol{\tau}) >$ on e. This figure shows that with increasing e, peak $< I_{HSHM}(\boldsymbol{\Omega}^*, \boldsymbol{\tau}) >$ decreases. Magnitude of e does not contribute to the timing of peak $< I_{HSHM}(\boldsymbol{\Omega}^*, \boldsymbol{\tau}) >$.

The discussion here (accompanying Figure 2.5) focuses on the impact of the anisotropy ratio in the correlation structure (e, defined above) on the HSHM probabilities. The anisotropy ratio, e, provides an indication about the persistence of the log-conductivity (Y) in the various directions. The spatial correlation model used here for demonstration is that of axis-symmetry, which is common to sedimentary formations (Dagan, 1989; Rubin, 2003), with e providing the ratio between the persistence of Y in the vertical (x_3) direction, represented by I_{YV}, and the ones on the horizontal plane ($x_1 - x_2$), represented by I_{YH}. In unconsolidated sedimentary formations, I_{YV} is typically smaller than I_{YH} by as much as one order of magnitude, due to the different time scales of the depositional process taking place in the horizontal and vertical directions, which leads to thin and elongated lithofacies and consequently to a much smaller persistence of Y values in normal to the horizontal plane (Miall, 1985, 1988; Ritzi et al., 2004).

Figure 2.5 compares $< I_{HSHM}(\boldsymbol{\Omega}^*, \tau) >$ between formations defined by different anisotropy ratios and different σ_Y^2. It shows that we have two factors to consider when explaining the differences in $< I_{HSHM}(\boldsymbol{\Omega}^*, \tau) >$. First factor, as discussed earlier, is the expansion in the range of travel times due to increase in σ_Y^2. With larger variance, we observe higher probabilities for departure of the travel times away from the average. The anisotropy ratio e adds a compounding factor. To understand its effect, we should recall the analyses of lateral displacement variances of solute particles moving in heterogeneous formations (cf., Dagan, 1989, and equations 2.17 to 2.24 here), showing that smaller e leads to smaller lateral (both vertical and horizontal) displacement variances, implying smaller probabilities for lateral departures from the mean flow trajectory. Smaller e limits lateral spread, and increases the probability of particle to enter $\boldsymbol{\Omega}^*$, sooner or later, and to trigger HSHM. The effect could also be viewed as a channeling effect of

sorts: smaller e implies Y blocks of small aspect ratio (i.e., long but thin elements), which provide fast tracks for particles when defined by high Y values, while blocking lateral spreads when defined by low Y values.

There are a few additional things to note here for completeness. First, $\boldsymbol{\Omega}^*$ in the present analysis is located downstream from the source, along with the mean trajectory of the solute displacement. We expect different results in situations where $\boldsymbol{\Omega}^*$ is positioned at an offset with respect to the mean flow direction. Second, we note that the analytical models used to compute the displacement statistics are formally limited to smaller variance ($\sigma_Y^2 < 1$), although they are shown to provide good approximations for large variances (Bellin et al., 1992). Third, the stochastic formulation provides the theoretical and computational formalism for conditioning the probabilities on in-situ measurements (Copty et al., 1993; Ezzedine & Rubin, 1996; Hubbard et al., 1997; Maxwell et al., 1999; Rubin, 1991a; Rubin et al., 1992; Rubin & Dagan, 1992) as well as on information borrowed from similar sites (Li et al., 2018; Cucchi et al., 2019).

2.8 Discussion and Summary

In this chapter, we developed a general stochastic framework that could be used to characterize the spatiotemporal distribution of environmental Hot Spots Hot Moments (HSHMs), with groundwater applications. The stochastic formulation is built around the following principles:

- The HSHMs are defined as random variables and the goal is to derive their stochastic distribution in terms of the relevant processes and attributes.
- HSHMs processes cover the dynamic components of the HSHMs. An example could be the transport of solutes and reactants. HSHMs attributes refer to the static components of the HSHMs, e.g., in situations related to the nitrogen cycles, attributes could represent pyrite concentrations or naturally-reducing zones. HSHMs could be defined through the confluence of a variety of contributors, both static and dynamic.
- The processes and attributes are modeled as stochastic processes and random variables, respectively, based on the underlying physics.
- The static contributors are modeled stochastically using geostatistical space random functions.
- The dynamic contributors are modeled stochastically using probability distribution functions derived from the underlying mathematical-physical models.
- Several HSHMs categories are defined, based on the contributing factors, as follows: HSHMs defined by dynamic contributors only, HSHMs defined by static contributors, and most commonly, HSHMs requiring the coupling of static and dynamic contributors. The HSHMs stochastic formulations are expressed in terms of the stochastic formulations of the relevant contributors.
- We provided a detailed review of multiple HSHMs and showed how they relate to our definitions.

The framework we proposed in this chapter is advantageous in that it allows to calculate the uncertainty associated with HSHMs based on the uncertainty associated with its contributors. Additionally, it provides a formalism, well established by Bayesian theory, for conditioning the HSHM probabilities on *in-situ* measurements as well as on information borrowed from geologically and otherwise similar sites.

We demonstrated our proposed approach through applications in the area of subsurface transport and hydrogeology, focusing on the impacts of subsurface heterogeneity on HSHMs. We analyzed, quantitatively, how subsurface heterogeneity of the conductivity field controls the

HSHM statistics, for example, the time expected for the probability of the HSHM to occur to reach a-priori set thresholds or time to peak probability.

Lastly, as mentioned both here and in previous studies, statistical methods for quantifying the occurrences of HSHMs and the associated uncertainties are needed to advance our understanding of the mechanisms that cause HSHMs, as well as to enhance our ability to predict HSHMs and manage their consequences.

Chapter 3

A Deep-Learning Hybrid-Predictive-Modeling Approach for Estimating Evapotranspiration and Ecosystem Respiration and Assessing Watershed Hot Spots and Hot Moments

3.1 Introduction

Evapotranspiration (ET) and ecosystem respiration (R_{ECO}) are key components of ecosystem water and carbon cycles. ET is an important link between the water and energy cycles: dynamic changes in ET can affect precipitation, soil moisture, and surface temperature, leading to uncertain feedbacks in the environment (Jung et al., 2010; Seneviratne et al., 2006; Teuling et al., 2013). Thus, quantifying ET is particularly essential for improving our understanding of water and energy interactions and watershed response to abrupt and gradual changes in climate, which is critical for water resources management, agriculture, and other societal benefits (Anderson et al., 2012; Jung et al., 2010; Rungee et al., 2019; Viviroli et al., 2007; Viviroli & Weingartner, 2008). R_{ECO} describes the sum of autotrophic respiration and respiration by heterotrophic microorganisms in a specific ecosystem and plays a vital role in the response of terrestrial ecosystem to global change (Jung et al., 2017; Reichstein et al., 2005; Xu et al., 2004). As long term exchanges in R_{ECO} have pivotal influences over the climate system (Cox et al., 2000; Gao et al., 2017; IPCC, 2019; Suleau et al., 2011), approaches are needed to estimate and monitor R_{ECO} over relevant spatiotemporal scales. As described below, there are many different strategies for measuring and estimating ET and R_{ECO}, each of which has advantages and limitations. The motivation for this chapter is the recognition that current methods cannot provide ET and R_{ECO} at space and time scales needed to improve prediction of changing terrestrial system behavior, particularly in challenging mountainous watersheds.

Several ground-based approaches have been used to provide $in\ situ$ estimates or measurements of ET and R_{ECO}. Ground based flux chambers capture and measure trace gases emitted from the land surface, which can be used to estimate ET and R_{ECO} (Livingston & Hutchinson, 1995; Pumpanen et al., 2004). However, the microclimate of the environment is affected by the chamber, and the laborious acquisition process and small chamber size typically leads to information with coarse spatiotemporal resolution (Baldocchi, 2014). The eddy covariance method uses a tower with installed instruments to autonomously measure fluxes of trace gases between ecosystem and atmosphere (Baldocchi, 2014; Wilson et al., 2001). The covariance between the vertical velocity and mixing ratios of the target scalar is computed to obtain the fluxes of carbon, water vapor, and other trace gases emitted from the land surface. ET is then calculated from the latent heat flux, and R_{ECO} is calculated from the net carbon fluxes using night-time or daytime partitioning approaches (van Gorsel et al., 2009; Lasslop et al., 2010; Reichstein et al., 2005). The spatial footprint of obtained fluxes is on the order of hundreds of meters, and the temporal resolution of the measurements range from hours to decades (K. B. Wilson et al., 2001). Such *in situ* measurements of fluxes have been integrated into the global network of Ameriflux (http://ameriflux.lbl.gov/) and FLUXNET (https://FLUXNET.fluxdata.org/), where such data have strongly supported scientists in process understanding and model development. Given the cost, efforts, and power required to install and maintain a flux tower, eddy covariance towers are typically sparse relative to the scale of study sites used to address ecosystem questions. Additionally, the location of a flux tower within a watershed greatly influences measurement representativeness. For example, eddy covariance towers are usually installed at valley bottoms of mountainous watersheds (Strachan et al., 2016), and estimates obtained there may not be representative of fluxes across a range of elevations or slope aspects within the watershed. The limited number of towers and their limited ability to sample different portions of a watershed thus limit the usefulness of flux towers for estimating ET and R_{ECO} in high resolution over space and time.

Physically-based models, which numerically represent land-surface energy and water balance, have also been used to estimate ET and R_{ECO} (Tran et al., 2019). These physically-based models solve physical equations to simulate the exchanges of energy, heat, water and carbon across atmosphere-canopy-soil compartments. Examples include the Community Land Model (CLM, Oleson et al., 2013). Performance of these models depend on the accuracy of inputs and parameters, such as soil type and leaf area index, which can be difficult to obtain at sufficiently high spatiotemporal resolution. The lack of measurements to infer parameters needed for models often leads to large discrepancies between model-based and flux-tower-based ET and R_{ECO} estimates. Conceptual model uncertainty inherent in mechanistic models can also lead to ET and R_{ECO} estimation uncertainty and errors. For example, Keenan et al. (2019) suggested that current terrestrial carbon cycle models neglect inhibition of leaf respiration that occurs during daytime, which can result in a bias of up to 25%. These conceptual uncertainties, in addition to data sparseness and data uncertainty, further limit the applicability of physically-based models to estimate ET and R_{ECO} at high spatiotemporal scales. Semi-analytical formulations based on combinations of meteorological and empirical parameters provide a reference condition for the water and energy balance. Examples used to estimate potential ET include the Budyko framework and its extensions (Budyko, 1961; Greve et al., 2015; Zhang et al., 2008); the Penman-Monteith's equation (Allen et al., 1998), and the Priestley-Taylor equation (Priestley and Taylor, 1972). Actual ET can then be approximated by multiplying a coefficient associated

with water deficit (De Bruin, 1983; Williams & Albertson, 2004). However, even with these empirical formulations many attributes are still difficult to obtain globally at high temporal scales, such as water-vapor deficit, leaf area index, and aerodynamic conductance of different plants.

Remote sensing products, such as Landsat imagery (Irons et al., 2012) and the moderate-resolution imaging spectroradiometer (MODIS, NASA. 2008), have also been integrated to estimate ET and R_{ECO} with empirical, statistical, or semi-physical relations (Abatzoglou et al., 2014; Daggers et al., 2018; Mohanty et al., 2017; Paca et al., 2019). Due to the high spatial coverage of remote sensing products, global-scale estimates of ET and R_{ECO} have become feasible. For example, Ryu et al. (2011) proposed the Breathing Earth System Simulator approach, which integrates mechanistic models and MODIS data to quantify ET and GPP with a spatial resolution of 1-5 km and a temporal resolution of 8 days. Ai et al. (2018) extracted enhanced vegetation index, fraction of absorbed photosynthetically active radiation, and leaf area index from the MODIS dataset—and used the rate-temperature curve and strong correlations between terrestrial carbon exchange and temperature to estimate R_{ECO} at 1 km spatial resolution and 8-day temporal resolution. Ma et al. (2018) developed a data fusion scheme that fused Landsat-like-scale datasets and MODIS data to estimate ET and irrigation water efficiency at a spatial scale of ~100 meters. However, even though remote sensing data cover large areas of the earth surface, they typically do not provide information over both high spatial and temporal resolution, and are also subject to cloudy conditions. For example, Landsat has average return periods of 16 days with a spatial resolution of 30 m (visible and near-infrared), whereas MODIS has 1-2 days temporal resolution with a 250 m or 1 km spatial resolution depending on the sensors. These resolutions are typically too coarse to enable exploration of how aspects such as plant phenology, snowmelt, and rainfall impact integrated ecosystem water and energy dynamics.

Combining machine-learning models with remote sensing products and meteorological inputs offers another option for large-scale estimation of ET and R_{ECO}. Remotely sensed data are good proxies for plant productivity and can be easily implemented into machine-learning models for ET and R_{ECO} estimation, such as for an enhanced vegetation index, land surface water index and NDVI (Gao et al., 2015; Jägermeyr et al., 2014; Migliavacca et al., 2015). Li and Xiao (2019) developed a data-driven model for gross primary production at a spatial and temporal resolution of $0.05°$ and 8 days using MODIS and meterological reanalysis data. Berryman et al. (2018) demonstrated a Random Forest model to predict growing season soil respiration from subalpine forests in the Southern Rocky Mountains ecoregion. Jung et al. (2009) developed a model tree ensemble approach to upscale FLUXNET data, where they have successfully estimated ET and GPP. Other methods have used support vector machines, artificial neural networks, random forest, and piecewise regression (Bodesheim et al., 2018; Metzger et al., 2013; Xiao et al., 2014; T. Xu et al., 2018). These models were trained with ground-measured flux observations and other variables, and then applied to estimate ET over continental or global scales with remote sensing and meteorological inputs. Some of the most important inputs include the enhanced vegetation index, aridity index, temperature, and precipitation. However, the spatiotemporal resolution of these approaches is constrained by the resolution of remote sensing products and meteorological inputs. Additionally, parameters such as leaf area index, cloudiness, and the vegetation types required by those models may not be available at the required resolution, accuracy or location. For example, in systems that have significant elevation gradients, errors

may result when valley-based FLUXNET data are used for training and then applied to hillslope or ridge ET and R_{ECO} estimation

Development of hybrid models that link direct measurements and/or mechanistic models with data-driven methods can benefit ET and R_{ECO} estimation (Reichstein et al., 2019). While remote sensing data that cover large regions provide promise for informing models, quantitative interpretation of these data needed for input into mechanistic models is still challenging (Reichstein et al., 2019). Physically-based models can provide estimates of ET and R_{ECO}, but the estimate error can be high, owing to parametric, structural, and conceptual uncertainties as described above. Hybrid data-driven frameworks are potentially advantageous because they enable the integration of remote sensing datasets, meteorological forcings, and mechanistic model outputs of ET and R_{ECO} into one model. Machine-learning approaches are then applied to extract the spatiotemporal patterns for ET and R_{ECO} prediction. Hybrid models can utilize the high spatial coverage of remote sensing data (e.g., 30 m of Landsat) and high temporal resolution of direct measurement from flux towers or simulation results from mechanistic models (e.g., daily or hourly scales), thus providing alternative approaches for next-stage, more accurate estimation of ET and R_{ECO} at greater spatial and finer temporal scales—and enhancing our process understanding of water and carbon cycling under climate change.

In this chapter, we developed a hybrid predictive modeling approach (HPM) to better estimate ET and R_{ECO} over space and time with easily acquired meteorological data (i.e., air temperature, precipitation and radiation) and remote sensing products (i.e., NDVI). HPM is hybrid as it can use deep learning models to integrate direct measurements from flux towers and physically-based model results (e.g., CLM) with meteorological and remote sensing inputs to capture the complex physical interactions within the watershed ecosystem. After development, we validated HPM performance with the FLUXNET dataset and benchmarked the CLM model at select sites. We then used the HPM for ET and R_{ECO} estimation at the mountainous East River Watershed in CO and investigated how small-scale heterogeneity influences ET and R_{ECO} dynamics.

3.2 Site and Data Description

Various sites were selected to develop and validate our approaches. We focused on mountainous watersheds because they provide significant water resources to the world (Viviroli et al., 2007), but also included sites to test HPM's capabilities under different climate and vegetation conditions. Mountainous watersheds are very sensitive to changes in temperature and precipitation patterns, which can significantly threaten downgradient water resources and associated societal benefits (Breshears et al., 2005; Ernakovich et al., 2014; Immerzeel et al., 2019). As mountainous regions are extremely important for regional and global assessment and management of water resources and carbon storage and emission (Knowles et al., 2015; Schimel et al., 2002), accurate estimation of ET and R_{ECO} in these regions is critical, though challenging due to complex heterogeneity and complicated interactions among the hydrosphere, biosphere and the atmosphere (Pelletier et al., 2018; Speckman et al., 2015). Thus, we focused on estimating ET and R_{ECO} at various sites along the Rocky Mountains, including the East River Watershed (Hubbard et al., 2018) of the Upper Colorado River Basin.

3.2.1 FLUXNET Stations and Ecoregions

Eight FLUXNET stations were selected for this study (Table 3.1 and Figure 3.1), which cover a wide range of climate and vegetation types. These stations have elevations from 129 m (US-Var) to 3050 m (US-NR1), mean annual air temperature from 1.5℃ (US-NR1) to 17.92℃

(US-SRM), and mean annual precipitation from 320 mm (US-Whs) to 800 mm (US-NR1). These FLUXNET stations also cover a wide range of vegetation types (i.e., evergreen forest, deciduous forest, and shrublands). As indicated by Hargrove et al. (2003), FLUXNET stations provide a good representation of different ecoregions, which are areas that display recurring patterns of similar combinations of soil and landform characteristics (Omernik, 2004). Omernik & Griffith. (2014) delineated the boundaries of ecoregions through pattern analysis that consider the spatial correlation of both physical and biological factors (i.e., soils, physiography, vegetation, land use, geology and hydrology) in a hierarchical level. FLUXNET stations considered in this study are mainly located in 4 unique ecoregions (Table 3.1). As is described below, we developed local-scale (i.e., point scale) HPM that are representative for different ecoregions using data provided at these FLUXNET stations to estimate ET and R_{ECO}, and validated the HPM estimates with measurements from stations within the same ecoregion.

3.2.2 SNOTEL Stations

For reasons described below, we performed a deeper exploration within one of the mountainous watershed sites (the East River Watershed of the Upper Colorado River Basin), which is located in the "western cordillera" ecoregion. At this site, we utilized meteorological forcings data from three snow telemetry (SNOTEL) stations. These sites include the Butte (ER-BT, id: 380), Porphyry Creek (ER-PK, id: 701) and Schofield Pass (ER-SP, id: 737) sites. A CLM model was developed at these SNOTEL stations that provides physically-model-based ET estimation (Tran et al., 2019). The consideration of SNOTEL stations in this study enabled us to explore and compare how heterogeneity in meteorological forcing attributes control ET and R_{ECO} dynamics as well as provide cases for further validating our proposed approach. Table 3.1 summarizes the SNOTEL stations used in this study and the corresponding climate characteristics. Figure 3.1 shows the geographical locations of FLUXNET and SNOTEL stations selected in this study.

Table 3.1 Summary of FLUXNET stations and SNOTEL stations information. * denotes SNOTEL stations and all others are FLUXNET stations. Dfc, Bsk, Csa represent subarctic or boreal climates, semi-arid climate, Mediterranean hot summer climates, respectively. ENF, DBF, WSA, GRA, and OSH represent evergreen needleleaf forest, deciduous broadleaf forests, woody savannas, grasslands, open shrubland, respectively.

Site ID	Site Name	Latitude, Longitude	Elevation (m)	Mean Annual temperature (℃)	Mean Annual Precipitation (m)	Climate Koeppen	Vegetation IGBP	Ecoregions (Level II)	Period of Record
US-NR1	Niwot Ridge	(40.0329, -105.5464)	3050	1.5	800	Dfc	ENF	Western Cordillera	2000-2014
CA-Oas	Saskatchewan-Aspen	(53.6289, -106.1978)	530	0.34	428.53	Dfc	DBF	Boreal Plain	1997-2010
CA-Obs	Saskatchewan-Black Spruce	(53.9872, -105.1178)	628.94	0.79	405.6	Dfc	ENF	Boreal Plain	1999-2010
US-SRM	Santa Rita Mesquite	(31.8214, -110.8661)	1120	17.92	380	Bsk	WSA	Western Sierra Madre Piedmont	2005-2015
US-Ton	Tonzi Ranch	(38.4316, -120.9660)	177	15.8	559	Csa	WSA	Mediterranean California	2002-2015
US-Var	Vaira Ranch-lone	(38.4133, -120.9507)	129	15.8	559	Csa	GRA	Mediterranean California	2002-2015
US-Whs	Walnut Gulch Lucky Hills Shrub	(31.7438, -110.0522)	1370	17.6	320	Bsk	OSH	Western Sierra Madre Piedmont	2008-2015
US-Wkg	Walnut Gulch Kendall Grasslands	(31.7365, -109.9419)	1531	15.64	407	Bsk	GRA	Western Sierra Madre Piedmont	2005-2015

ER-BT*	East River-Butte	(38.894, -106.945)	3096	2.38	821	Dfc	N/A	Western Cordillera	1995-2017
ER-SP*	East River-Schofield Pass	(39.02, -107.05)	3261	2.46	1064	Dfc	N/A	Western Cordillera	1995-2017
ER-PK*	East River-Porphyry Creek	(38.49, -106.34)	3280	1.97	574	Dfc	N/A	Western Cordillera	1995-2017

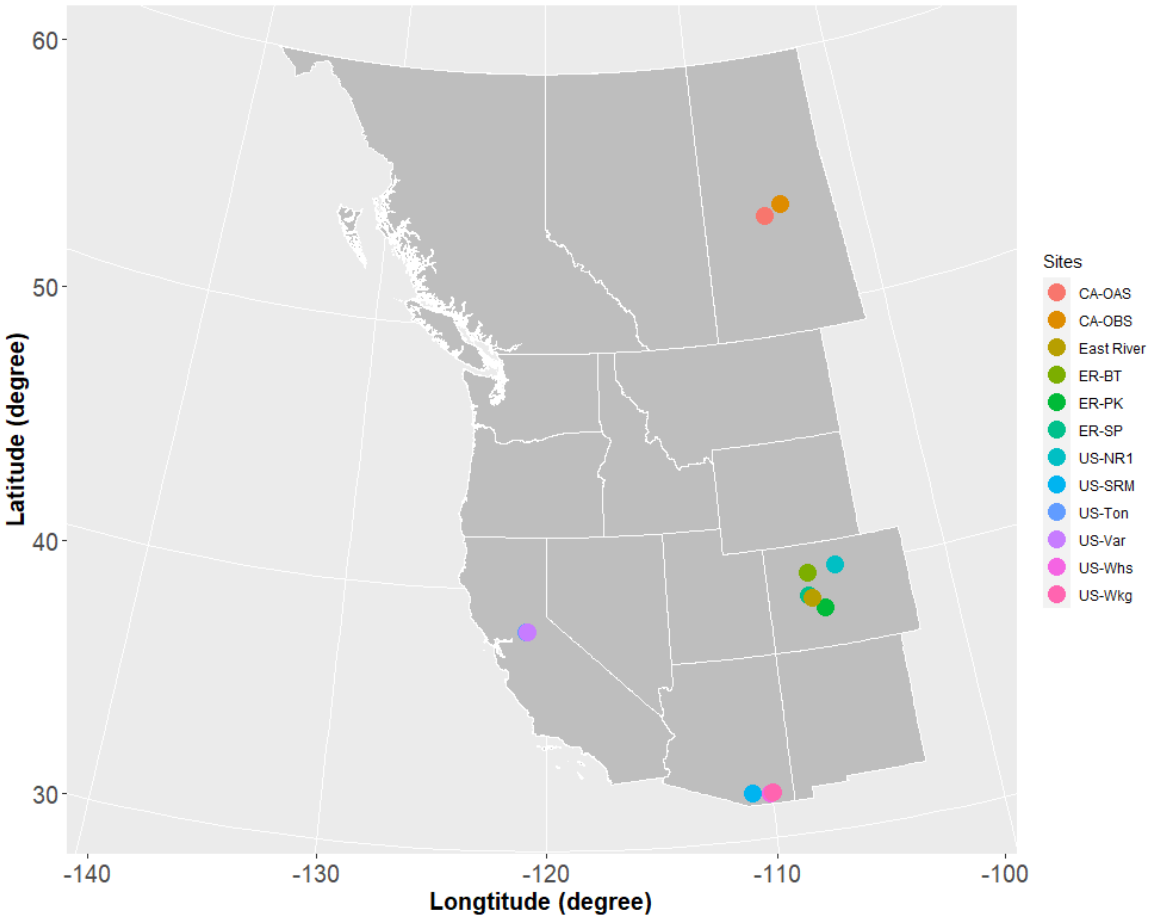

Figure 3.1 Location of sites considered in this study. Note: US-Ton and US-Var; US-Whs and US-Wkg are at the same locations. East River Watershed is located next to ER-BT. The white lines delineate Western US states and Canadian provinces.

3.2.3 East River Watershed and Previous Analyses

Data from the East River Watershed were used to explore how ET and R_{ECO} dynamics estimated from the developed HPM vary with different vegetation and meteorological forcings. The East River Watershed is located northeast of the town of Crested Butte, Colorado. This watershed has an average elevation of 3266 m, with significant gradients in topography, hydrology, geomorphology, vegetation, and weather. The watershed has a mean annual temperature around 0℃ , with an average of 1200 mm yr^{-1} total precipitation (Hubbard et al., 2018). Consisting of montane, subalpine, and alpine life zones, each with distinctive vegetation biodiversity, the East River Watershed is a testbed for the US Department of Energy Watershed Function Scientific Focus Area Project, led by the Lawrence Berkeley National Laboratory

(LBNL; Hubbard et al., 2018). The project has acquired a range of datasets, including hydrological, biogeochemical, remote sensing, and geophysical datasets.

Recently completed studies at the East River Watershed were used in this study to inform HPM and to assess the results. For example, physically-model-based estimations of ET at this site (Tran et al., 2019) were used herein for HPM development and validation. Falco et al. (2019) used machine-learning-based remote sensing methods to characterize the spatial distribution of vegetation types, slopes, and aspects within a hillslope at the East River Watershed, which were used with obtained HPM estimates to explore how small-scale vegetation heterogeneity influences ET and R_{ECO} dynamics. To perform this assessment, we computed the spatial distribution of vegetation types at watershed scale, based on Falco et al. (2019), and selected 16 locations within the East River Watershed having different vegetation types and slope aspects. These 16 locations were chosen at a level to be distinguishable by Landsat images and maintain the same vegetation type (given a spatial resolution of 30 m), and also possess small-scale heterogeneity. A summary of the locations is presented in Table 3.2; the spatial distribution of the locations is shown in Figure 3.3.2.

Table 3.2 Location and vegetation types of East River Watershed sampling points (Figure 3.2)

Easting (m)	Northing (m)	Vegetation Type	Aspect	Elevation (m)
327085	4309878	Deciduous Forest	South	2983
326288	4312504	Deciduous Forest	South	3177
330012	4313132	Deciduous Forest	North	3108
326854	4313192	Deciduous Forest	South	3098
328246	4312832	Meadow	South	3095
327010	4315059	Meadow	South	2790
328738	4306139	Meadow	North	2890
334270	4309465	Meadow	North	2929
333406.5	4308340	Riparian Shrubland	South	2760
327846	4312497	Riparian Shrubland	South	2723
334641	4305632	Riparian Shrubland	North	2740
330760	4310097	Riparian Shrubland	South	2855
329573	4314569	Evergreen Forest	South	3026
333106	4307313	Evergreen Forest	North	3102
325056	4310456	Evergreen Forest	South	2961
335141	4309614	Evergreen Forest	North	3131

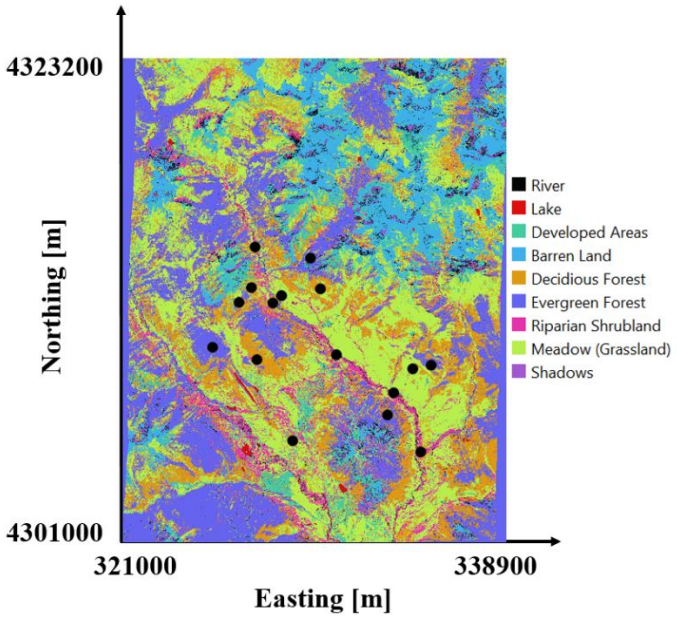

Figure 3.2 Vegetation classification of the East River, CO Watershed from Falco et al. (2019). East River sites selected in this study are denoted by black circles.

3.2.4 Data Collection and Processing

To enhance transferability of the developed HPM strategy to less intensively characterized watersheds, we selected only "easy to measure" or "widely available" attributes, such as precipitation, temperature, radiation and NDVI, as inputs to the HTM model. The data sources used for these inputs include FLUXNET data (https://fluxnet.fluxdata.org/), SNOTEL data (https://www.wcc.nrcs.usda.gov/snow/) and developed CLM model (Tran et al., 2019) at SNOTEL stations, DAYMET meteorological inputs (Thornton et al., 2017) and remote sensing data from Landsat imageries (Irons et al., 2012).

A variety of measured data and model outputs were used to train and validate HPM. We obtained daily meteorological data, including air temperature, precipitation, radiation, ET, and R_{ECO} data, from the FLUXNET database at the selected FLUXNET sites. The pipeline of data processing for FLUXNET dataset is provided at https://FLUXNET.fluxdata.org/. ET data for US-NR1 were cleaned following the procedures presented in Rungee et al. (2019). The meteorological data were used as inputs for HPM development, and ET and R_{ECO} data from these sites were used for HPM validation. At the three selected SNOTEL stations, we obtained air temperature, precipitation, and snow-water-equivalent data from the SNOTEL database. Air temperature data at these three SNOTEL stations were processed following Oyler et al. (2015), given potential systematic artifacts. Snow-water-equivalent data are not easily acquired, and thus were not considered as inputs for HPM. However, a categorical variable was constructed to assimilate information regarding snow (Section 3.2.1). CLM models were generated following Tran et al. (2019) for the SNOTEL stations and US-NR1 to assess the spatiotemporal variability of ET at the East River Watershed and for training and validating HPM (Section 4.3). The DAYMET dataset (Thornton et al., 2017) provided gridded daily weather-forcings-attribute estimates at a 1 km spatial resolution. We obtained the incident radiation data from DAYMET at the SNOTEL stations as inputs for HPM. For the East River Watershed sites, meteorological forcings data, including air temperature, precipitation and radiation, were also obtained from

DAYMET. The low spatial resolution of DAYMET data introduces uncertainty in HPM estimation of ET and R_{ECO}, which will be discussed in the following sections. We calculated the NDVI time series from the red band (RED) and near-infrared band (NIR) from Landsat 5, 7, and 8 images following Equation 3.1 at all selected FLUXNET sites, SNOTEL stations, and East River Watershed sites at a spatial scale of 30 m.

$$NDVI = \frac{NIR - RED}{NIR + RED} \tag{3.1}$$

Since cloud conditions can severely decrease data quality, we used the cloud-scoring algorithm provided in the Google Earth Engine to mask clouds in all retrieved data, only selecting the ones that had a simple cloud score below 20 to ensure data quality. Given the different calibration sensors used in Landsat 5, 7, and 8, we also followed the processes described in Homer et al. (2015) and Vogelmann et al. (2001) to keep NDVI computations consistent over time. Landsat satellites have a return period of 16 days, and thus we performed a reconstruction of NDVI time series to obtain daily scale time data (Section 3.2.2).

3.3 Hybrid Predictive Modeling Framework

In this section, we illustrate the steps for building an HPM model for ET and R_{ECO} estimation over time and space. Figure 3.3 presents the general framework of HPM, which includes modules for data preprocessing, model development, model validation, and predictive modeling.

3.3.1 Model Framework

HPM establishes relationships among meteorological forcings attributes, NDVI, ET, and R_{ECO} (Figure 3.3). Both input data (e.g., meteorological forcings) and output data (ET and R_{ECO}) used for training and validation are preprocessed for gap filling, smoothing, and data updating. HPM "learns" the complex space-time relationship among meteorological forcings, NDVI, ET, and R_{ECO} using a deep-learning-based module (deeply connected neural networks and a long short-term memory recurrent neural network). HPM then can be used for ET and R_{ECO} estimation at sparsely monitored watersheds. Individual HPM models can be trained in two different ways using ET and R_{ECO} information: with data obtained from flux towers ("data-driven HPM") or with outputs from 1-D physically-based models ("mechanistic HPM"). In both cases, the models obtained with local data are then used to estimate ET and R_{ECO} at other sites in the same ecoregion (see Section 2.1). For ecoregions not represented by FLUXNET sites, it is necessary to develop mechanistic HPM that enables ET and R_{ECO} estimation over space and time.

HPM has several additional modules, including model development, model validation, and model prediction modules. In the HPM model development module, deep-learning algorithms are trained with input features and response data until a pre-defined "stopping criteria" (e.g., root mean squared error, RMSE) is met, indicating subsequent training would lead to minimal improvement. In the validation module, estimation outputs from the "trained HPM models" are compared with other ET and R_{ECO} data obtained from other independent sites or mechanistic models within the same ecoregion. Statistical measures, including adjusted R^2 and mean absolute error (MAE), are computed to evaluate the performance of HPM models. In the predictive model module, meteorological forcings data and remote sensing data are processed at target sites of interest, and the validated HPM model is used to estimate ET and R_{ECO} at these sites. ET and R_{ECO} outputs estimated from HPM at sparsely monitored watersheds then provide alternative datasets for process understanding within the target watersheds.

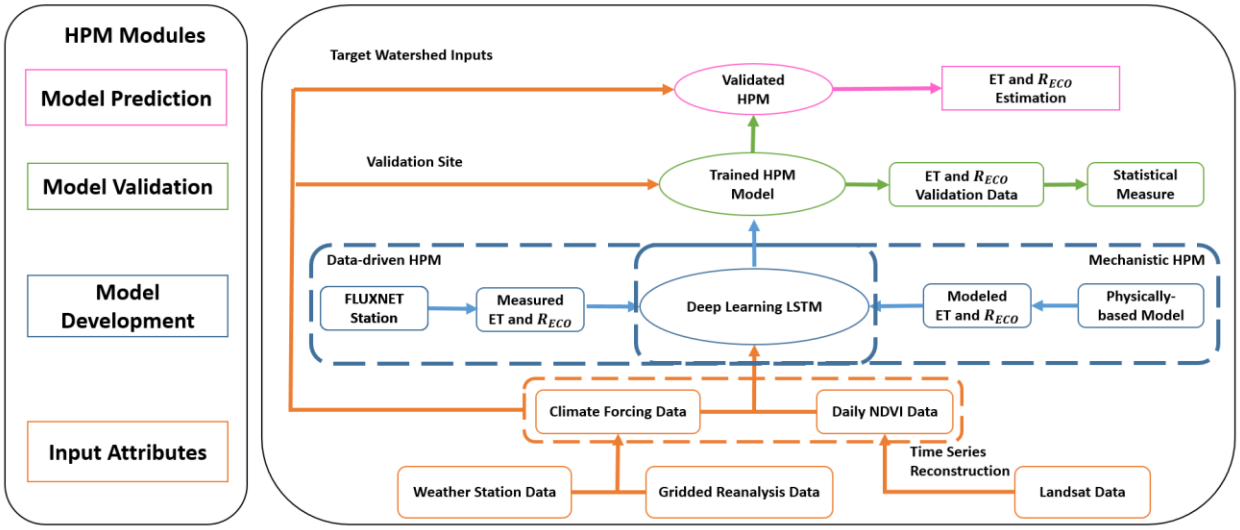

Figure 3.3 Hybrid Predictive Model Framework. The HPM model mainly consists of four modules: Input Attributes, Model Development, Model Validation and Model Prediction, represented by rectangles with colors. Arrows represent the linkages among different modules. Choices of data-driven HPM or mechanistic HPM depend on the ecoregion of target watershed and data availability.

Long short-term memory (LSTM, Hochreiter & Schmidhuber, 1997) is capable of identifying long-term dependencies between climate and environmental data. For example, Kratzert et al. (2018) successfully used LSTM to learn the long-term dependencies in hydrological data (e.g., storage effects within catchments, time lags between precipitation inputs and runoff generation) for rainfall-runoff modeling. Kratzert et al. (2019) further developed predictive models with LSTM trained on gauged sites to provide streamflow estimations at ungaged basins. LSTM has also been used for gap filling in hydrological monitoring networks in the spatiotemporal domain (Ren et al., 2019). In this study, the outputs (ET or R_{ECO}) denoted as y are predicted from the input $x = [x_1, x_2, \dots, x_T]$, consisting of the last Tconsecutive time steps of attributes, such as meteorological forcings attributes (e.g., air temperature and precipitation) and remote sensing attributes (i.e., NDVI). In a recurrent neural network (RNN), h_t represents the internal state at every time step t that takes in current input value x_t and previous internal state h_{t-1}, and is recomputed along the time axis using the following equation:

$$h_t = g(Wx_t + Uh_{t-1} + b), \tag{3.2}$$

where g represents the hyperbolic tangent activation function, W and U are trainable weight metrices of the hidden state h, and b is a bias vector. W, U and b are all trainable through optimization. LSTM introduces the cell state c_t, which makes LSTM powerful in identifying long-term dependencies in a statistical manner. The cell state c_t has three gates structures, including "forget gates" (which determine what information from previous cell states will be forgotten), "input gates" (which determine what information will be conveyed from the forget gate) and "output gates" (which return information from cell state c_t to a new state h_t). With these gate structures, the cell state c_t controls what information will be forgotten, conveyed, and updated over time. The forget gate is formulated as follows:

$$f_t = \sigma\left(W_f x_t + U_f h_{t-1} + b_f\right), \tag{3.3}$$

where f_t results in a value between 0 and 1 indicating the degree of information to be forgotten; σ is the logistic sigmoid function, $and\ W_f, U_f$ and b_f are trainable parameters. Next, the input

gate decides which values will be updated in the current cell state, and creates a vector of candidate values $\widetilde{c_t}$ in the range of (-1, 1) through a $tanh$ layer, which will be used to update the current state. With the candidate values calculated from the current state, and the information conveyed from the forget gate, we can calculate the current cell state as follows:

$$i_t = \sigma(W_i x_t + U_i h_{t-1} + b_i), \tag{3.4}$$

$$\widetilde{c_t} = tan\,h(W_{\tilde{c}} x_t + U_{\tilde{c}} h_{t-1} + b_{\tilde{c}}), \tag{3.5}$$

$$c_t = f_t * c_{t-1} + i_t * \widetilde{c_t}, \tag{3.6}$$

where i_t is the input gate that defines which information of $\widetilde{c_t}$ will be used to update the current cell state and is in the range of (0, 1); c_t represents the current cell state; and $W_{\tilde{c}}, U_{\tilde{c}}, b_{\tilde{c}}, W_i, U_i, and\ b_i$ are trainable parameters. Finally, the output gate o_t controls the information of cell state c_t to a new hidden state h_t, which is computed using the following equation:

$$o_t = \sigma(W_o x_t + U_o h_{t-1} + b_o), \tag{3.7}$$

$$h_t = \tanh(c_t) * o_t, \tag{3.8}$$

With the new hidden state calculated, ET and R_{ECO} can be calculated using a one unit dense layer:

$$y_t = W_d h_t + b_d, \tag{3.9}$$

where W_d and b_d are additional trainable parameters. In summary, the LSTM unit calculates the internal state using current meteorological forcings and remote sensing data at every time step. The forget gate, input gate, and output gate decide what information from previous time steps will be kept, updated, and conveyed to the new hidden state. Finally, with a single dense layer, the algorithm will output ET and R_{ECO} estimation from the trained model.

A 70%-30% sequentially split between training and validation time series data was applied here, where the first 70% of the data were used for HPM development as a learning process, and 30% of the data were used as validation sets at individual sites. At the East River Watershed, HPM results were also validated with benchmark CLM outputs from Tran et al. (2019) and FLUXNET measurements. We used the mean absolute error (MAE), and adjusted R^2 as the statistical measure to determine model performance.

$$MAE = \frac{\sum_{i=1}^{n} |y_{predict} - y_{measured}|}{n}, \tag{3.10}$$

$$R^2 = 1 - \frac{SSE}{SS}, \tag{3.11}$$

where SSE represents the sum of squared errors, SS is the sum of squares of the response attributes (i.e., ET or R_{ECO}), and n is the number of data points. In most models, the configuration of the neural networks includes a first LSTM layer with 50 units, a second LSTM layer with 25 units, and a dense layer with 8 units having L2 regularizers and a final output dense layer. Dropout layers are also embedded in the model to prevent overfitting. Other configurations of networks may provide better estimation results; however, they are not assessed in this study. More information about the LSTM-RNN method is provided by Olah (2015). Configuration of the deep-learning module is documented in Table 3.3

Table 3.3 Configuration of Deep-Learning Module

Layer	Output Shape	Parameters #	Note
LSTM	[50, 1]	11600	
LSTM	[25]	7600	
Dropout	[25]	0	Rate = 0.1
Dense	[8]	208	L2 regularizers, 0.01

Dropout	[8]	0	Rate = 0.1
Dense	[1]	9	Output Layer

3.3.2 Feature Selection

Given data availability and the practicability of applying HPM to estimate ET and R_{ECO} at sparsely monitored watersheds, we also selected, constructed, and augmented certain attributes as features for HPM.

In mountainous watersheds, snow dynamics significantly influence water and carbon fluxes. Because of the difficulties in measuring snow time series over space, we did not directly use attributes such as snow water equivalent as input to HPM. Instead, we separated precipitation data into snow (air temperature < 0) and rainfall (air temperature > 0). This is in line with what has been used in hydrological models such as CLM (Oleson et al., 2013). Note that for certain sites in this study, snow is not present (e.g., US-Ton). In order to capture the dynamics of snow processes, such as accumulation and melting, we constructed a categorical variable (sn), as follows:

$$\boldsymbol{sn} = \begin{cases} 0, during\ snow\ accumlation;\ \ SWE > 0\ and\ SWE < peak\ SWE \\ 1, during\ snow\ melting; SWE > 0\ and\ \ SWE \leq peak\ SWE \\ 2, no\ snow; SWE = \ 0 \end{cases}, \quad (3.12)$$

Since data on peak SWE are rarely available because of the difficulties in measuring snow, we also define a proxy categorical variable, ***sn***. When no SWE measurements were available, we estimated ***sn*** using air and soil temperature data following Knowles et al. (2016), who found significant correlations between the day of peak snow accumulation and first day of air temperature above 0 degrees Celsius, as follows:

$$\boldsymbol{sn} = \begin{cases} 0, during\ snow\ accumlation;\ \ Air\ Temperature < 0 \\ 1, during\ snow\ melting; Air\ Temperature > 0\ while\ Soil\ Temperature \leq 0, \\ 2, no\ snow; Air\ Temperature\ and\ Soil\ Temperature > 0 \end{cases} (3.13)$$

To mitigate the long return periods of satellites and the presence of clouds, we reconstructed daily NDVI values based on meteorological forcings data (e.g., air temperature, precipitation, radiation) using deep-learning recurrent neural networks, leading to estimates of NDVI at daily temporal resolution. For example, Figure 3.4 represents Landsat-derived NDVI and reconstructed NDVI values for two sites at the East River, CO watershed: Butte (ER-BT), and Schofield Pass (ER-SP). Figure 3.4 reveals that based on meteorological forcings data only, the reconstructions achieved an adjusted R^2 of 0.65. Though not ideal, as satellites continue to advance and more training data becomes available, the accuracy of NDVI temporal reconstruction will increase.

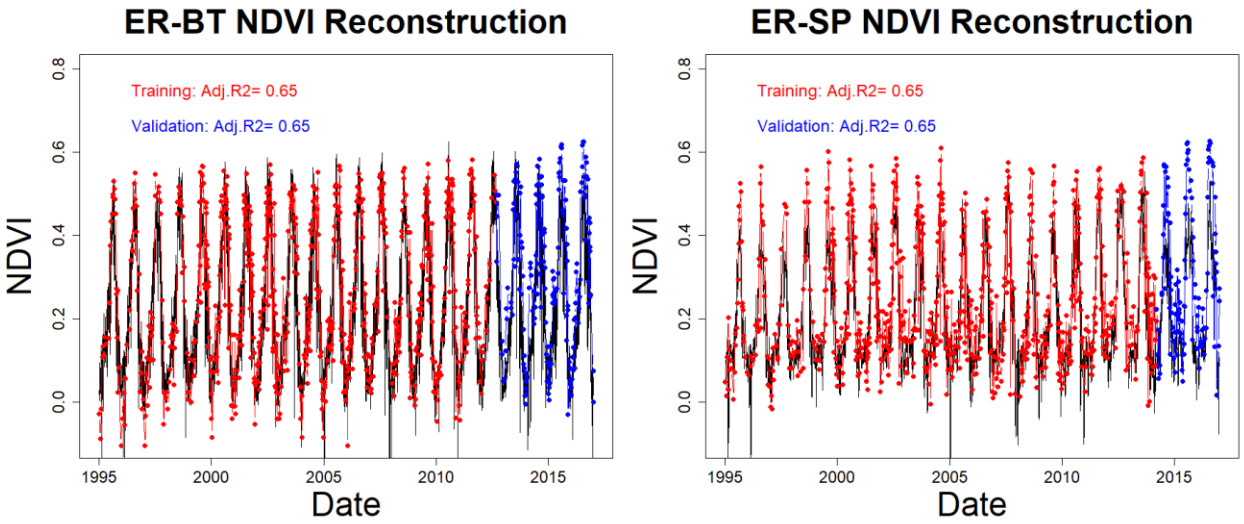

Figure 3.4 Temporal reconstruction of NDVI at ER-BT (left) and ER-SP (right). Black line represents reconstructed daily NDVI. Red points are used for training and blue points are used for validation

3.4. Results

We tested HPM's capabilities using different use cases to explore different conditions. First, we tested the capability of HPM to estimate long-term temporal dependency among meteorological forcings, ET, and R_{ECO} (presented in Section 3.4.1). Second, we validated HPM's capability to estimate the spatial distribution of ET and R_{ECO} over space in selected watersheds, where we developed HPM using existing FLUXNET data (data-driven HPM, Section 3.4.2) or outputs from a mechanistic model (physical-model-based HPM, Section 3.4.3). Third, HPM was used to estimate ET and R_{ECO} at selected sites within the East River Watershed and to distinguish how local factors (e.g., vegetation heterogeneity) influence ET and R_{ECO} dynamics (Section 3.4.4). These four use cases illustrate and demonstrate how HPM can be developed and applied at target watersheds, where data are sparse.

3.4.1 Use Case 1: ET and R_{ECO} Time Series Estimation with HPM Developed at FLUXNET Sites

Local HPMs were developed to estimate ET and R_{ECO} using flux tower data obtained from FLUXNET sites listed in Table 3.1. Attributes used to train these individual HPM are documented in Table 3.3.

Table 3.4 Attributes used for HPM development in Use Case 1

Site ID	Site Name	Attributes
US-NR1	Niwot Ridge	Air Temperature, precipitation, net radiation, sn, NDVI, soil temperature
CA-Oas	Saskatchewan-Aspen	Air Temperature, precipitation, net radiation, sn, NDVI, soil temperature
CA-Obs	Saskatchewan-Black Spruce	Air Temperature, precipitation, net radiation, sn, NDVI, soil temperature
US-SRM	Santa Rita Mesquite	Air Temperature, precipitation, net radiation, NDVI, soil temperature
US-Ton	Tonzi Ranch	Air Temperature, precipitation, net radiation, NDVI, soil temperature
US-Var	Vaira Ranch-lone	Air Temperature, precipitation, net radiation, NDVI, soil temperature
US-Whs	Walnut Gulch Lucky Hills Shrub	Air Temperature, precipitation, net radiation, NDVI, soil temperature
US-Wkg	Walnut Gulch Kendall Grasslands	Air Temperature, precipitation, net radiation, NDVI, soil temperature

The results, which are shown in Figure 3.5 and Table 3.4, reveal that the HPM approach was effective for estimating ET. Adjusted R^2 between the HTM estimates and flux tower

measurements are above 0.85 for all sites, and mean absolute errors are small at a level of ~0.2 mm/d. Figure 3.5 displays the estimation of ET from HPM US-NR1 and CA-OAS (other sites provided in supplementary material), and presents monthly mean ET values of measurements, HPM estimations, and differences. The long-term trends in ET are well captured by HPM. At larger temporal scales (monthly or yearly), HPM provides reasonable estimation of ET at these sites. However, short-term fluctuations during the summer are also not well captured by ET, specifically at California sites during the periods when plant transpiration and soil evaporation are constrained by soil moisture (Figure 3.3.A2 panel a).

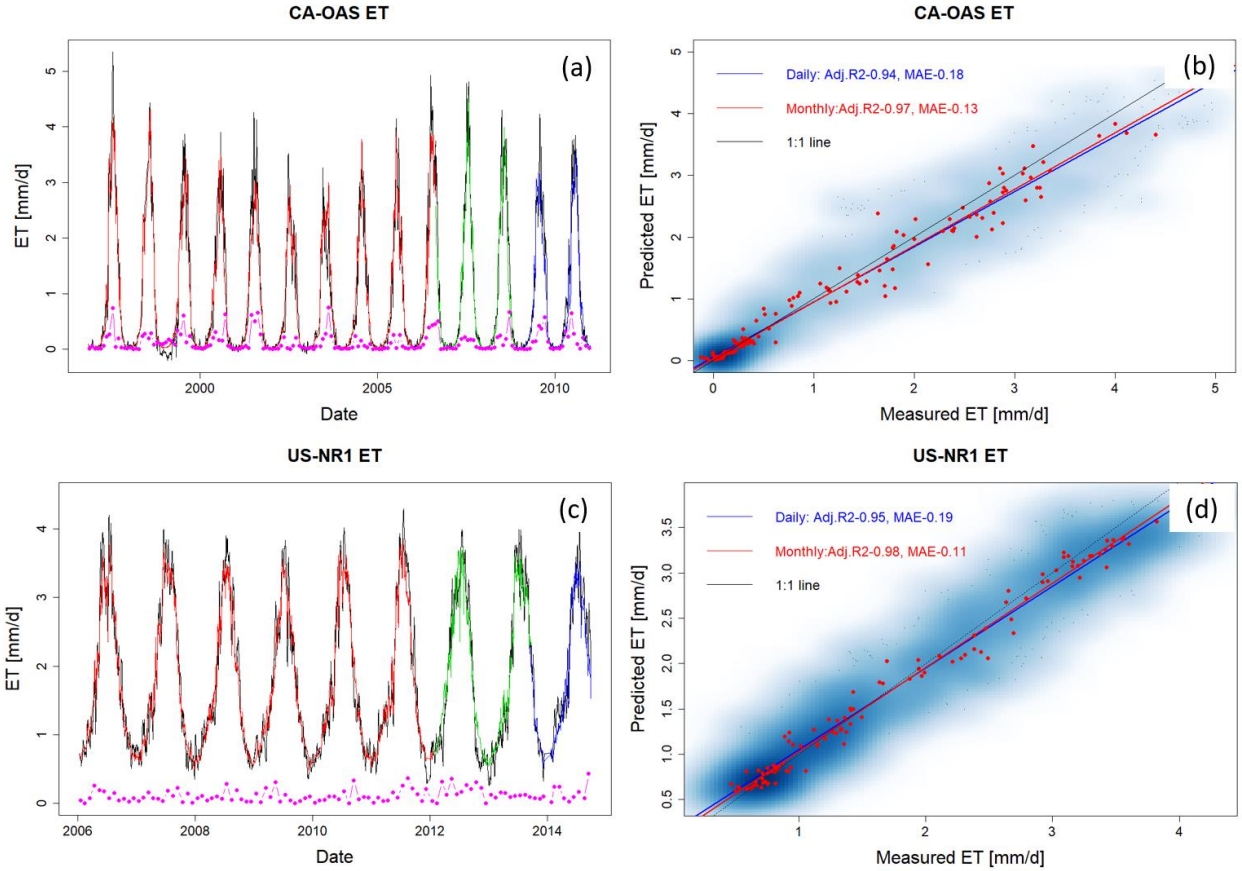

Figure 3.5 ET estimation with data from FLUXNET sites at CA-OAS and US-NR1. Panels (a) and (c) illustrate the daily estimation of ET with red, green, and blue lines representing data used for training, validation, and prediction, respectively, and the black line showing the eddy covariance measurements. Pink points describe monthly mean difference between HPM estimation and measured data. Panels (b) and (d) show the scatter plots of daily (blue) and monthly (red) ET. Darker blue clouds represent greater density of data points. Results for other sites are included in supplementary materials below (Figures A1 and A2).

Similarly, Table 3.4 and Figure 3.6 reveal that HPM was also effective in estimating R_{ECO}, leading to small *MAE* and adjusted R^2 of 0.8 between estimated and measured R_{ECO} except for US-Ton and US-Var. Figure 3.6 presents HPM-estimated R_{ECO} at US-NR1 and CA-OAS, with other sites presented in Figures A3 and A4. Long-term dynamics of R_{ECO} are also successfully captured by HPM; however, HPM underestimates R_{ECO} during peak growing seasons. For example, at US-NR1, error increased during the growing season, when estimates of R_{ECO} are smaller than measured R_{ECO}. While soil moisture can limit R_{ECO} during peak growing season

(Ng et al., 2014; Wang et al., 2014), the developed HPM does not include soil moisture as a key attribute. As such, HPM underestimates R_{ECO} during peak growing season, leading to higher MAE than other times of the year. In addition, HPM R_{ECO} estimation at US-Ton and US-Var show higher uncertainties (i.e., $MAE > 0.4$ and Adj. $R^2 < 0.8$), which also indicates that soil moisture data is necessary to increase R_{ECO} prediction accuracy in this ecoregion.

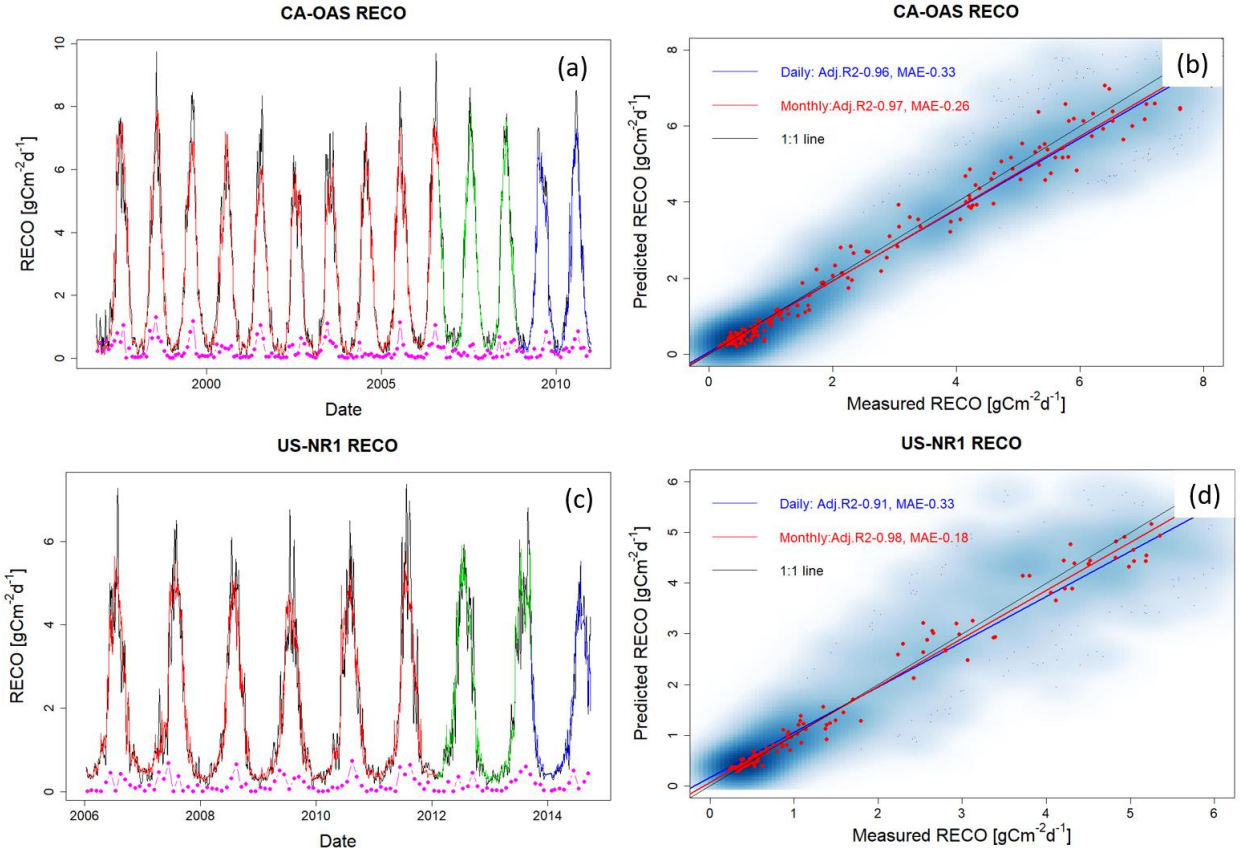

Figure 3.6 R_{ECO} estimation with data from FLUXNET sites at CA-OAS and US-NR1. Panels (a) and (c) present daily estimation of R_{ECO} with red, green, and blue lines representing data used for training, validation, and prediction, and the black line shows the eddy covariance measurements. Pink points describe monthly mean difference between HPM estimation and measured data. Panels (b) and (d) show the scatter plots of daily (blue) and monthly (red) R_{ECO}. Darker blue clouds represent greater density of data points.

Table 3.5 Statistical measures of HPM estimation of ET and R_{ECO}

Site ID	Train MAE -ET $[mm/d]$	Test MAE - ET $[mm/d]$	Train Adj. R^2 - ET	Test Adj. R^2 - ET	Train MAE $-R_{ECO}$ $[gCm^{-2}d^{-1}]$	Test MAE $-R_{ECO}$ $[gCm^{-2}d^{-1}]$	Train Adj. R^2 $-R_{ECO}$	Test Adj. R^2 $-R_{ECO}$
US-NR1	0.19	0.11	0.95	0.98	0.33	0.18	0.91	0.98
CA-Oas	0.18	0.13	0.94	0.97	0.33	0.26	0.96	0.97
CA-Obs	0.12	0.09	0.95	0.96	0.29	0.25	0.96	0.97
US-SRM	0.22	0.17	0.92	0.94	0.24	0.19	0.80	0.87
US-Ton	0.22	0.17	0.92	0.94	0.43	0.36	0.76	0.82
US-Var	0.15	0.12	0.92	0.95	0.49	0.38	0.81	0.88
US-Whs	0.13	0.09	0.93	0.96	0.12	0.09	0.84	0.89
US-Wkg	0.19	0.15	0.87	0.91	0.18	0.15	0.85	0.91

3.4.2 Use Case 2: Ecoregion-Based, Data-Driven HPM Model for ET and R_{ECO} Estimation

While the effort and cost involved in establishing flux towers naturally limit the spatial coverage of obtained measurements, point scale measurements from one FLUXNET station provides representative information about ecosystem dynamics at other locations within the same ecoregion. In this section, we explored the use of a data-driven HPM trained with one FLUXNET station to estimate ET and R_{ECO} at other locations within the same ecoregion. To test this approach, we first trained HPM at a selected FLUXNET stations and validated these HPM models at other FLUXNET stations (ET and R_{ECO} data at testing sites were only used for comparison with HPM prediction) within the same ecoregion. Specifically, we developed HPM models at US-Ton, CA-Oas and US-Wkg, and provided ET and R_{ECO} estimations at US-Var, CA-Obs and US-Whs at three ecoregions, respectively.

Table 3.5 summarizes how we developed the data-driven HPM models for spatially distributed estimation of ET and R_{ECO} as well as the corresponding statistical summaries. The estimation led to an adjusted R^2 greater than 0.85 for CA-Obs and US-Whs and 0.70 for US-Var. Figure 3.7 and 3.8 present the time series of HPM-estimated ET and R_{ECO} compared to measurements from flux towers. The figures show that HPM captures the seasonal and longer-term dynamics of ET and R_{ECO} well, as indicated by the high adjusted R^2. However, we observed an increased error in HPM-based estimations compared to measurements during peak growing seasons (e.g., a 0.5 mm discrepancy in June mean ET). Higher prediction accuracy for the two ecoregions presented by US-Whs and CA-Obs are observed compared to US-Ton, which indicates other attributes are necessary to improve prediction accuracy, especially for sites limited by moisture conditions. For example, ET is usually constrained by moisture condition during peak growing season. Other attributes such as soil moisture can be very useful for improving the prediction accuracy. Although the prediction accuracy is not as high as Use Case 1 (Section 4.1), this use case demonstrates that HPM can learn the complicated relationships between responses and features successfully, and that a local data-driven HPM can be used to fuse with data from other subsites for long-term estimation of ET and R_{ECO} within the same ecoregions.

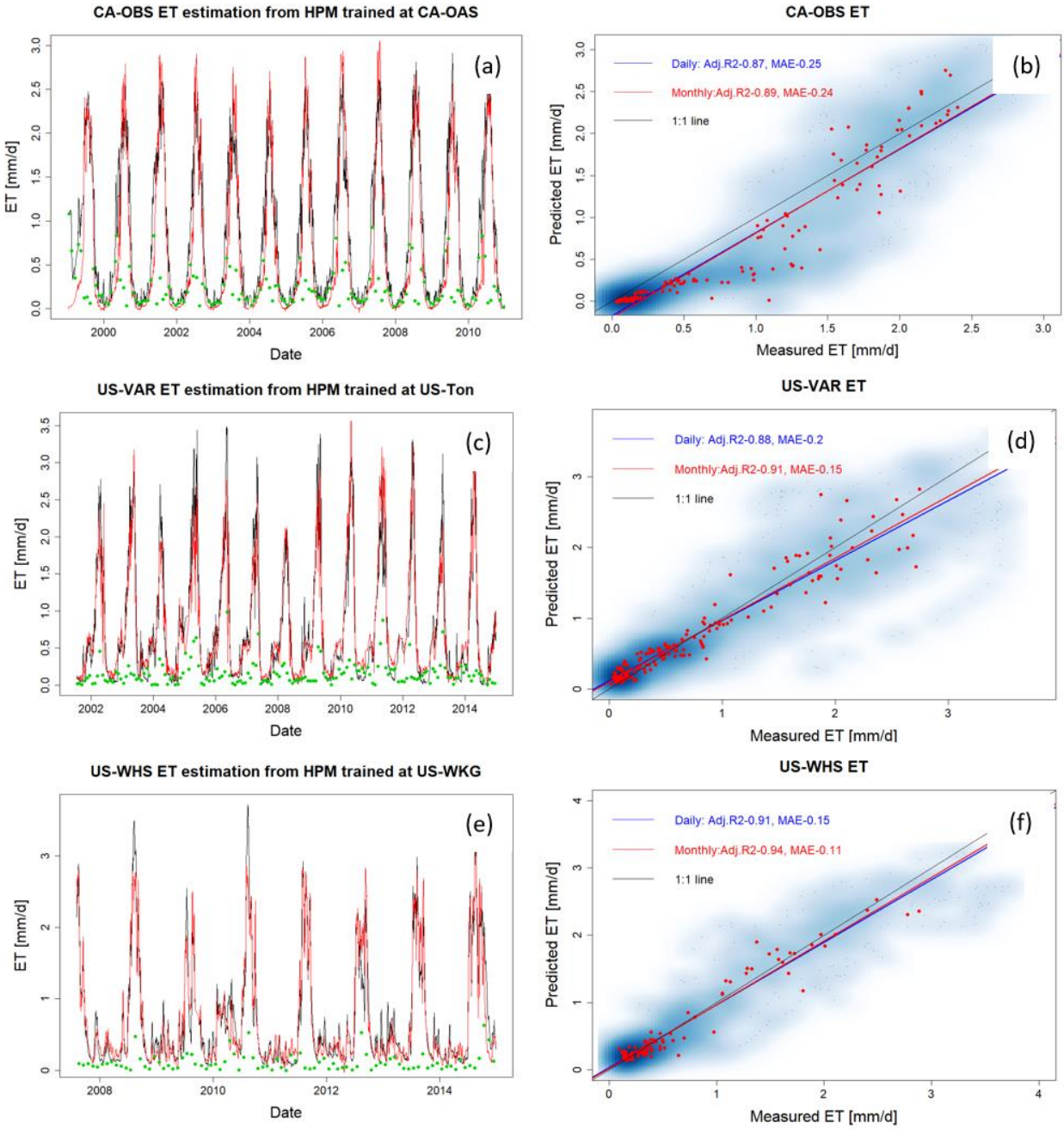

Figure 3.7 ET estimation at CA-Oas (a), US-Var (c), and US-Whs (e) with HPM trained at US-Ton, US-Wkg, and CA-Oas, respectively. Red and black lines represent HPM estimation and real measurements, with green points denoting the monthly mean difference between HPM estimationss and measurements. Panels (b), (d), and (f) show the scatter plots of daily (blue) and monthly (red) ET at these three sites. Darker blue clouds represent greater density of data points.

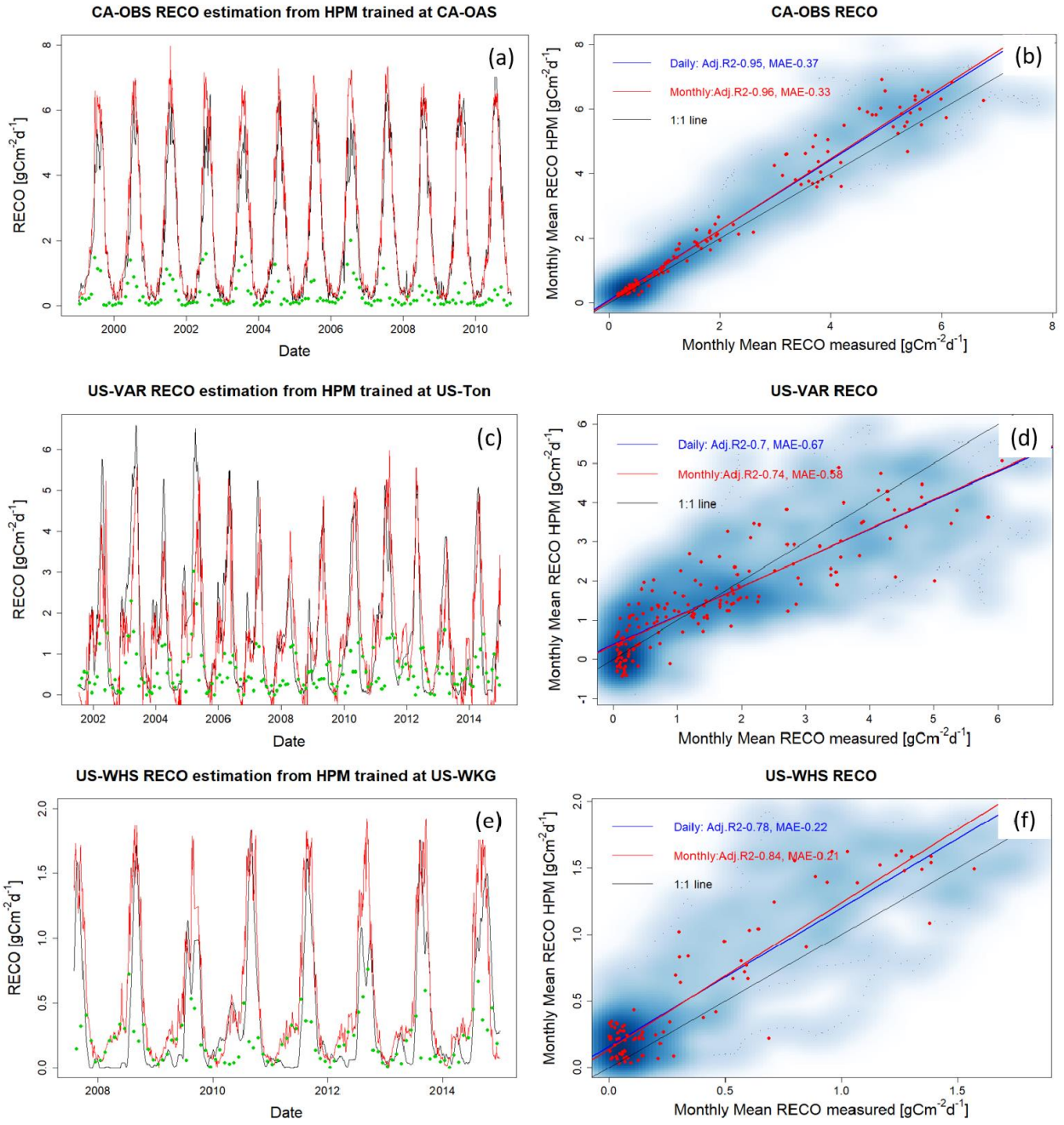

Figure 3. 8 R_{ECO} estimation at CA-Oas (a), US-Var (c), and US-Whs (e) with HPM trained at US-Ton, US-Wkg, and CA-Oas, respectively. Red and black lines represent HPM estimations and real measurements; green points denote the monthly mean difference between HPM estimation and measurements. Panels (b), (d), and (f) show the scatter plots of daily (blue) and monthly (red) R_{ECO} at these three sites. Darker blue clouds represent greater density of data points.

3.4.3 Use Case 3: Ecoregion-Based, Mechanistic HPM Estimation of ET

Mechanistic HPM, which is trained with ET estimates from 1-D physically-based-model simulations, provides an avenue for estimating ET in ecoregions where direct measurements from eddy covariance tower are not available. In order to test the effectiveness of the mechanistic

HPM, we focused on the three SNOTEL stations and US-NR1, which locates in the "Western Cordillera" ecoregion. Mechanistic HPM is coupled with CLM simulations at these sites (Tran et al., 2019). To ensure the CLM physically-based-model simulations can provide alternative datasets to develop mechanistic HPMs, we compared CLM estimation and direct measurements of ET at US-NR1 (Figure D.1). The consistent results between measured ET and CLM-estimated ET (adjusted $R^2 = 0.88$; $k = 0.95$) indicate independent CLM simulations can be effectively used to develop the mechanistic HPM.

We applied mechanistic HPM trained with 1-D CLM developed at ER-BT (Tran et al., 2019) to estimate ET at sites classified as part of the same ecoregion (i.e., ER-SP, ER-PK and US-NR1). We then compared ET estimation from HPM to independent CLM-based ET estimations at ER-SP and ER-PK and to direct measurements at US-NR1. Figure 3.9 shows a high consistency between HPM estimation and the validation data. For all scenarios, an adjusted R^2 of 0.8 or greater is observed (Table 3.5), which strongly indicates that mechanistic HPM can provide accurate ET estimation at sites of similar ecoregions. These results suggest the broad applicability of mechanistic HPM to estimate ET based on ecoregion characteristics. This approach is expected to be particularly useful for regions where flux towers are difficult to install or where measured fluxes are not representative of the landscape, such as in mountainous watersheds.

Table 3.6 Statistical summary of HPM estimation over space with FLUXNET sites and SNOTEL stations with CLM

Target Site	Training Site	Level II Ecoregion	ET MSE (monthly)$[mm/d]$	ET Adj. R^2	R_{ECO} MSE(monthly)$[gCm^{-2}d^{-1}]$	R_{ECO} Adj. R^2
CA-Obs	CA-Oas	Boreal Plain	0.39	0.88	0.36	0.97
US-Var	US-Ton	Mediterrean California	0.34	0.70	0.67	0.70
US-Whs	US-Wkg	Western Serra Madre Pidemont	0.13	0.94	0.17	0.85
ER-SP	ER-BT	Western Cordillera	0.20	0.92	-	-
ER-PK	ER-BT	Western Cordillera	0.24	0.90	-	-
US-NR1	ER-BT	Western Cordillera	0.23	0.90		

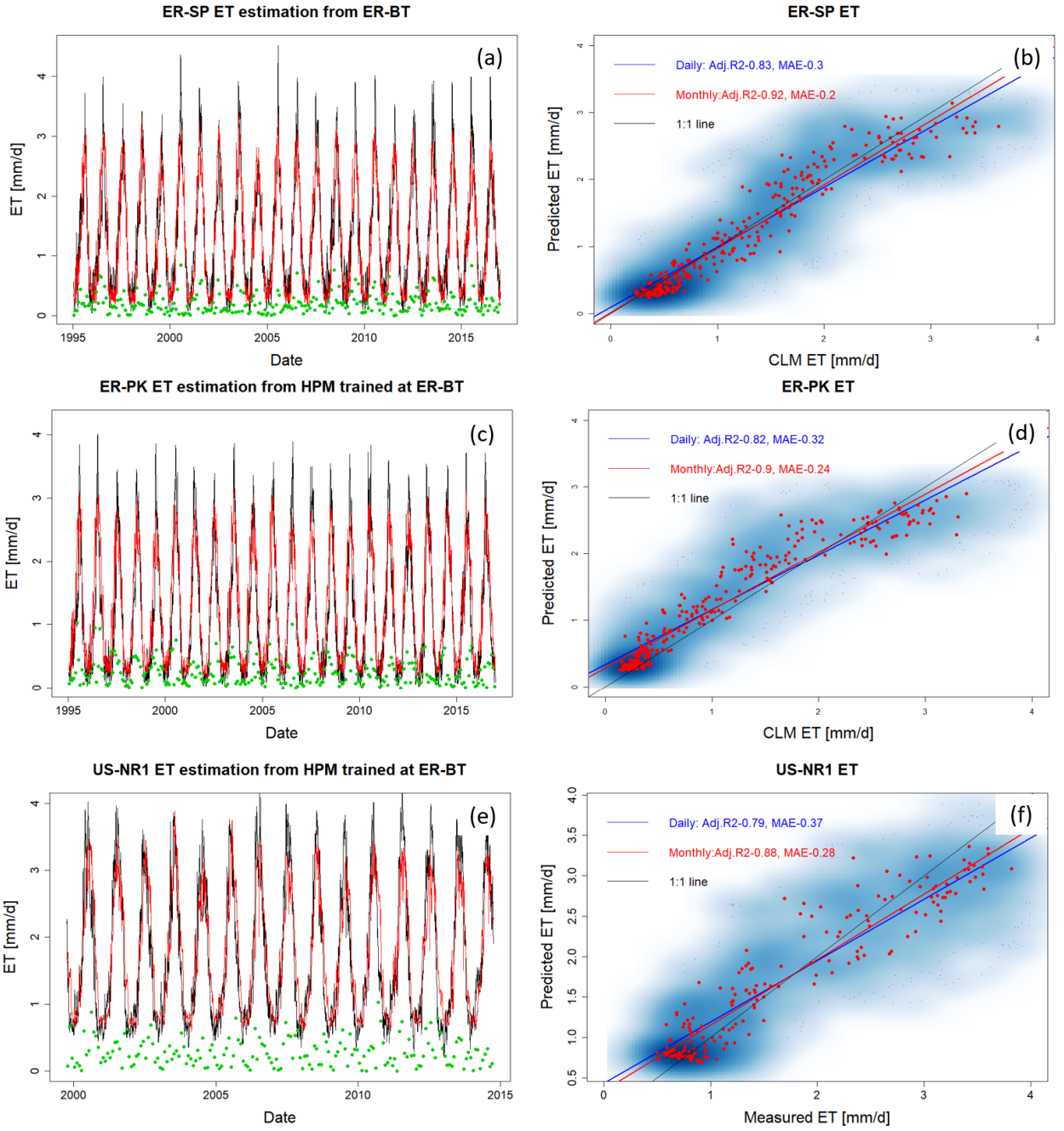

Figure 3.9 HPMs trained with CLM simulation at ER-BT are used to estimate ET at ER-SP, ER-PK, and US-NR1. Panels (a), (c), and (e) display HPM estimation of ET (red lines), as well as independent CLM estimation at ER-SP, ER-PK, and eddy covariance measurements at US-NR1 (black lines). Panels (b), (d), and (f) show the scatter plots of daily (blue) and monthly (red) ET at these three sites. Darker blue clouds represent greater density of data points.

3.4.4 Exploration of How ET and R_{ECO} Varies with Meteorological forcings and Vegetation Heterogeneity at the East River Watershed

ET and R_{ECO} estimated from the HPM model at the mountainous East River Watershed in CO enabled us to analyze how heterogeneity in vegetation and meteorological forcings influence

estimated ET and R_{ECO} dynamics, and to identify limitations in the developed approach for estimating ET and R_{ECO} across mountainous and heterogeneous watersheds.

NDVI time-series data provide high-resolution (30m) information about vegetation variability across the East River Watershed. The spatial distribution of vegetation cover presented in Figure 3.2 (from Falco et al. 2019) enables us to distinguish different patches of deciduous forests, evergreen forests, meadow grassland and riparian shrublands and retrieve corresponding NDVI time-series. Figure 3.10 shows Landsat-derived and reconstructed NDVI values for the four different vegetation types within the East River Watershed. Evergreen forests have an extended growing season compared to deciduous forests. However, peak NDVI is smaller in evergreen forests compared to deciduous forests. NDVI ranges from 0.2 to 0.6 for evergreen forests, whereas larger fluctuations in NDVI are observed for deciduous forests (-0.2 to 0.8). The NDVI values during the winter are likely sensing both snow and forest density, due to pixel spatial averaging from Landsat images. Similar to Qiao et al. (2016), we also found that the NDVI of deciduous forests exhibits a significant increase during the growing season, followed by a sharp decline (likely caused by defoliation), and that evergreen forests had a more stable NDVI.

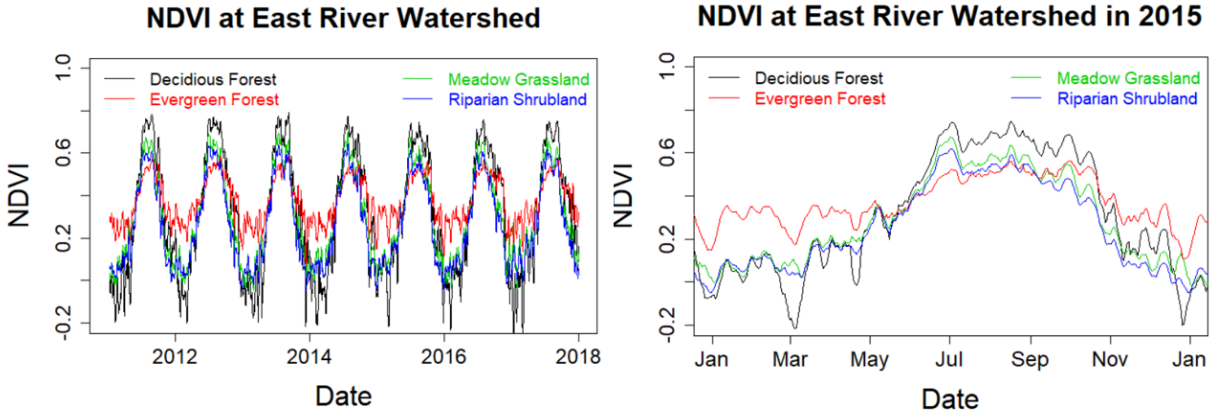

Figure 3. 10 Reconstructed NDVI time series at selected locations in the East River Watershed for 2011 to 2018 (panel a) and for 2015 (panel b, normal water year). Black, red, green, and blue lines represent the time series of NDVI for deciduous forests, meadow grasslands, evergreen forests and riparian shrubland, respectively.

HPM-estimated ET and R_{ECO} also show different dynamics in evergreen forests and deciduous forests. Figure 3.11a and 11b present the time series of estimated ET and R_{ECO} associated with deciduous forests, respectively. Figure 3.11c and d present the ET and R_{ECO} differences between deciduous forest sites and sites with other vegetation (e.g., evergreen forests shown in red). Before peak growing season, the ET of evergreen forests is about 10% greater than deciduous forests, whereas ET of deciduous forests during peak growing season is greater than evergreen forests. After growing season, the NDVI of deciduous forests is less than 0.2 (loss of leaves) compared to the NDVI of evergreen forests. Before peak growing season, R_{ECO} of evergreen forests is slightly greater than deciduous forests. During peak growing season, R_{ECO} of deciduous forests is around 17% greater than $R_{ECO}$of evergreen forests. Total annual ET between evergreen and deciduous forests is very close (DF1: 535 to 573 mm and EF1: 532 to 569 mm across 7 years in this study). Total annual R_{ECO} of evergreen forests is smaller than deciduous forests (DF1: 642 to 698 $gCm^{-2}d^{-1}$ and EF1: 592 to 639gCm^{-2}). The ET estimation at East

River Watershed is comparable to Mu et al. (2013), where ET is computed based upon the logic of the Penman-Monteith equation and MODIS remote sensing data. At the East River Watershed, data retrieved from Mu et al. (2013) indicate annual ET ranges from 554 to 585 mm at deciduous forests sites and 540 to 593 mm at evergreen forests sites. The R^2 between 8-day aggregated HPM-based ET estimation and data retrieved from Mu et al. (2013) achieves 0.65 (Figure B.1). Berryman et al. (2018) developed a random forest model to predict growing season soil respiration at subalpine forests in the Southern Rocky Mountain ecoregions. Their results suggest a consistent respiration rate from 2004 to 2006, with 150-day sums of $542.8, 544.3\ and\ 536.5\ gCm^{-2}$, respectively, with a mean measured growing season respiration across sites and years of 3.37 gCm^{-2}. HPM-based R_{ECO} estimation is also comparable to what Berryman et al. (2018) discovered, with growing season R_{ECO} ranging between 555 to 607 gCm^{-2} and mean growing season R_{ECO} ranging between $3.01\ to\ 3.30\ gCm^{-2}$. While we currently do not have a time-series measurement of ET and R_{ECO} at the East River Watershed for validation, our results are comparable to other studies that focus on sites within the same ecoregion (e.g., Berryman et al., 2018).

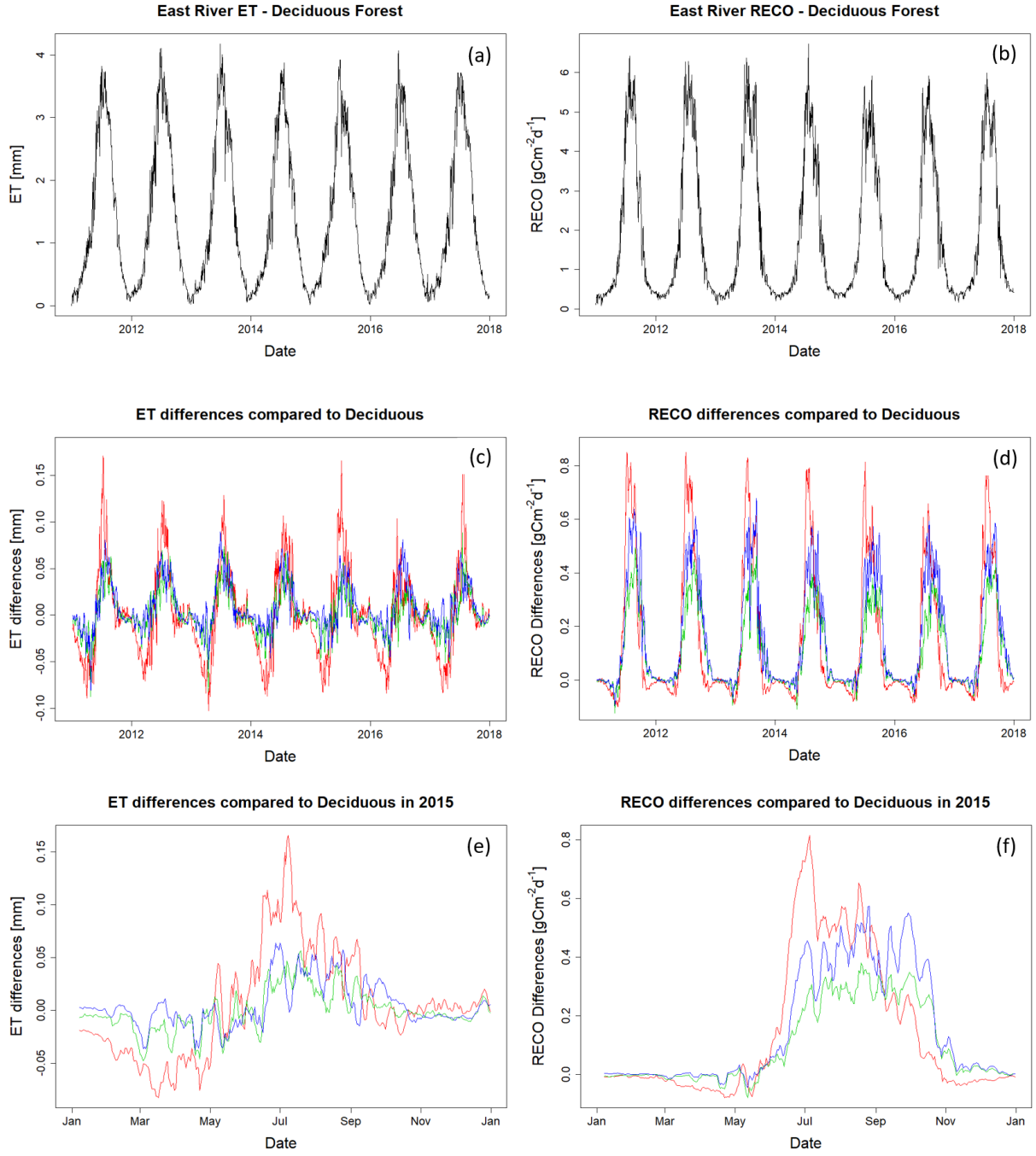

Figure 3.11 ET (a) and R_{ECO} (b) estimation for the deciduous forest site DF1 at the East River Watershed. Panels (c) and (d) show the differences in ET and R_{ECO} among various vegetation types and DF1. Red, green, and blue lines represent the differences in evergreen forest, meadow, and riparian shrubland compared to DF1. Panels (e) and (f) zoom into 2015 to better display seasonal variations.

ET and R_{ECO} estimation at the East River Watershed from the HPM model further enabled us to assess the impacts of small-scale (e.g., hillslope scale) heterogeneity in vegetation type on ET and R_{ECO} dynamics. Figure 3.12 shows the absolute value of monthly mean difference in ET

(Fig. 12a and Fig. 12b) and R_{ECO} (Fig. 12c and Fig. 12d) across SNOTEL stations (ER-BT, ER-SP and ER-PK) and within selected East River locations. A comparison of meteorological forcings data within selected East River locations and across SNOTEL stations are given in Figure C.1 and C.2. We observed 2.5 times greater differences in ET across SNOTEL stations compared to the sites within the East River watershed, whereas the differences in R_{ECO} across SNOTEL stations are at the same level compared to the sites within East River Watershed (around 0.8 gCm^{-2}). This result indicates small-scale meteorological forcings and vegetation heterogeneity are the major controls of differences in ET and R_{ECO} at the East River Watershed.

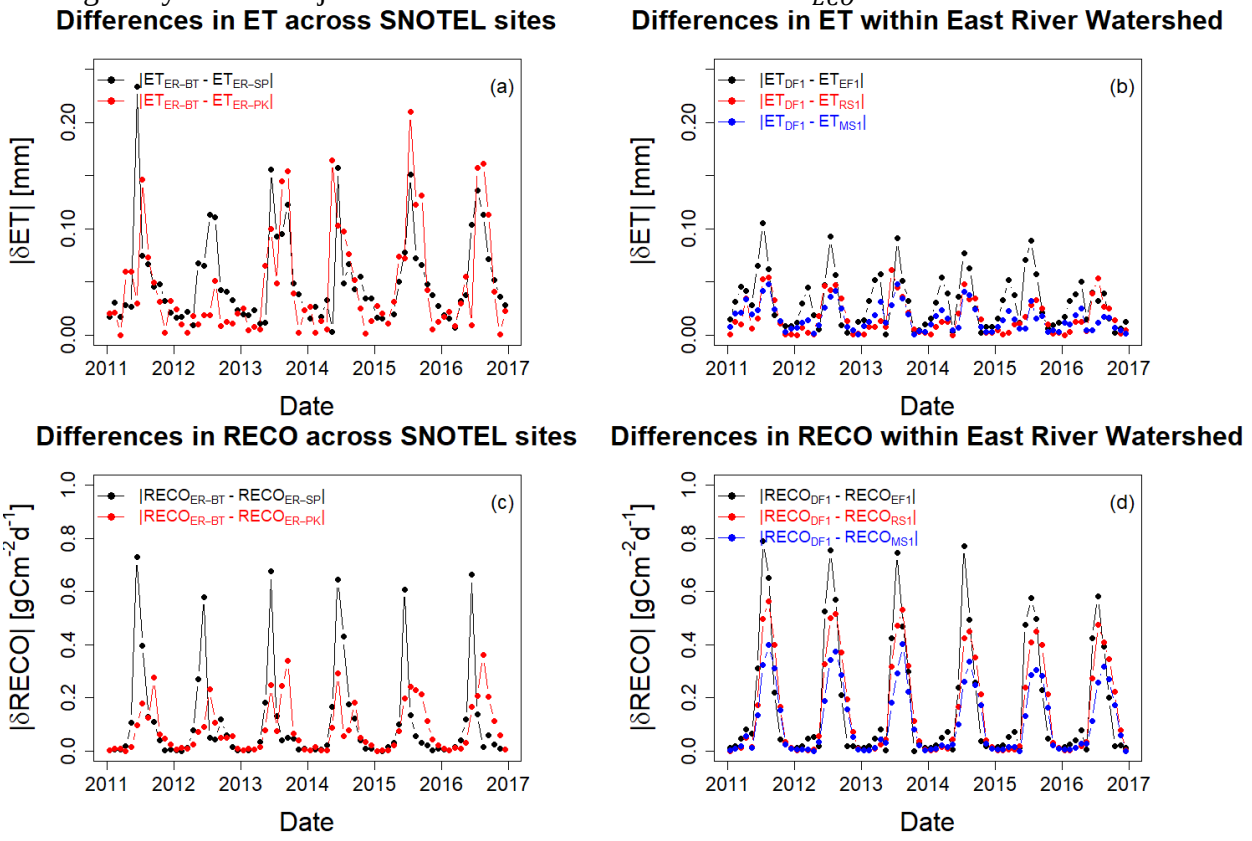

Figure 3.12 Absolute differences in monthly mean ET and R_{ECO} across SNOTEL stations and within East River Watershed. Panels (a) and (c) describe the absolute differences in monthly mean ET and R_{ECO} between ER-BT, ER-SP, and ER-PK. Panels (b) and (d) describe the absolute differences in monthly mean ET and R_{ECO} within East River Watershed between deciduous forest (DF1), evergreen forest (EF1), meadow (MS1), and riparian shrubland (RS1).

3.5. Discussion

Our study demonstrates that HPM provides reliable estimations of ET and R_{ECO} under various climate and vegetation conditions, including data-based HPMs that are trained with FLUXNET data and physical-model-based HPMs that are coupled with simulations results from mechanistic models (i.e., CLM in our case). With 70% of the data used for training (model development), ET and R_{ECO} estimation from HPM achieves an adjusted R^2 of 0.9 compared to eddy covariance measurements. With this high estimation accuracy, we demonstrated that this approach could be used for predicting ET and R_{ECO} over time. HPM is capable of "learning" the complex interactions among meteorological forcings, vegetation dynamics, and water and carbon

fluxes. The underlying relationships acquired by HPM can serve as a local ecohydrological model for long-term monitoring of ET and R_{ECO}, with the aid of remote sensing data, and can fill in gap data during occasional equipment failure.

HPM was also successful at estimating the spatial distribution of ET and R_{ECO} through exploiting an ecoregion concept. Using the representative FLUXNET sites in different ecoregions, HPM provided estimates of ET and R_{ECO} at locations using learned relationships from other sites having the same ecoregion classification. For conditions where no FLUXNET sites are within the same ecoregion, our study showed that physically-based models that can utilize weather forcings data can provide alternatives for developing mechanistic HPM to estimate ET and R_{ECO}. We found that HPM performance was more reliable when trained and applied at different watersheds in the same ecoregion. For example, HPM that only relies on energy-related parameters was able to successfully estimate ET and R_{ECO} at US-NR1 and CA-OAS, where radiation and temperature are key components that regulate ET and R_{ECO} dynamics. However, HPM with the same input features do not yield desired results at sites limited by water conditions (e.g., US-Ton and US-Var), due to lack of soil moisture data. This change indicates that parameter optimization and attributes selection may be needed for sites that are limited by moisture conditions, because important features can be subject to local conditions that potentially lower HPM performance.

We confirmed the important role of small-scale vegetation heterogeneity in modeling ET and R_{ECO} dynamics, which further enabled us to better understand ecosystem dynamics at the East River Watershed. As indicated from NDVI time series (Fig 10), evergreen forests have a longer growing season compared to deciduous forests; however, deciduous forests have greater peak NDVI values. Correspondingly, we also observed an earlier increase in ET and R_{ECO} for evergreen forests (before May), but larger ET and R_{ECO} for deciduous forests during peak growing season (around June and July). Annual ET between deciduous forests and evergreen forests are not statistically different, which is similar to (Berryman et al., 2018; Mu et al., 2013). Annual R_{ECO} differences between evergreen forests and deciduous forests are around $50\ gCm^{-2}$, which is comparable to Berryman et al. 2018). Similar dynamics were also observed at regions that are have different climate conditions. Through assessing the differential mechanisms of deciduous forests and evergreen forests at various sites under Mediterranean climates, Baldocchi et al. (2010) found that deciduous forests had a shorter growing season, but showed a greater capacity for assimilating carbon during the growing season. Evergreen forests, on the other hand, had an extended growing season but with a smaller capacity for gaining carbon. These results were identified through analyzing the relationships among leaf ages, leaf nitrogen level, leaf area, and water use efficiencies of these tree species at the selected Mediterranean climate sites. Older leaves tend to have smaller leaf nitrogen and stomata conductance, and thus evergreen forest ET and R_{ECO} are smaller during the peak growing season compared to deciduous forests, yet maintain a relatively high level before the peak growing season or during defoliation. Hu et al. (2010) analyzed flux data at US-NR1 to determine the relationships between growing season lengths and carbon sequestration, and found that extended growing season length resulted in less annual CO_2 uptake. They also found that the duration of growing seasons substantially decreases snow water storage, which significantly decreases forest carbon uptake. While we were not able in this study to assess the differential advatanges and physiological mechanisms among vegetation types, HPM-based estimation of ET and R_{ECO} presented similar dynamic trends to those found in Berryman et al. (2018); Hu et al. (2018); and Mu et al. (2013).

Microclimate and small-scale heterogeneity in meteorological forcings attributes control the magnitude and timing of ET and R_{ECO} dynamics. For example, other field observations along the Rocky Mountain ranges have shown that south-facing hillslopes have significantly earlier snowmelt compared to north-facing hillslopes (Kampf et al., 2015; Webb et al., 2018), which are hypothesized to result in significant differences in ET and R_{ECO} dynamics. As a result, estimation of small-scale ET and R_{ECO} dynamics requires high spatial resolution meteorological inputs, which is currently a challenge. We originally intended to investigate aspect impacts on ET and R_{ECO} dynamics at East River Watershed by selecting East River sites with different slope orientations. However, small-scale meteorological-forcings heterogeneity and microclimate were not available due to the relatively low spatial resolution of meteorological forcings inputs (DAYMET, 1 km scale). While DAYMET data suggest that differences in air temperature and solar radiation are very small for sites located at different portions of the watershed, the three weather stations at the site reveal that spatial heterogeneity in meteorological forcing attributes does exist, especially air temperature (Figure C.2). Even though the small-scale meteorological forcings heterogeneity is partly embedded in NDVI time series, the heterogeneity in ET and R_{ECO} estimated from HPM at the East River Watershed is potentially underestimated, due to the insufficient spatial resolution of meteorological inputs. In addition to limitations imposed from the spatial resolution, uncertainties in meteorological inputs can also result in large errors (i.e., >20% MAE) and reduce accuracy by 10-30% in ET and R_{ECO} estimations as suggested by Mu et al. (2013) and Zhang et al. (2019). Thus, there is still a significant need for high-spatial-resolution meteorological-forcing data products, such as data provided by the Surface Atmosphere Integrated Field Laboratory (SAIL) that can capture small-scale heterogeneity for implementing into HPM, which will then enable us to better assess the governing factors that regulate small-scale heterogeneity in ET and R_{ECO}.

In addition to the quality of meteorological data, HPM is also influenced by remote sensing inputs accuracy. Incorrectly calculated or pixel-averaged NDVI values from Landsat images can greatly alter HPM outputs for ET and R_{ECO}. Satellite images with different cloud cover have a slight influence over the NDVI values calculated, which do not represent real-time vegetation conditions. Algorithms used to reconstruct daily NDVI time series are also subject to uncertainties. However, with recent advances in remote sensing and satellite technologies (McCabe et al., 2017), the spatial and temporal resolution should greatly increase in the future (i.e., 3 m resolution and daily). These advances will lead to more accurate classification of vegetation types and NDVI calculations, which are expected to decrease uncertainty associated with flux estimation

Another source of uncertainty in HPM arises from the choice of hybrid approaches and any parameter uncertainties in mechanistic models. Since HPM relies on accurate ET and R_{ECO} inputs from flux towers or mechanistic models, any uncertainties in measuring or modeling ET and R_{ECO} will propagate to HPM. If HPM is developed with a mechanistic model that has such missing components, these biases will be passed on to HPM estimation of ET and R_{ECO}. Parameter and conceptual model uncertainties in mechanistic models also restrict HPM's ability to "learn" the ecosystem dynamics. In order to reduce potential biasedness, we trained data-based HPM and physical-model-based HPM upon long time series (e.g., > 5 years) with quality assessed data or simulation results, which also enables HPM to better memorize long time dependencies of ecosystem dynamics. Though the quantification of uncertainties remains

challenging, efforts have been made to lower these uncertainties using the technical advances described here.

3.6. Conclusion

In this study, we developed and tested a Hybrid Predictive Modeling (HPM) approach for ET and R_{ECO} estimation, with a focus on mountainous watersheds. We developed individual HPM models at various FLUXNET sites and at sites where data can support the proper development of a mechanistic model (e.g., CLM). These models were validated against eddy covariance measurements and CLM outputs. We further used these models for ET and R_{ECO} estimation at watersheds within the same ecoregion to test HPM's capability of providing estimation over space, where only meteorological forcings data and remote sensing data were available. Lastly, we applied the HPM to provide long-term estimation of ET and R_{ECO} and test the sensitivity of HPM to various vegetation types at various sites within the East River Watershed.

Given the promising results of HPM, this work offers an avenue for estimating ET and R_{ECO} using easy-to-acquire or commonly available datasets. This study also suggests that the spatial heterogeneity of meteorological forcings and vegetation dynamics have significant impacts on ET and R_{ECO} dynamics, which may be currently underestimated due to typically coarse spatial resolution of data inputs. Parameters related to energy and soil moisture conditions can be implemented into HPM to increase HPM's accuracy, especially for sites limited by soil moisture conditions. Lastly, it should be pointed out that HPM is not restricted to estimation of ET and R_{ECO} only. We focused here on developing HPM for ET and R_{ECO}, but HPM also has great potential for estimating other parameters important for water and carbon cycles. Indeed, other attributes, such as GPP and sensible heat flux, might also be accurately captured and represented with HPM, given the right choice of features.

Chapter 4

Defining Temporal Regimes for Assessing Intra-annual Variability of Evapotranspiration in Central Rocky Mountain Watersheds

4.1 Introduction

Mountainous watersheds provide more than 60% of the water resources to the world and are thus recognized as "Water Towers" of earth that provide significant economic and societal benefits (Immerzeel et al., 2019; Viviroli et al., 2007). Central Rocky Mountains and the Colorado River Basins provide vital source of water for agricultural and urban areas in western North America. Annual contribution of the Colorado River to the combined Gross State Product in the Colorado River Basin region is approximately one twelfth of total U.S. gross domestic product in fiscal year 2012 (James et al., 2014) with over 16 million public and private sector jobs in the Colorado River Basin Region relying on the availability of Colorado River Water. Water and energy resources availability of the Colorado River thus have a crucial impact on the socioeconomic development of the region. However, changes in meteorological forcing, such as increases and decreases in temperature and precipitation, can lead to uncertain responses in watershed dynamics and increase the uncertainties in water and energy resources management (Immerzeel et al., 2019). Studies have shown that mountainous watersheds' responses to climate change have been greatly altered in the past few decades, including streamflow responses (Godsey et al., 2014); montane biodiversity (Voepel et al., 2011); plant phenology (Jonas et al., 2008); occurrences of droughts (Sloat et al., 2015); soil moisture dynamics (Aulenbach & Peters, 2018); and evapotranspiration (ET) and ecosystem respiration (Jung et al., 2017; Nelson et al., 2018). Occurrences of extreme weather, fire, floods and other perturbations are significantly reshaping complex interactions within mountainous watersheds, leading to challenges in the development of optimized management strategies to meet the growing demand of clean water, food and energy (Carpenter et al., 2015). Thus, quantifying the interactions among changes in

hydroclimate and watershed processes is extremely important for understanding mountainous watersheds' evolution under climate change as needed to improve management strategies.

Interactions among meteorological forcing and watershed processes are complex. Changes in temperature, radiation and precipitation patterns can greatly alter growing season length, the timing of snowmelt, defoliation and plant phenology and crucially influence the hydrological cycle, including runoff, discharge and ET. Recent global climate models and studies have predicted that the increase in spring temperatures in the Rocky Mountains may occur weeks earlier than today by the end of this century, which may result in significant earlier snowmelt and snowmelt-driven runoff (Blankinship, 2014; Rauscher et al., 2008; Stocker et al., 2013). Changes in the timing of snowmelt further alters the intra-annual variability of other numerous processes. Shorter growing season with decreased plant productivity can occur due to decreased water availability from earlier snowmelt and warmer summer temperatures (Ernakovich et al., 2014). Wieder et al. (2017) discovered earlier snowmelt and warmer summertime temperatures can cause significant divergent plant responses across landscape. Earlier snowmelt also increases the probability of occurrences of fore-summer (May-June) drought (Sloat et al., 2015). Working at the East River of Colorado, they showed that the severity of drought conditions significantly decreased peak and cumulative net ecosystem productivity (NEP) and ET, especially during soil moisture limiting conditions. In the same watershed, Wainwright et al. (2020) used satellite data to explore the spatial heterogeneity of foresummer drought sensitivity of plant productivity. Their study suggested that peak plant productivity (expressed by remote-sensed vegetation indices) was highly correlated with the timing of snowmelt and foresummer temperature. Weiss et al. (2009) showed that occurrences of foresummer drought can significantly reduce ET due to limited soil moisture in the subsurface. The duration of foresummer drought in the Rocky Mountains is not only influenced by the timing of snowmelt and warmer temperature, but also by monsoon timing and magnitude. These studies focus on different aspects of changes in hydroclimate, and strongly suggest the necessity to describe intra-annual variability of watershed processes qualitatively and quantitatively.

Evapotranspiration, as the important component of water and energy cycle, is also largely influenced by atmospheric and soil conditions. Quantifying the inter-annual variability of ET dynamics improves our understanding of watershed responses and increase our capability for water and energy resources management. In the North American monsoon region, Bohn & Vivoni. (2016) suggested a strong correlation between ET and current monsoon precipitation, whereas correlation between ET and precipitation from prior seasons were not statistically significant. Working in the Gunnison River Basin of Colorado, Condon & Maxwell, (2019) simulated how ET and streamflow respond to large-scale groundwater depletion under synthetic climate change scenarios. Their study demonstrated a significant decline of ET in water-limited periods and shallow groundwater regions. Foster et al., (2016) used an integrated modeling approach to isolate the impacts of climate change on Rocky Mountain hydrology. Their study suggested that phase shifts in precipitation inputs from snow to rain and changes in energy-driven evaporative losses were the most influential control on watershed hydrology, especially streamflow discharge and ET. Fatichi & Ivanov (2014) investigated how fluctuations of annual precipitation influenced ecohydrological dynamics (including ET and plant productivity) through imposing four scenarios characterized by different interannual variabilities of precipitation. Their findings suggested a relative insensitivity of the interannual ET and vegetation productivity to annual climatic fluctuations except for water-limited environment. Their study also indicated that

fluctuations of inter-annual variability of ET and plant productivity can be better explained by certain combination of meteorological conditions taking place within the year rather than annual conditions. Thus in addition to capturing the inter-annual variability of ET, there's a strong need to incorporate sub-annual dynamics and develop approaches that could quantitatively analyze the intra-annual variability of ET

Recent methods that focused on quantifying intra-annual variability of ET dynamics leveraged the Budyko framework and its extensions that distinguish energy-limiting versus water-limiting conditions for ET dynamics (Budyko, 1961; Zhang et al., 2008). Zeng & Cai, (2015) decomposed the variability of ET into covariance from precipitation, potential evapotranspiration (PET) and storage factors and suggested that: precipitation variability mostly influenced ET variance under hot-dry climates; variance of PET was the limiting factor for ET variance under cold-wet climates; and both precipitation and PET variance were important under moderate climate. Zeng & Cai. (2016) further emphasized the importance of terrestrial storage for dampening ET variance in arid climates but strengthening ET variance in humid climates. Similarly, Zhang et al. (2016) examined the contributions of precipitation, reference ET and total water storage change to ET and streamflow variability under different climate conditions through Budyko-based variance decomposition framework. However, methods based upon the Budyko hypothesis are restricted to the two limiting conditions (i.e., soil moisture and energy inputs), and do not systematically consider other processes, including snow, drought, growing season and monsoon. For example, in mountainous watersheds such as those in the Rocky Mountains, the effects of earlier snowmelt and the resulting fore-summer drought on ET can possibly be compensated by an earlier monsoon leading to small or no changes in annual ET. Alternatively, drought conditions can be intensified by late arriving monsoons, resulting in severer vegetation loss and decrease in ET and plant productivity. Transitions and phase shifts among these processes, such as timing of snowmelt, occurrences of drought and monsoon seasons, trigger significant intra-annual variability of ET. These disproportionate contributions caused by these transitions and phase shifts cannot be quantified without identifying the corresponding sub-annual processes.

In this chapter, we proposed the concept of temporal regimes to delineate the transition among various hydroclimate processes and to better assess the intra-annual variability of ET dynamics. Each temporal regime was determined based on the unique combination of statistical characteristics (e.g., amplitude and variance) of meteorological attributes, including air temperature radiation and precipitation inputs. Temporal regimes characterize the distinct rate, duration and process of ET dynamics. In each temporal regime, we expect to observe different ET behavior compared to other temporal regimes, however with relatively constant ET rate within the same temporal regime across different years and locations. The duration of temporal regime thus becomes a key parameter for assessing the intra-annual variability of ET as well as a pivotal component that controls the inter-annual variability of ET.

4.2 Study Sites

In this chapter, we focus on six sites along the Rocky Mountains, including sites from the FLUXNET network (https://fluxnet.fluxdata.org/) and SNOTEL sites (https://www.wcc.nrcs.usda.gov/snow/). Three FLUXNET sites are considered in this chapter, including the Niwot Ridge site (US-NR1, Monson et al., 2002), the Glacier Lakes Ecosystem Experiments Sites (US-GLE, Frank et al., 2014) and the Valles Caldera Conifer site (US-VCM, Litvak et al., 2016). US-NR1 (40.0329, -105.5464) is located in a subalpine forest ecosystem at

3050m elevation with a subarctic climate and evergreen needleleaf forests as the dominant vegetation. US-GLE (41.36653, -106.2399) is located in the Snowy Range of Wyoming at an elevation of 3197m. US-GLE is characterized as a high elevation wilderness-like site with an alpine and subalpine aquatic and terrestrial ecosystem and evergreen needleleaf forests is the dominant vegetation at US-GLE. US-VCM (35.888447, -106.532114) is located in the Jemez River basin in north-central New Mexico at 3030m elevation. The dominant vegetation for US-VCM is also evergreen needleleaf. US-VCM experienced a stand-replacing wildfire in May 2013, which resulted in discontinuous functionality of flux tower until 2014. We will discuss the data processing procedure at US-VCM in the following sections.

The three SNOTEL sites considered in this chapter include Butte (ER-BT, id: 380), Porphyry Creek (ER-PK, id: 701) and Schofield Pass (ER-SP, 737). These three sites are part of the East River Watershed, which is located within the Elk Range of the central Rocky Mountains in the state of Colorado and is a testbed for the US Department of Energy Watershed Function Scientific Focus Area Project (Hubbard et al., 2018). Montane to alpine ecosystems with an elevation from 2500m to 4000m are present within this watershed, which provides life support for mixed vegetation in this region. Figure 1 displays the geographical locations of the three FLUXNET sites and three SNOTEL sites considered in this chapter.

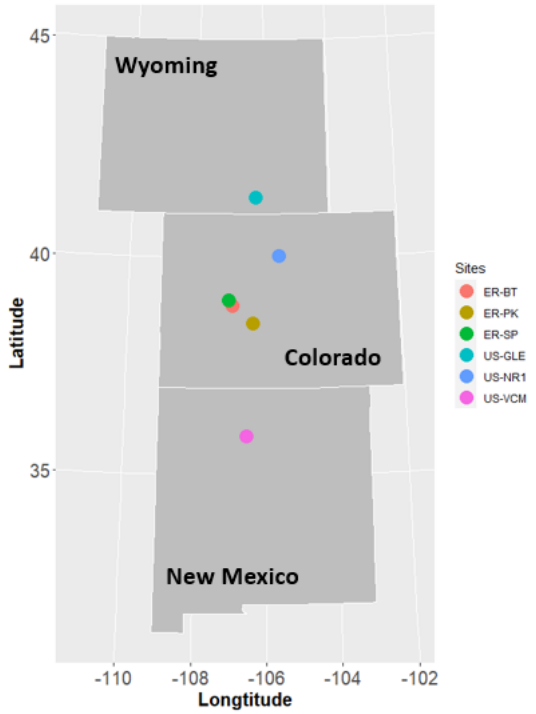

Figure 4.1 Geographical locations of the six sites selected in this chapter

4.3 Data Acquisition

4.3.1 Climate forcing data

At the three FLUXNET sites, eddy covariance towers have been installed and maintained to provide half-hourly direct measurements of climate forcing data, including air and soil temperature, precipitation, and solar radiation. As we mainly focused on daily temporal scales in

this chapter, we aggregated half-hourly climate forcing data into daily scales. As ecosystem dynamics in these watersheds are mainly controlled by snow dynamics, it is necessary to incorporate snow depth or snow water equivalent time series. Thus we also obtained snow data from Niwot (SNOTEL id: 663) for US-NR1, Brooklyn Lake (SNOTEL id: 367) for US-GLE, and Quemazon (SNOTEL id: 708) for US-VCM. At the three SNOTEL sites in the East River Watershed, quality assessed climate forcing data were obtained from https://wcc.sc.egov.usda.gov/, including air and soil temperature, precipitation, snow water equivalent and snow depth. In addition, we followed approaches proposed in Oyler et al. (2015) to filter potential systematic artifacts in air temperature data. Solar radiation data is not available at these three SNOTEL sites, and thus we integrated incident solar radiation from the DAYMET database (Thornton et al., 2017). For certain conditions such as data gap and unreasonable data due to power outages or sensor malfunction, DAYMET climate forcing data were also used to append the time series of climate forcing at these sites. Snow water equivalent and snow depths data are available at the SNOTEL sites, however are not measured at FLUXNET sites. Thus in this study, we did not directly integrate snow data into the model. Table 4.1 provides a statistical summary of climate forcing attributes at these six sites.

Table 4.1 Summary of six sites selected in this chapter.

Site ID	Site Name	Latitude	Longitude	Elevation (m)	Air Temperature ($^\circ C$)	Rain Precipitation (mm)	Snow Precipitation (mm)	Climate Koeppen
US-NR1	Niwot Ridge	40.0309	-105.5464	3050	2.43	377	632	Dfc
US-GLE	Glees	41.36653	-106.2399	3197	0.80	234	855	Dfc
US-VCM	Valles Caldera Mixed Conifer	35.88845	-106.53211	3030	4.70	397	284	Dfb
ER-BT	Butte	38.894	-106.945	3096	2.38	342	564	Dfc
ER-SP	Schofield Pass	39.02	-107.05	3261	1.97	392	784	Dfc
ER-PK	Porphyry Creek	38.49	-106.34	3280	2.46	267	368	Dfc

4.3.2 ET data

At the FLUXNET sites, ET data were calculated from the latent heat fluxes measured from eddy covariance towers. We followed approaches developed in Rungee et al. (2019) to further process unreasonable ET data and fill the gaps in ET measurements. Independent Community Land Models (CLM) were developed for both FLUXNET sites and SNOTEL sites at the East River Watershed (Tran et al., 2019) using the augmented climate forcing time series documented in the previous section. For certain periods of time when it is not feasible to use approaches in Rungee et al. (2019) to gap fill ET data, we used ET estimation from the developed CLM. We also applied CLM ET estimation to append data till 2016 so that we obtained 10 years of ET augmented data to analyze long-term dynamics of ET under climate change. Specifically, at US-VCM, we used the ET estimation from CLM to replace the post-fire dynamics after May 2013. It is noted that the time series after 2013 do not consider the effects caused by fire at US-VCM, and our approach does not consider any factors related with fire. A comparison between ET estimated from CLM and direct measurements from the three FLUXNET sites are provided in the supplementary materials (Figure D.1, R^2>0.8, $k > 0.94, p < 2.2e-10, MAE < 0.25mm$ for all three sites), which enables us to use CLM ET estimation to integrate with direct flux measurements. As no flux tower data is available for the three SNOTEL sites, we obtained ET estimation from Tran et al. (2019) for ER-BT, ER-SP and ER-PK. Despite the high estimation accuracy of CLM models, augmented ET data for FLUXNET sites and ET estimation from SNOTEL sites are subjective to any conceptual model and parameter uncertainties in CLM. We

should point out the use of CLM estimation does not restrict the applicability of our approaches. If flux tower measurements become available at SNOTEL sites, these data can be easily integrated into our approach.

4.4 Framework of Temporal Regimes

In this section, we will provide a brief overview of the statistical methods applied in this study. Hypothesis tests and analysis of variance (ANOVA) were used to estimate the heterogeneity of meteorological forcing attributes and ET in space and time. Hidden Markov Model (HMM) was used to statistically characterize temporal regimes that govern ET dynamics. Regime transitions in meteorological forcing were determined, and further used to determine the intra-annual variability of ET dynamics. Based on the results of temporal regimes, we calculated the within-regime cumulative ET, which is the sum of total ET for each temporal regime to determine the contribution of each temporal regime and dominant seasonal event to the annual ET. Our proposed method provides a qualitative and quantitative approach to analyze inter- and intra-annual variability of ET dynamics under climate change.

4.4.1 Analysis of Variance (ANOVA) and Tukey's test

ANOVA is a statistical method used to test the differences between two or more means. In this study, we applied ANOVA to test the null hypothesis that the mean values of meteorological forcing attributes and ET from the six sites do not vary significantly. Rejecting the null hypothesis indicates that the differences in hydroclimate attributes and ET observed across different sites are unlikely caused by random chance, indicating heterogeneity in meteorological forcing and ET data over space and time. A test statistic (e.g., F-statistics) is calculated and used to calculate a p-value, which is compared to a preset significance level (0.05 in this study). When the p-value is smaller than the significance level, the null hypothesis is rejected, which indicates significant spatial heterogeneity or temporal variability is present in at least one member of the group compared to the rest. ANOVA is not capable of identifying which location or which year is statistically different from the other locations or years when the null hypothesis is rejected. Hence, Tukey's test (Tukey, 1949) is also used in conjunction with ANOVA to further determine pairwise differences across the six sites. It compares all possible pairs of means, and is based on a studentized range distribution to determine whether or not to reject the null hypothesis. Failing to reject the null hypothesis indicates the mean of the two pairs are not statistically significantly different from each other. We also applied linear regression to determine the trends of meteorological forcing and ET over time under climate change. The slope coefficient represents rate of change in attributes over years. A goodness of fit test is usually performed together with linear regression to determine if such slope coefficient is statistically significant, which indicates if the trend of meteorological forcing or ET dynamics is statistically significant under climate change.

4.4.2 Hidden Markov Model (HMM) for temporal regime determination

HMM is a statistical model in which the system being modeled is assumed to be a Markov process with unobserved (i.e., hidden) states. Among many other studies, HMM has been used to characterize mechanistic reaction network of uranium transport in a contaminated aquifer (Chen et al., 2013), reconstruct streamflow (Bracken et al., 2014, 2016), and predict spatiotemporal variability in precipitation (Foufoula‐Georgiou & Lettenmaier, 1987; Zucchini & Guttorp, 1991). In this study, six temporal regimes (R0 to R5) were determined through identifying the hidden states and transitions through HMM with a year specific drought regime. Temporal changes in meteorological forcing attributes lead to transitions among different temporal regimes

related with hydroclimate processes (e.g., snowmelt season, growing season, and monsoon season). Each temporal regime will have distinguishable statistical characteristics of meteorological forcing attributes and ET compared to other temporal regimes. The use of HMM enables us to statistically characterize the boundaries and transitions among temporal regimes and thus assess the intra-annual variability of ET dynamics.

We notations employed in Chen et al. (2013) and Zucchini & MacDonald. (2009) to present a brief summary of HMM. For observed time series of hydroclimate attributes ($X_t, t = 1, 2, \dots, T$, i.e., air temperature, precipitation, and radiation), we defined a temporal regime variable $R_t, t = 1, 2, \dots, T$, where R_t takes values from $1, 2, \dots, m$, which represents m unique temporal regimes. The emission (output) probabilities are used to relate "temporal regimes" with the observed measurements (i.e., meteorological forcing attributes), and are modeled by state dependent probability distributions:

$$p_i(x) = P(X_t = x | R_t = i) \tag{4.1}$$

First order Markov process has been assumed to represent the time series behavior of measurements and temporal regimes, which are presented as follows.

$$P(R_t | R_1, R_2, \dots, R_{t-1}) = P(R_t | R_{t-1}), t = 2, 3, \dots, T \tag{4.2}$$

$$P(X_t | X_1, X_2, \dots, X_{t-1}, R_1, R_2, \dots, R_t) = P(X_t | R_t), t = 2, 3, \dots, T \tag{4.3}$$

Transitional probability metrics denote the probabilities of transition between temporal regime i to temporal regime j, and are expressed as:

$$\gamma_{jk} = P(R_{i+1} = k | R_i = j) \tag{4.4}$$

where R denotes a temporal regime determined from HMM. If $k = j$, then no transition of the temporal regimes occurs in the time domain. In order to estimate the unknown parameters, the likelihood function needs to be derived, which is the joint conditional probability distribution of all the data given unknown parameters with the initial probability of unknown temporal regime. The unknown parameters (including temporal regimes) can be determined using the Expectation-Maximization algorithm. More details about deriving the likelihood function and the E-M algorithm can be found in Zucchini & Guttorp (1991) and Dempster et al. (1977). We used the package "depmixS4" in R developed by Visser & Speekenbrink (2010) for implementation.

In this chapter, we used air temperature, soil temperature and radiation as inputs to HMM. In addition, a categorical variable (sn) that represents hydrological dynamics is also included as an input. sn is determined based on the time series of air and soil temperature as well as precipitation data. It provides a proxy for peak snow day, bareground day, effective monsoon day, which represents the day with maximum snow depth, first day of snow disappearance and first day that have monsoon precipitation greater than 10 mm, respectively. If snow data becomes available, snow accumulation, melting and no snow can be directly determined with snow water equivalent and depth data. sn is derived as follows,

$$sn = \begin{cases} 0; if\ air\ temperature < 0℃ \\ 1;\ \ if\ air\ temperature > 0℃\ and\ soil\ temperature < 0℃ \\ 2; if\ temperatures > 0℃ \\ 3; if\ temperatures\ and\ precipitation < 10mm \\ 4; if\ monsoon\ precipitation > 10mm \end{cases} \tag{4.5}$$

We assumed a Gaussian distribution for the emission probability $p_i(x) = N(\mu_i, \sigma_i^2)$ for air temperature, soil temperature and radiation inputs. Other state probability distributions for the emission probability can be applied based on other conditions with domain knowledge. For

example, a Gamma state dependent probability distributions have been widely used for precipitation regime determination (Bracken et al., 2014, 2016). Figure 4.2 displays hypothesized seasonal events, where we generally characterize any year into regimes of snow accumulation, snowmelt, growing season, monsoon season and defoliation season. For given combination of meteorological conditions such as significantly earlier snowmelt (e.g., Year 2012), it is likely that the watershed encounters a foresummer drought during the growing season, and hence a potential drought regime ($R_?$) is added in figure 2 as well. Temporal boundaries of these temporal regimes are selected based upon the mode of 1000-Hidden Markov Model simulations with the optimal information criterion (Akaike, 1974; Schwarz, 1978).

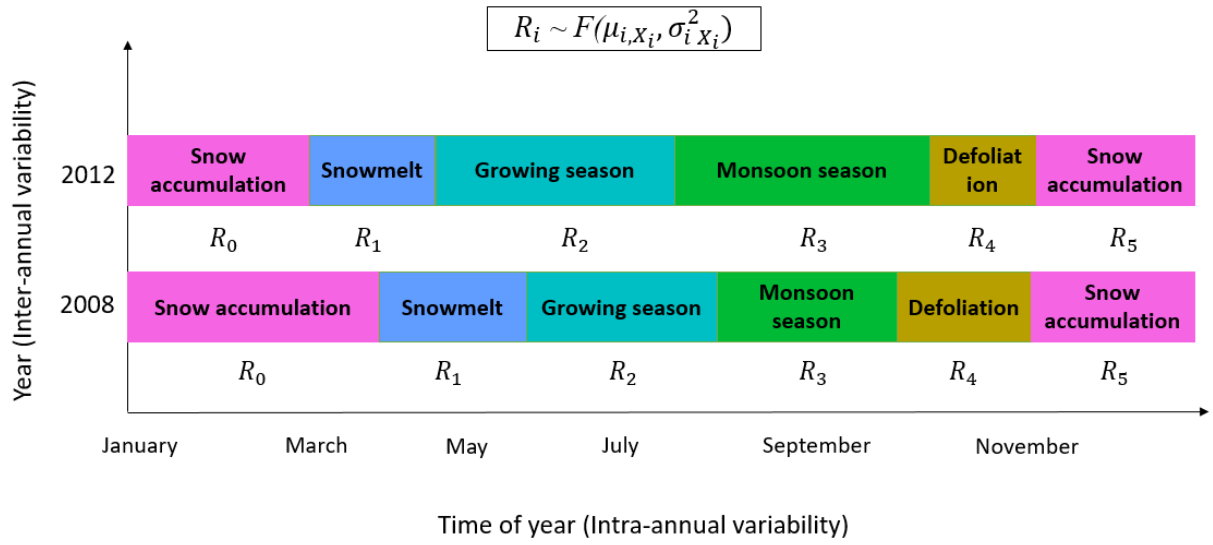

Figure 4.2 Illustration of potential temporal regimes (R_i) within a year. X_i represents the data used to determine temporal regimes and follow a statistical distribution denoted by $F(\mu_i, \sigma_i^2)$. μ_i and σ_i^2 are the mean and variance of X_i under specific temporal regimes, respectively

With temporal regimes being determined from Hidden Markov Model, we defined within-regime cumulative ET that represents the contribution of ET from each individual temporal regime to annual cumulative ET as indicated in equation (6), where ET_{R_i} is the mean ET (mm/d) and $duration_{R_i}$ represents the duration of temporal regime R_i.

$$Within\ R_i\ ET = ET_{R_i} * duration_{R_i} \tag{4.6}$$

$$Annual\ ET \cong \sum_{i=0}^{i=5} within\ R_i\ cumulative\ ET\ = \sum_{i=0}^{i=5} ET_{R_i} * duration_{R_i} \tag{4.7}$$

4.5 Results and Discussion

In this section, we first presented the spatial heterogeneity and temporal variability observed in meteorological forcing attributes and ET data across the sites selected in this study (section 4.5.1). Then we focused on the characteristics of each temporal regime (section 4.5.2) and demonstrated the underlying dominant processes and assessed the spatiotemporal variability in

temporal regimes (section 4.5.3). In section 4.5.4, we analyzed the intra-annual variability of ET through within-regime cumulative ET based upon temporal regimes. Section 4.5.5 explained the linkage between temporal regimes and watershed dynamics observed in the physical environment. In the last section, we used year of 2008 and 2012 as examples to explain how determination of temporal regimes can help us better understand the inter-annual variability of ET.

4.5.1 Nonlinear interactions between meteorological forcing and ET dynamics

The six sites selected in this study covers a wide range of annual mean air temperature, annual rain precipitation, annual snow precipitation, annual mean solar radiation, annual ET, and annual P-ET (Figure 4.3). We observe close to 5℃ difference in the annual mean temperature between US-VCM and US-GLE, 500 mm snow precipitation differences between US-VCM and US-GLE, 100 mm rain precipitation between US-NR1 and ER-PK. Climate forcing across the sites shows much stronger heterogeneity than the heterogeneity observed in the annual ET. ANOVA with annual ET data rejects the null hypothesis, which suggests at least the mean of annual ET in one of the six sites is statistically different from the others. Tukey's test further indicates that with a 95% family-wise confidence level there is no significant difference in annual ET between the following pairs: ER-SP and ER-BT, US-NR1 and ER-BT, US-VCM and ER-BT, US-NR1 and ER-SP, US-VCM and ER-SP, US-GLE and ER-PK, US-VCM and US-NR1. Table 4.2 displays the results from Tukey's test on annual ET.

The heterogeneity in climate forcing attributes across these sites is likely influenced by their latitudes, elevation and other local scale factors. For example, we observe greatest air temperature at US-VCM, followed by the three SNOTEL sites and US-NR1 with US-GLE having the lowest air temperature. On the other hand, maximum annual solar radiation is observed for US-GLE, followed by SNOTEL sites and US-NR1, with US-VCM as the lowest. Rain and snow patterns across these six sites are complex. We observe greater rain at US-NR1 and US-VCM, whereas ER-PK has the smallest annual rain totals. The largest snow amounts are observed at US-GLE and ER-SP, whereas the lowest snow total generally occurs at US-VCM. Even though these six sites are located along the Rocky Mountain ranges, they span a wide range of latitudes, which leads to significant differences in their energy inputs as well as precipitation inputs. Spatial heterogeneity of snow and total precipitation minus ET (P – ET) also appears to be associated with energy inputs and latitudes; we observe the greatest snow totals and P – ET at US-GLE, followed by US-NR1, with US-VCM having the lowest snow total and P – ET. However, this relationship becomes much more complex when we further consider the three SNOTEL sites that have similar latitude. We observe similar annual snow precipitation between ER-SP and US-GLE; ER-BT and US-NR1, however, annual P – ET of ER-BT is closer to US-VCM. Despite significant differences in energy and precipitation patterns among these sites, we observe some similarity in the temporal distribution of annual ET between US-NR1 and US-VCM; ER-BT and ER-SP; ER-PK and US-GLE, which suggests the necessity to capture the intra-annual variability of ET dynamics influenced by hydroclimate changes.

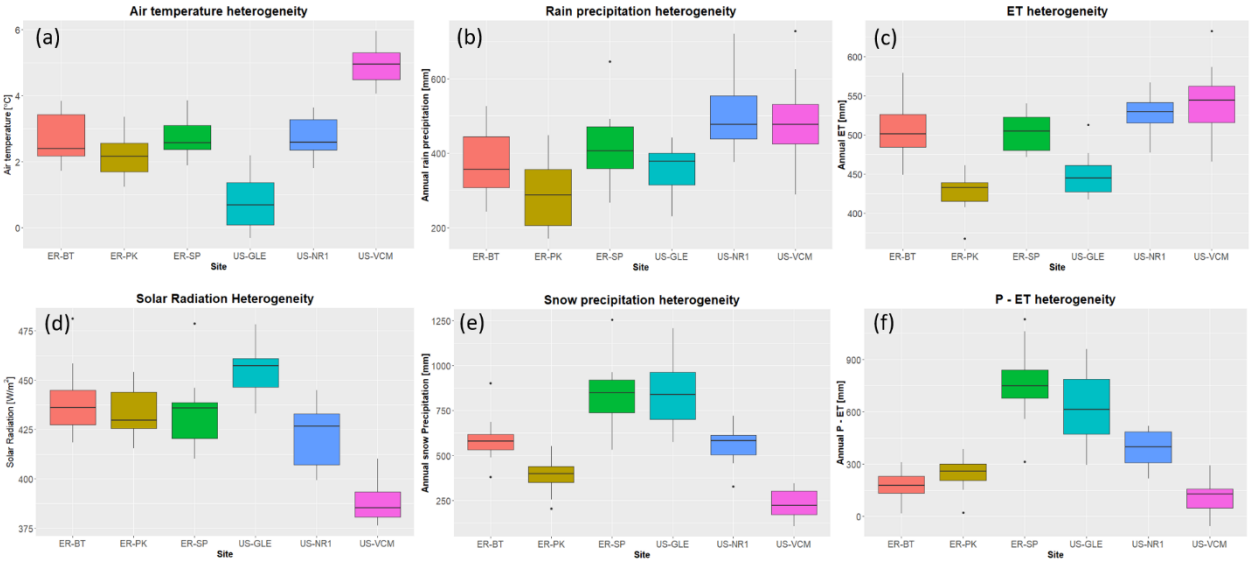

Figure 4.3 Spatial heterogeneity in hydroclimate attributes, ET and P-ET across six sites.

Table 4.2 Tukey's test result indicate differences in annual ET for certain pairs at familywise 95% level. Significance level is set at 0.05

Site 1	Site 2	Difference in mean annual ET [mm]	Lower Bound [mm]	Upper Bound [mm]	p-value	Significant
ER-SP	ER-BT	-0.74	-39.55	38.07	0.99	No
ER-PK	ER-BT	-78	-116.83	-39.21	0.00	Yes
US-NR1	ER-BT	21.47	-17.34	60.28	0.59	No
US-GLE	ER-BT	-55.65	-94.46	-16.84	0.00	Yes
US-VCM	ER-BT	36.33	-2.48	75.15	0.08	No
ER-PK	ER-SP	-77.28	-116.09	-38.46	0.00	Yes
US-NR1	ER-SP	22.21	-16.60	61.02	0.55	No
US-GLE	ER-SP	-54.91	-93.72	-16.10	0.00	Yes
US-VCM	ER-SP	37.07	-1.74	75.89	0.07	No
US-NR1	ER-PK	99.49	60.68	138.30	0.00	Yes
US-GLE	ER-PK	22.34	-16.44	61.18	0.54	No
US-VCM	ER-PK	114.35	75.54	153.17	0.00	Yes
US-GLE	US-NR1	-77.12	-115.93	-38.31	0.00	Yes
US-VCM	US-NR1	14.86	-23.95	53.68	0.87	No
US-VCM	US-GLE	91.98	53.17	130.80	0.00	Yes

4.5.2 Characteristics of temporal regimes

In this section, we presented the statistical summary of meteorological forcing attributes determined for each temporal regime and demonstrate the physical representation of each determined temporal regimes and how dynamic changes in hydroclimate govern ET dynamics. With the proposed framework, six temporal regimes (R0 – R5) that have distinct statistical characteristics in meteorological forcing attributes were determined. Figure 4 presents the temporal regime-based distribution of air temperature (Figure 4.4a), solar radiation (Figure 4.4b), regime durations (Figure 4.4c) ET (Figure 4.4d), rain precipitation (Figure 4.4e), snow

precipitation (Figure 4.4f) and net precipitation minus ET (Figure 4.4g) across all six sites and years considered.

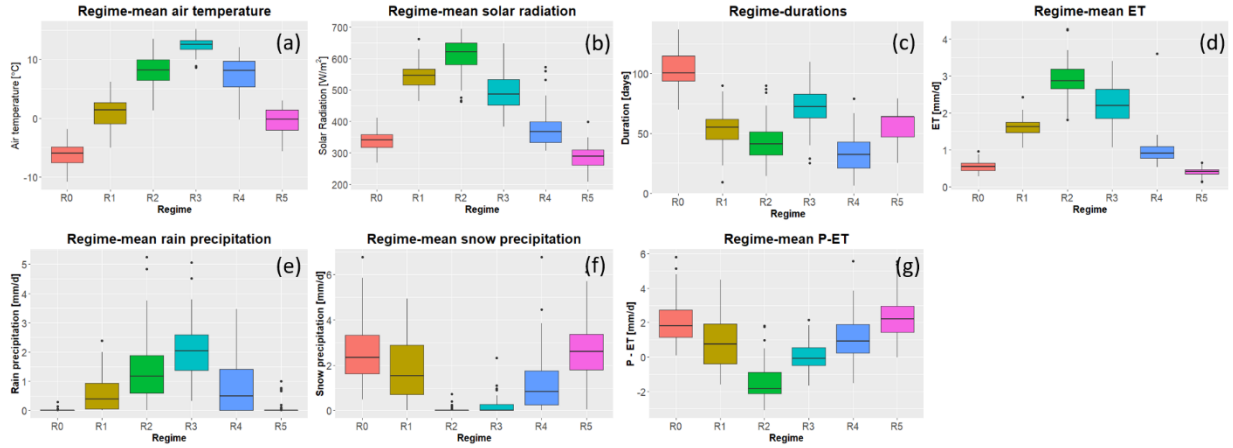

Figure 4.4 Statistical summary of temporal regime based characteristics of daily air temperature, solar radiation, regime durations, ET, rain precipitation, snow precipitation, and net precipitation minus ET at all six sites across 10 years considered in this study

As calendar year was used in this study, temporal regime R5 and R0 represents the period of time that the watershed is covered under snow, which has minimum temperature, minimum solar radiation and minimum ET. The duration of R5 and R0 is largely controlled by snow precipitation and the effective accumulation of snow during the winter time. During R0 and R5, positive P – ET is observed. Towards the end of R0, as temperature is reaching above freezing point and solar radiation increases, R0 and R1 transition happens following the start of snowmelt. During R1, sufficient soil moisture is supplied from melted snow and supports nutrient transport in the subsurface. However, due to limited energy conditions (e.g., low air temperature), R1-based ET is still very small (~ 1.6 mm/d). Snow disappearance usually occurs at the end of R1 and bareground date is highly correlated with the day of R1-R2 transition. Duration of R1 is important as it controls the amount of soil moisture from snowmelt that can be potentially used to support vegetation growth at later temporal regimes. During R1, snowmelt water also contribute to groundwater and stream recharge, which are necessary for plant dynamics during later regimes.

Following R1, R2 represents the period of time during which the watershed experiences maximum radiation that supports vegetation growth. At the beginning of R2, rate of vegetation growth is very high due to ambient soil moisture from snowmelt and radiation, where we observed increase in ET. Comparing to other regimes, we observed the smallest P – ET in R2. However, with certain combinations of meteorological conditions (e.g., late monsoon and earlier snowmelt), decreases in R2-mean ET can occur due to occurrences of droughts, such as year 2012. Our current approach does not explicitly determine a drought regime, however the occurrence of fore-summer drought within R2 is highly dynamic and happen with earlier R1-R2 transition (earlier snowmelt) and late R2-R3 transition (later monsoon). R2-R3 transition is controlled by the first effective monsoon, which greatly eases the potential drought condition posed in R2. Compared to R2, R3 has the highest rain precipitation inputs, and these monsoon precipitation provide additional water supply for ET that support both plant transpiration and soil evaporation. However, as the solar radiation input is small, R3-based ET is smaller than R2 due

to decreasing evaporative demands. The changes in meteorological forcing between R2 and R3 also suggests different partition of ET into transpiration and evaporation. For example, transpiration is likely greater in R2 than R3, whereas evaporation is greater in R3 compared to R2. Correspondingly, P-ET varies around 0, indicating the competition between potential drought condition due to high ET demand and monsoon precipitation inputs.

R3 and R4 transition usually takes place in late autumn and correspond to the defoliation period, where temperature and radiation is low, and most plants are adapting to winter dynamics and reduce ET significantly. Though rainfall precipitation still occurs in R4, this increasing moisture input does not contribute to ET due to energy limiting condition and limited plant productivity. R4-R5 transition is triggered when temperature decreases to the freezing point. R5 marks the start of winter, where the ecosystem has minimum ET and extends to R0 until snowmelt initiate the transition to R1. Overall contribution of ET from R4, R5 and R0 are very small compared to the other temporal regimes due to very small regime based ET (limited plant functionality and evaporative demands).

4.5.3 Intra-annual variability of ET

Within-regime Following R1, R2 represents the period of time during which the watershed experiences maximum radiation that supports vegetation growth. At the beginning of R2, rate of vegetation growth is very high due to ambient soil moisture from snowmelt and radiation, where we observed increase in ET. Comparing to other regimes, we observed the smallest P – ET in R2. However, with certain combinations of meteorological conditions (e.g., late monsoon and earlier snowmelt), decreases in R2-mean ET can occur due to occurrences of droughts, such as year 2012. Our current approach does not explicitly determine a drought regime, however the occurrence of fore-summer drought within R2 is highly dynamic and happen with earlier R1-R2 transition (earlier snowmelt) and late R2-R3 transition (later monsoon). R2-R3 transition is controlled by the first effective monsoon, which greatly eases the potential drought condition posed in R2. Compared to R2, R3 has the highest rain precipitation inputs, and these monsoon precipitation provide additional water supply for ET that support both plant transpiration and soil evaporation. However, as the solar radiation input is small, R3-based ET is smaller than R2 due to decreasing evaporative demands. The changes in meteorological forcing between R2 and R3 also suggests different partition of ET into transpiration and evaporation. For example, transpiration is likely greater in R2 than R3, whereas evaporation is greater in R3 compared to R2. Correspondingly, P-ET varies around 0, indicating the competition between potential drought condition due to high ET demand and monsoon precipitation inputs.

Dynamics in meteorological forcing attributes extend or shorten the duration of temporal regimes and thus re-partition the annual cumulative ET into different temporal regimes. At ER-BT, within-R1 cumulative ET varies from 64 mm to 126 mm and within-R2 cumulative ET varies from 77 mm to 187 mm where annual ET ranges from 446 mm to 579 mm between 2005 and 2016. Through comparing the within regime cumulative ET between 2011 and 2015, we determined that the differences in annual ET mainly resulted from within-R3 cumulative ET (124 mm vs 233mm), indicating adequate precipitation events and radiation inputs during the prolonged monsoon season in 2015 is the major driver that lead to the discrepancy in annual ET between 2011 and 2015; whereas ET dynamics during snowmelt periods, growing season and other regimes are similar in these two years. These results further indicate that differences in annual ET dynamics can be explained by differences contributed from certain regimes, where regime duration and transitions lead to the short-term and long-term temporal variability of ET.

We also observed significant fluctuations in annual ET, within-regime ET and regime durations across the six watersheds. For example, at US-NR1 and US-GLE, we have identified greater contribution in annual ET from within-R0 and within-R1 ET whereas within-R3 ET is significantly greater at US-VCM. Correspondingly, longest duration of R3 was observed at US-VCM, whereas longest duration of R1 occurs at US-GLE and US-NR1 (Figure E.1). These comparisons further distinguish the disproportionate effects of regimes in regulating intra-annual variability of ET across these Rocky Mountain watersheds.

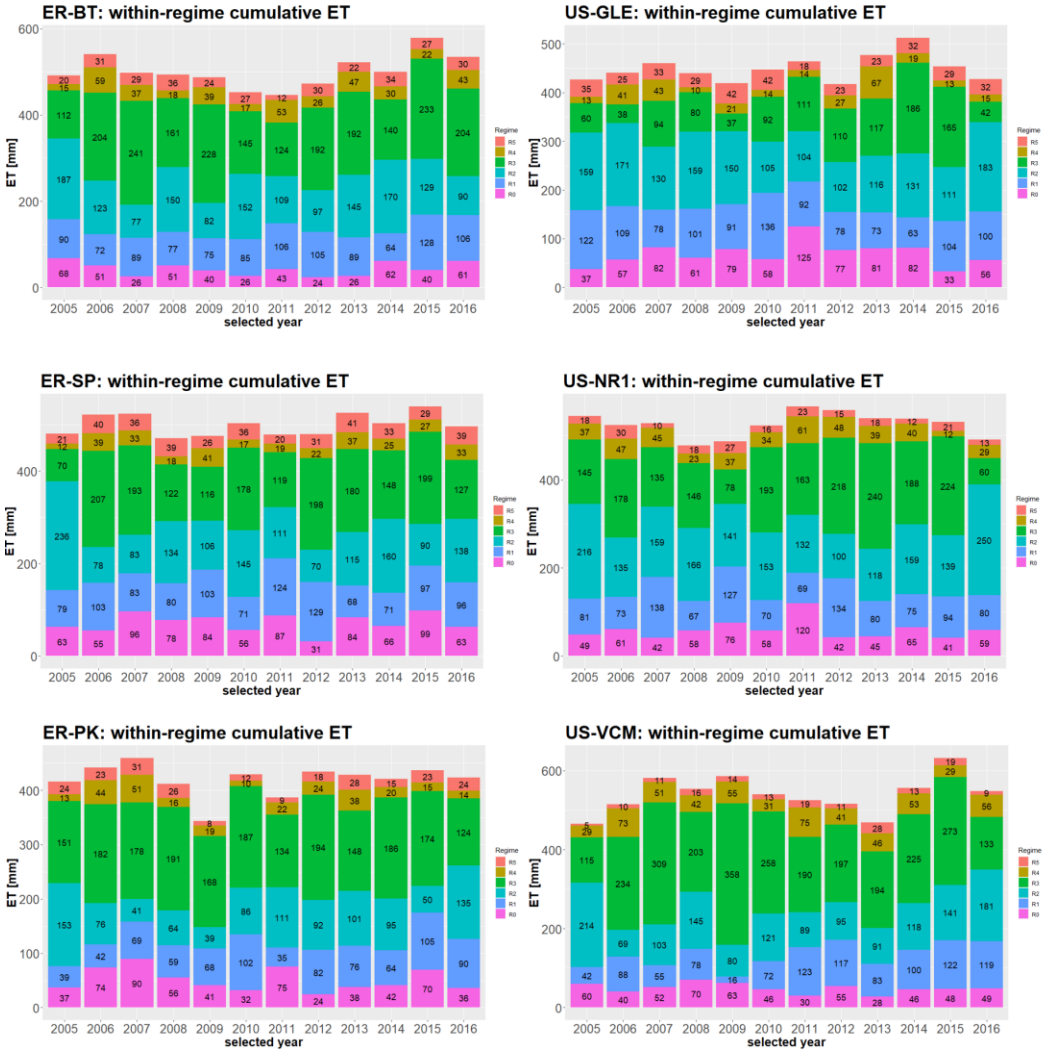

Figure 4.5 Temporal regime dependent partitioning of ET. Numbers within each column represents the amount of within-regime ET.

4.5.4 Timing and duration of temporal regime as the key controls for within-regime cumulative ET and annual ET

The magnitude of each within-regime cumulative ET contributes to annual ET. Duration of temporal regimes and regime-mean ET control within-regime cumulative ET, and thus influence the inter-annual variability of annual ET. Figure 4.6 presents the correlation between temporal regime duration and within regime cumulative ET. At each temporal regime, ET fluctuates

around its regime-mean ET, which is relatively constant across various years and sites (k in Figure 4.6). Thus, the duration of temporal regimes is an important factor that leads to spatiotemporal variability in annual ET. Earlier snowmelt, extended-foresummer drought or changes in other watershed dynamics reshapes the duration of temporal regimes, which further influences annual ET. Considering all years and sites, high correlations between regime durations and within-regime cumulative ET were observed for R0-R5, which suggested an overall similarity in within-regime ET across the various sites. Regime-mean ET for R0-R5 is at 1.1, 1.5, 2.4, 2.7, 0.96 and 0.55 mm/d respectively. Prolonged duration of R2 and R3 increase the annual ET due to high regime-mean ET in R2 and R3. Adequately prolonged duration of R0 and R5 caused by higher snow precipitation and colder winter increases R0 and R5 duration and delays R1-R2 transition and snowmelt, which provide sufficient water supply during high solar radiation that lead to an overall increase in annual ET. However, if the duration of R0 and R5 becomes excessive, it significantly decreases R2 and R3 duration and reduces annual cumulative ET. Further, ET dynamics also experience compensatory effects of these two temporal regimes (i.e., extended R2 and shortened R3 vs. shortened R2 and extended R3), leading to minor differences in annual ET (further explored in section 4.5.6).

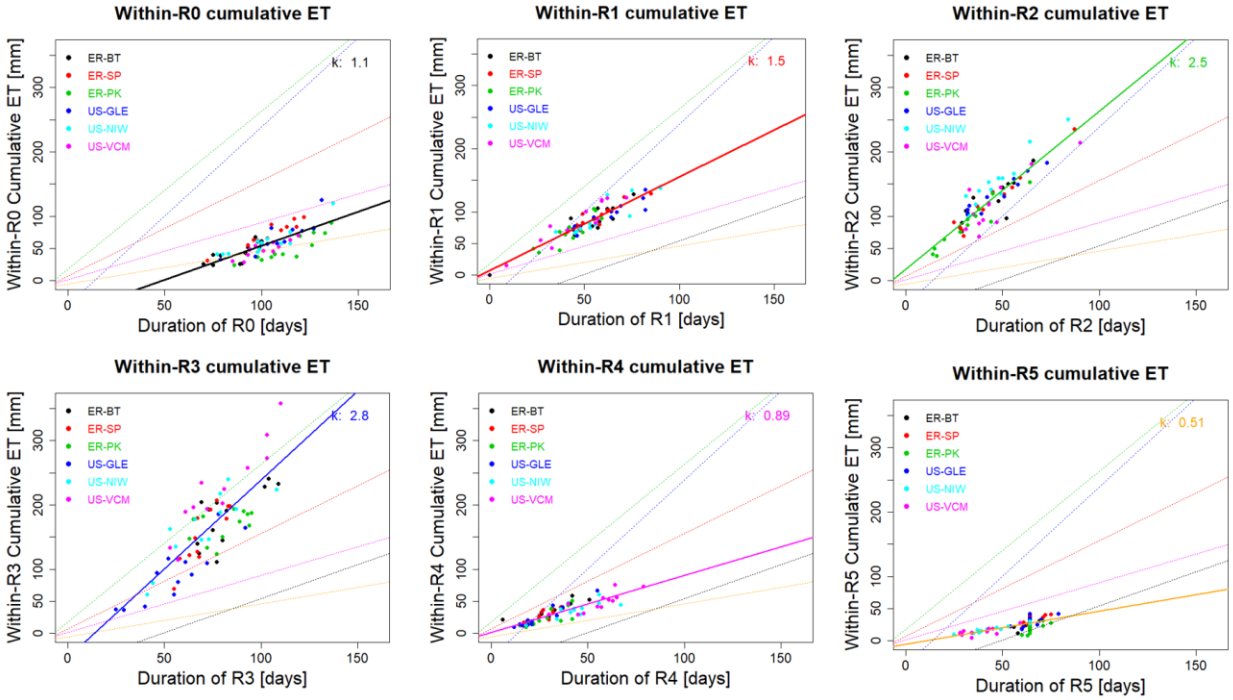

Figure 4.6 Correlation between hydroclimate regime duration and within-regime cumulative ET. Colored points represent different sites. Colored lines are regression lines for each hydroclimate regime between within-regime cumulative ET and hydroclimate regime duration. k values measure regime-mean ET [mm/day].

4.5.5 Linking temporal regimes with dynamics observed in the physical environment

We used data at US-NR1 as an example to present the coherency between various observations in the physical environment and assess how they're related with the timing of hydroclimate regime shifts. Figure 4.7 presents the time series of snow water equivalent (SWE), ET, soil temperature, and soil water content of 2008 and 2012 at US-NR1. Temporal consistency in all these processes are observed, including date of maximum snow depth, first day of snow

disappearance (bareground date), and day of air and soil temperature above 0℃. This result suggests changes in one aspect of the hydroclimatological dynamics (e.g., snow) are coherent with changes in other aspects (e.g., soil temperature and ET). The coherency and covariability in ET and soil moisture (Figure 8) indicate the plausibility of using statistical characteristics to determine intra-annual variability, such as proposed in this study.

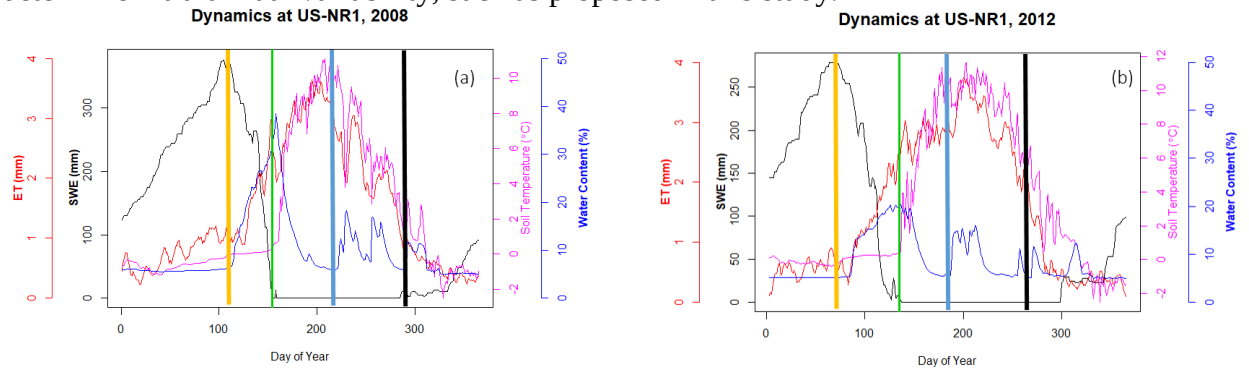

Figure 4.7 Coherency in the timing of watershed dynamics. Panel (a) and (b) present snow water equivalent (SWE, black), ET (red), soil temperature (Pink), and soil water content (blue) time series. Orange, green, blue and black vertical lines representing R0-R1 transition, R1-R2 transition, R2-R3 transition and R3-R4 transition, respectively. 2008 and 2012 are selected due to their divergence in climate forcing with 2012 having earlier snowmelt and earlier monsoon and 2008 having later snowmelt and later monsoon.

Temporal regimes provide a quantitative approach to unify the linkages among different dynamic processes. Figure 4.8 presents inter-annual variability of data based indices, including bareground date, day of minimum net ecosystem exchange (NEE), day of maximum gradient in soil temperature, day of maximum soil moisture at US-NR1 supported by Fluxnet data, where R0-R1 and R1-R2 transition date were also used for comparison. As regimes were determined upon the interactions among multiple dynamics, regime transitions are not identical to specific data based indices but a statistical significant correlation among regime transition dates and the other commonly used indices were observed. For example, R0-R1 transition date that represents the watershed transits from a snow accumulation regime to snowmelt regime is highly correlated with the occurrence of bareground date, day of maximum soil moisture, and maximum gradient with correlation coefficient above 0.8. Similarly, R1-R2 transition that distinct snowmelt regime and growing season regime is also highly correlated with these indices. This result indicated that the temporal regimes and regime shifts are able to integrate multiple ecosystem dynamics (e.g., snowmelt, temperature rising, monsoon etc.) as a whole to determine the intra-annual variability dynamics. Such coherency in dynamic processes has also been reported in other studies. For example, soil moisture dynamics and timing of snowmelt are highly correlated (Harpold & Molotch, 2015); dynamic changes in meteorological forcing also leads to temporal variations in ecosystem respiration and gross primary production (Berryman et al., 2018; Knowles et al., 2016); and fore-summer drought occurrences are also highly linked with the timing of snowmelt and shifts in energy inputs (Sloat et al., 2015; Wainwright et al., 2020). Thus, even if our current study focuses on using temporal regimes and regime shifts to assess the intra-annual variability of ET dynamics, our proposed approach can be also applied towards other ecosystem dynamics, such as ecosystem respiration and gross primary production.

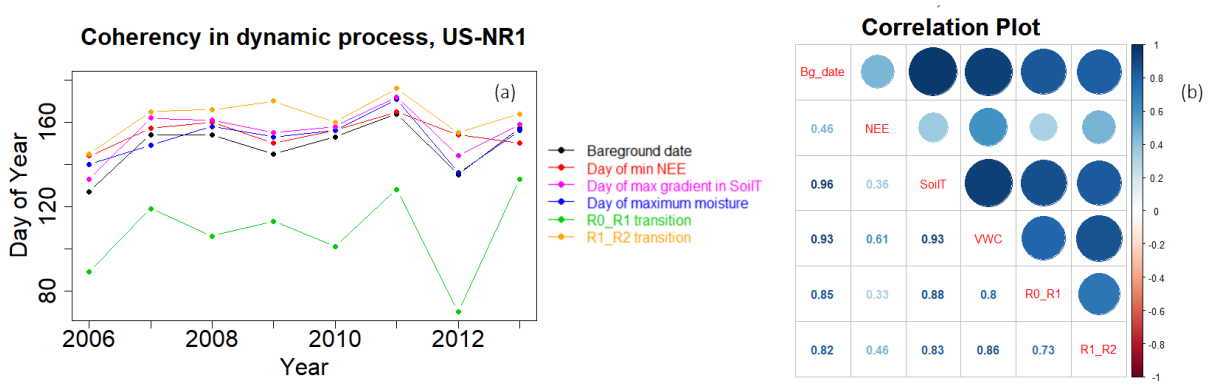

Figure 4.8 Coherency between hydrological indices, R0-R1 and R1-R2 transitions at US-NR1

4.5.6 Evaluate inter-annual variability in ET through intra-annual variability determined with temporal regimes

We further used the determined temporal regimes to investigate the major contributors that lead to the inter-annual variability of ET. We specifically considered 2008 and 2012, as 2008 represents a year in the Rocky Mountains having above average snow precipitation and later snowmelt and 2012 depicts a situation with significantly less than average snow precipitation and very early snowmelt with identified fore-summer drought in the Colorado sites (Sloat et al., 2015). ET dynamics in 2008 and 2012 are very different due to differences in hydroclimate dynamics. At ER-BT, we observed approximately 3 weeks earlier R0-R1 transition in 2012 (75^{th} day) due to earlier snowmelt compared to 2008 (99^{th} day), where snow has not begun to melt until April. R1-R2 transition is 2 weeks apart between 2008 (153th day) and 2012 (137^{th}) due to different rate of snowmelt (Figure E.2). R2-R3 transition in 2012 happened at the 189^{th} day compared to 205^{th} day in 2008 at ER-BT, which provided monsoon soil moisture that relieved the effect of fore-summer drought. At the other Colorado sites (i.e., ER-SP, ER-PK and US-NR1) and US-VCM, we observed a similar earlier R0-R1 and R1-R2 transition in 2012 compared to 2008. However at US-GLE, R0-R1 and R1-R2 transition were not following the similarity as we observed in the Colorado sites. US-GLE usually have longer R0 and R1 durations due to its higher latitude and more accumulation of snow during winter.

Variability in annual ET across different years is also largely controlled by the intra-annual variability of ET through within-regime cumulative ET. Though we have observed significant differences in the timing of ET dynamics between 2008 and 2012 at ER-BT, annual ET was 493 mm for 2008 and 474 mm for 2012. Correspondingly, we observed +27 mm differences in within-R0 ET, -28 mm differences in within-R1 ET, +53 mm differences in within-R2 ET, and -31 mm differences in within-R3 ET. The strong decrease of ET during R2 in 2012 due to earlier snowmelt was compensated by earlier monsoon. These results showed that intra-annual variability of ET can vary significantly across different years, however, result in significantly less differences in annual ET due to the compensatory effects between different temporal regimes. At ER-BT, precipitation from monsoon becomes more essential for ET and plant growth for years that experience significant earlier snowmelt (e.g., 2012) compared to other scenarios where ambient moisture supply due to later snowmelt contributes more ET during snowmelt and growing periods, which together result in smaller differences in annual ET. At US-GLE, annual ET was 439 mm for 2008 and 417 mm for 2012. Though R0-R1 transition between 2008 and 2012 is not as significantly different as the Colorado sites, different contributions from

within-R2 and within-R3 ET result in the overall differences in annual ET. Similarly at US-VCM, differences in annual ET between 2008 and 2012 was largely caused by within-R2 ET (145 mm in 2008 versus 95 mm in 2012).

With the example of ET dynamics at 2008 and 2012, we determined which changes in meteorological conditions caused significant differences in temporal regime durations and within regime ET over different years. Inter-annual variability in annual ET is largely controlled by the combinational effects from all temporal regimes. Thus quantifying the intra-annual variability is necessary to better understand these dynamics.

4.6 Summary

In this chapter, we developed the framework of temporal regimes to better characterize the intra-annual variability of ET dynamics at mountainous watersheds. With this method, we were able to determine the dominant factors for temporal regimes in the central Rocky Mountains, including transitions between temporal regimes; the duration of temporal regimes and within-regime cumulative ET. Our proposed framework of temporal regimes is advantageous as it can quantitatively distinguish the distinct contribution from intra-annual dynamics to inter-annual variability and assess the major limiting processes The use of temporal regimes also enabled us to distinguish the temporal variability of season durations, which is important for water and energy resources management.

Intra-annual variability in ET is the major driver that leads to spatiotemporal variability of ET across the six watersheds and across all years. With the statistical framework, we quantitatively characterize the durations and occurrences of regimes related with snow, snowmelt, growing season, monsoon and defoliation. Differences in annual ET between different years result from disproportionate contribution from certain regimes with similar ET dynamics in other periods. For example, annual ET differences between 2011 and 2015 at ER-BT results from the disproportionate contributions from within-R3 ET during the monsoon season. Combinations of meteorological conditions also lead to compensatory effects in the intra-annual variability of ET, such as R2 and R3 ET dynamics in 2008 and 2012 at ER-BT. Temporal regimes also reveal the spatial heterogeneity in ET dynamics across the six watersheds. We observed greater ET contributions from snow-related regimes at US-GLE and US-NR1 than at US-VCM where ET contributions was more strongly driven by monsoon season. Our approach provides a unique perspective to better quantify spatiotemporal variability of ET dynamics and quantify contributions from each regime associated with seasonal events.

Regime-mean ET is relatively constant across all years and the six Rocky Mountain watersheds. Temporal regime duration and occurrences of regime transition are the pivotal factors that lead to the magnitude of annual cumulative ET. Combinations of different timing of snowmelt and monsoon, changes in temperature and precipitation patterns, significantly alter the duration of regimes and the contribution of ET from sub-annual dynamics, which can add complexity to the water and energy balance of mountainous watersheds. Earlier snowmelt, limited precipitation during R2 and ambient energy demand lead to a decrease in regime-mean ET in 2012, which indirectly indicating occurrence of fore-summer drought that were also discovered in Sloat et al. (2015) and Wainwright et al. (2020). However the earlier arrival of monsoon precipitation events ended the extended growing season regime and evolved the watershed into R3 and thus restored ET. Even if we observed a smaller within-R2 ET due to fore-summer drought, the earlier R2-R3 transition extended R3 and lead to increasing within-R3 ET. Thus intra-annual variability of ET indicated from temporal regimes is as significant as or

even greater than the inter-site and inter-annual variability of ET along the central Rocky Mountain regions. Quantifying intra-annual variability assists us to better understand the cause and effect linkages in the long-term trends of climate change, which are essential for managing water and energy resources.

It should be noted that the proposed statistical framework that focuses on understanding intra-annual dynamics also is flexible enough to be used to identify intra-annual variability of other processes, including carbon cycling, plant production and hydrological dynamics with the right data inputs for analysis. In this study, we have demonstrated the high correlation between regime-based transition dates and process-based indices, such as peak snow day, bareground date, and day of maximum soil moisture. If additional data becomes available (e.g., remote sensing, ecological and hydrological data), we believe our proposed approach can still be effective in quantifying intra-annual variability of other hydrological and ecological processes in future studies.

Chapter 5

Summary

The purpose of this dissertation was to improve the conceptual understanding of environmental Hot Spots and Hot Moments as well as the mathematical modeling of processes within mountainous watersheds. Particularly, this dissertation focuses on deriving statistical approaches to characterize the occurrence of HSHMs and the associated uncertainties; developing hybrid data-driven and physically-based model simulation approaches to estimate evapotranspiration and ecosystem respiration from stand scale to watershed scale; and assimilate statistical frameworks that could finally improve our understanding of HSHMs dynamics and mountainous watersheds ecosystem functioning. The previous three chapters investigated different aspects of the methodology and application, and presented the relevant findings.

With the recognition of current lacking of statistical quantifications of environmental HSHMs, Chapter 2 describes a statistical framework that utilizes indicator random variables to decompose HSHMs into the relevant processes and attributes. The proposed approach provides a general stochastic framework that can capture both transport-driven HSHMs as well as biogeochemical processes-driven HSHMs through the applications of static indicators and dynamic indicators. For example, static indicators can be constructed at locations that have higher pyrite concentrations or characterized as naturally-reducing zones through geophysical data that are necessary for nitrogen related HSHMs, whereas dynamic indicators can be constructed through the deployment of particle displacement probability density function that represent solute transport in the subsurface. The developed statistical framework significantly improves the capability to capture the uncertainties of HSHMs occurrences and provide an "easy-to-use" approach for future HSHMs predictions under various conditions. With the framework, we could relate HSHMs dynamics to the most influential parameters that could significantly reduce site characterization needs to capture HSHMs occurrences.

Understanding HSHMs occurrences at sparsely monitored mountainous watersheds relies upon long-term measurements, such as evapotranspiration and ecosystem respiration. However, due to the associated costs and efforts to establish and maintain eddy covariance flux towers at mountainous watersheds, ET and R_{ECO} data are mostly sparsely measured, which limits out ability to understand the occurrences of related ecohydrological HSHMs. In Chapter 3, we proposed a hybrid data-driven and physically-based modeling approach, namely Hybrid-Predictive-Modeling (HPM) approach, to predict ET and R_{ECO} at satisfactory spatial and temporal resolution with meteorological forcing data and remote sensing data. The proposed HPM approach utilizes deep-learning based long short-term memory recurrent neural network to establish temporal dependencies among ET, R_{ECO} and meteorological forcing attributes and remote-sensed vegetation indices (e.g., NDVI). In order to test the performance of HPM, we developed four use cases that cover a wide range of situations for ET and R_{ECO} estimation. Use Case 1 is mainly developed for estimating ET and R_{ECO} over time at local scale with HPM trained at local Fluxnet sites. High adjusted R^2 for all sites considered was observed indicating satisfactory performance of HPM approach. In Use Case 2 and Use Case 3, we tested HPM for ET and R_{ECO} estimation from one site to other sparsely monitored locations within the same ecoregion. Depending on data availability, data-driven HPM or mechanistic HPM can be applied. For various testing scenarios, HPM provides accurate and reliable estimation of ET and R_{ECO} for sparsely monitored watersheds within the same ecoregion. In Use Case 4, we integrated the previous three Use Cases to estimate ET and R_{ECO} at the mountainous East River Watershed, which is located in the Upper Colorado River Basin in the state of Colorado. With HPM-estimated ET and R_{ECO}, we were capable of distinguishing how heterogeneity in vegetation (e.g., vegetation types) and small-scale meteorological forcing control ET and R_{ECO} dynamics. With the remote-sensing derived NDVI time series, we determined different adaptation strategies for deciduous forests and evergreen forests in assimilating carbon and water usage under different meteorological conditions. Our results indicated similar annual ET and R_{ECO} budget for different vegetation types, however, diverse intra-annual variability. With the original intent to extract the role of topography and micrometeorology on ET and R_{ECO} dynamics, we recognized the uncertainties in meteorological forcing reanalysis data that significantly underestimate small-scale heterogeneity caused by slope, aspects, elevation gradient and other topographic features. In short, the proposed HPM approach significantly improved our predictive capability for ET and R_{ECO} estimation at mountainous watersheds, which then can be linked with the statistical framework proposed in Chapter 2 for ecohydrological HSHMs quantification that is necessary for better understanding of ecosystem dynamics under gradual and rapid climate change.

Findings discovered in Chapter 2 and Chapter 3 show the importance of capturing intra-annual variability in watershed ecosystems. From Chapter 2, we realized that HSHMs can occur at different temporal scales, bringing the importance of capturing HSHMs dynamics at both intra-annual cycles as well as inter-annual cycles. In Chapter 3, we discovered very small differences in annual ET and R_{ECO} at the East River Watersheds between deciduous forests and evergreen forests, the intra-annual variability is significantly different. Thus, in Chapter 4, we developed the framework of hydroclimate regimes to quantitatively and qualitatively identify intra-annual variability caused by dynamic changes in the hydroclimate to better assist our understanding of ecosystem dynamics and the occurrences of HSHMs, such as fore-summer drought. Hydroclimate regimes utilizes Hidden Markov Model to distinguish the temporal boundaries and duration of regimes through hydroclimate data inputs, including air temperature, soil temperature, precipitation and radiation. The identified regimes (e.g., R0-R5) enable us to

distinguish the duration of ecohydrological dynamics (e.g., snowmelt, fore-summer drought, growing season, defoliation) and assess their impacts over ET and other ecohydrological processes. With hydroclimate regimes, we were able to quantitatively characterize the durations and occurrences of regimes related with snow, snowmelt, growing season, monsoon and defoliation. The employment of hydroclimate regimes enables us to delineate the spatial component and temporal component of ET dynamics over the six sites over 10 years. The proposed hydroclimate regimes can fill in the current missing gaps that are needed to quantitatively and qualitatively assess the intra-annual variability of ET dynamics at mountainous watersheds.

Finally, although we focused on a limited number of sites and developed specific examples (Use Cases) to test and demonstrate the applicability of proposed approaches, these methods are applicable for other sites and other attributes. Thus, the approaches proposed in this dissertation still provide general formulations that are expected to further contribute to better understand watershed processes and model environmental HSHMs.

Appendix A

Flux Estimation and Validation for Chapter 3

A1. ET and R_{ECO} Estimation over Time at other Fluxnet sites

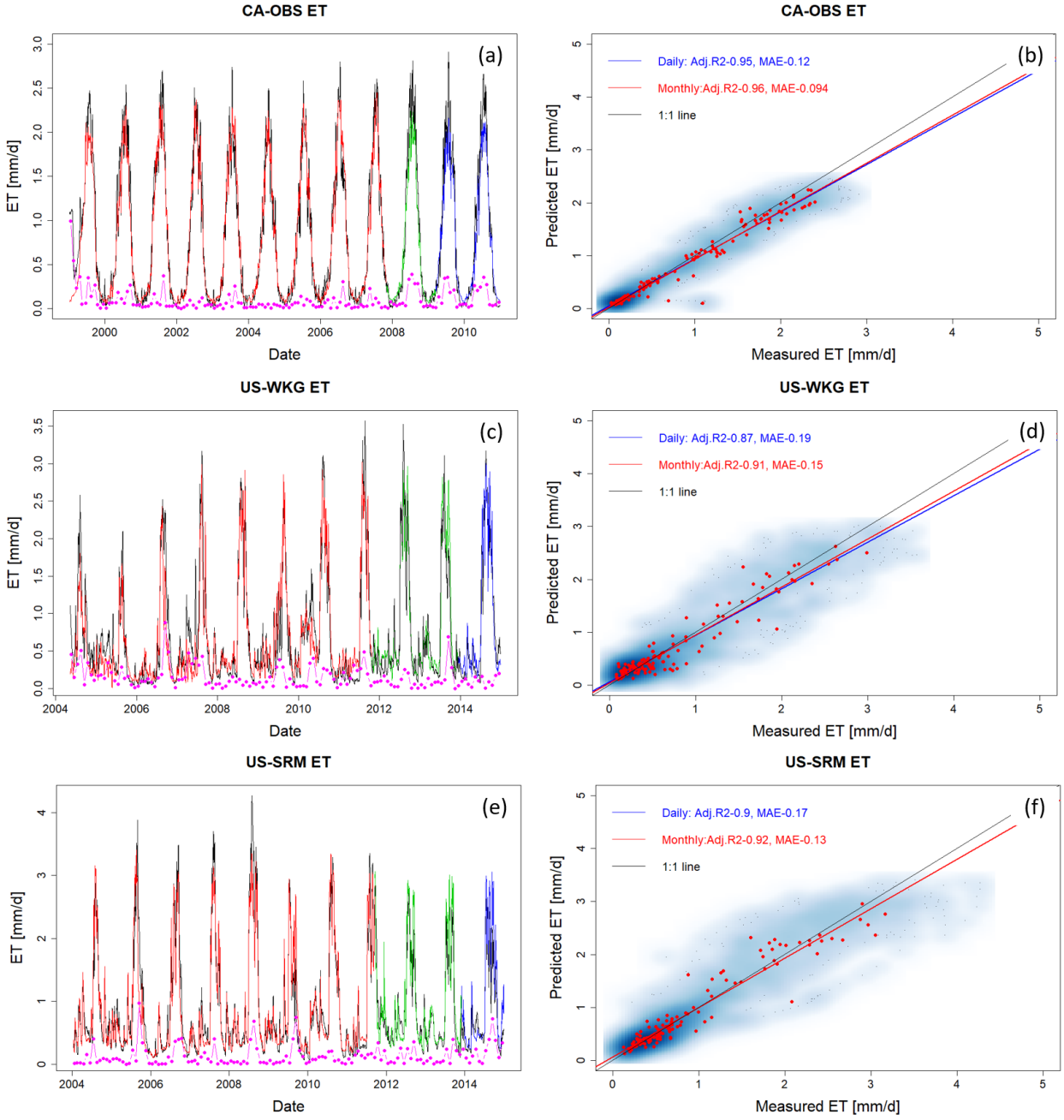

Figure A.1 ET estimation with data from selected FLUXNET sites at CA-OBS, US-Wkg, and US-SRM. Panels (a), (c), and (e) present daily estimations of ET with red, green, and blue lines representing data used for training, validation, and prediction, respectively, and the black line representing the eddy covariance measurement. Pink points describe monthly mean difference between HPM estimation and measured data. Panels (b), (d), and (f) show the scatter plots of daily (blue) and monthly (red) ET. Darker blue clouds represent greater density of data points.

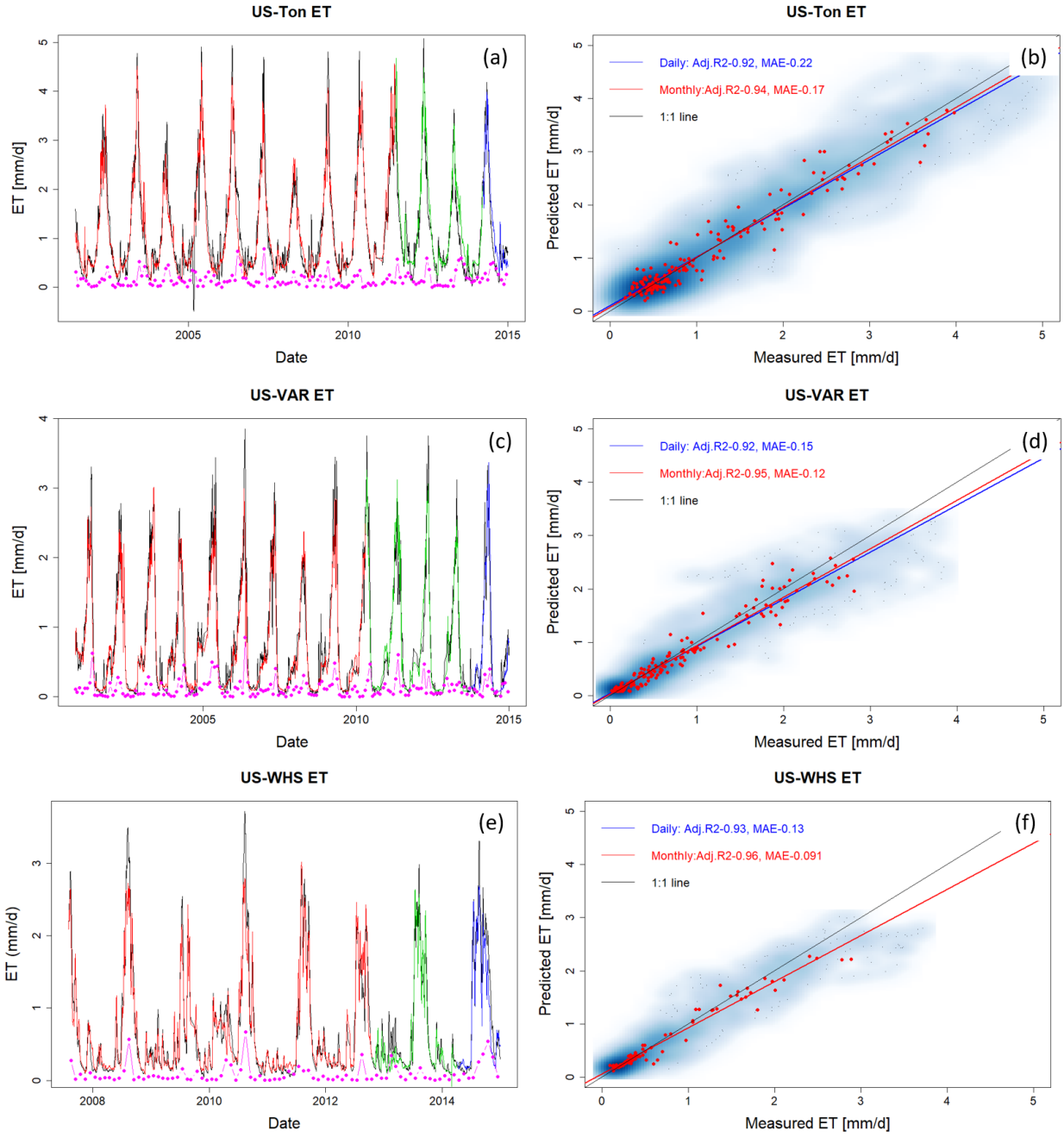

Figure A.2 ET estimation with data from selected FLUXNET sites at US-Ton, US-Var, and US-Whs. Panels (a), (c), and (e) present daily estimations of ET with red, green, and blue lines representing data used for training, validation, and prediction, respectively, and the black line representing the eddy covariance measurement. Pink points describe monthly mean difference between HPM estimation and measured data. Panels (b), (d), and (f) show the scatter plots of daily (blue) and monthly (red) ET. Darker blue clouds represent greater density of data points.

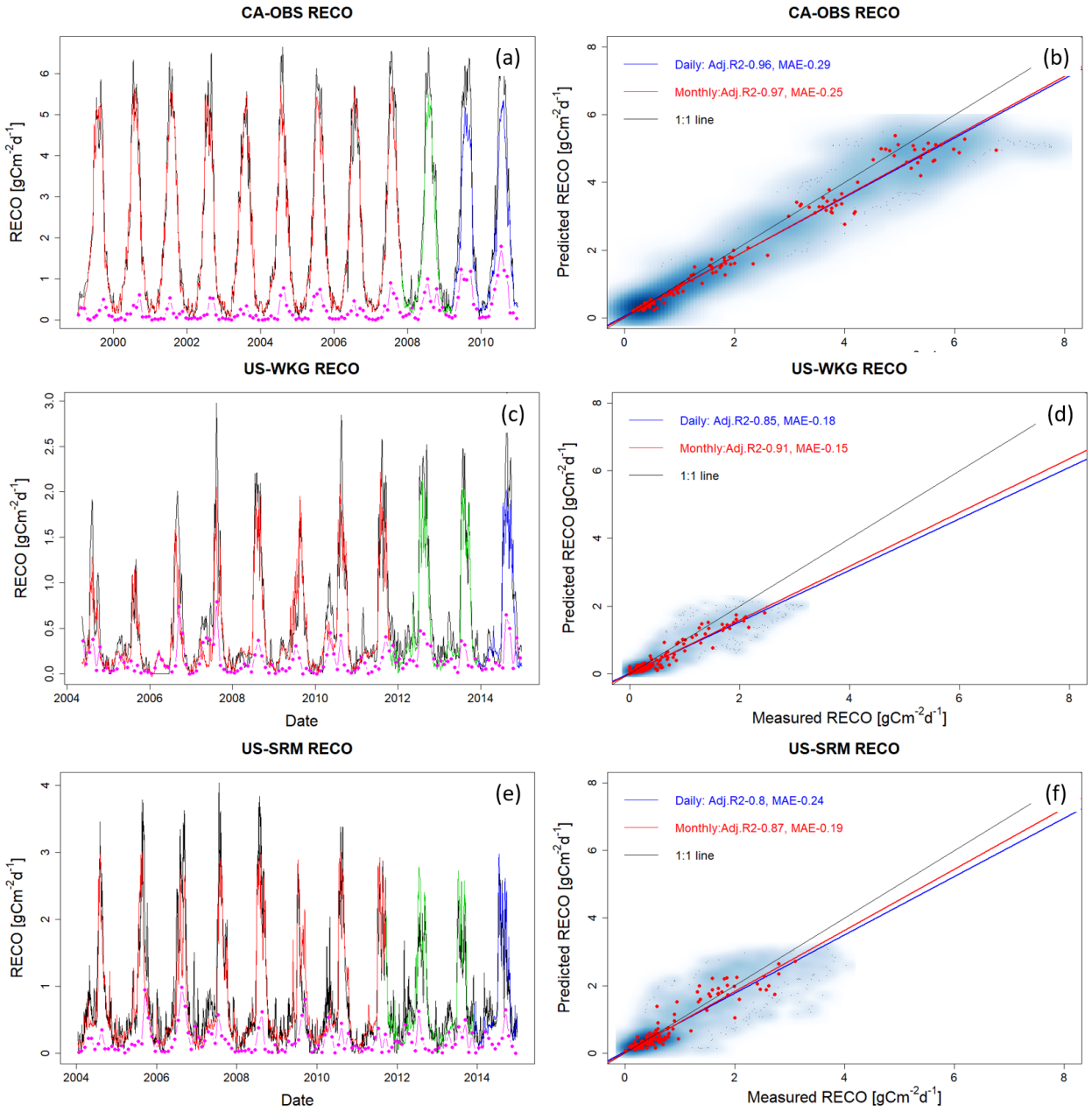

Figure A.3 R_{ECO} estimation with data from selected FLUXNET sites at CA-OBS, US-Wkg, and US-SRM. Panels (a), (c), and (e) present daily estimations of R_{ECO} with red, green, and blue lines representing data used for training, validation, and prediction, respectively, and the black line is eddy covariance measurement. Pink points describe the monthly mean difference between HPM estimation and measured data. Panels (b), (d), and (f) show the scatter plots of daily (blue) and monthly (red) R_{ECO}. Darker blue clouds represent greater density of data points.

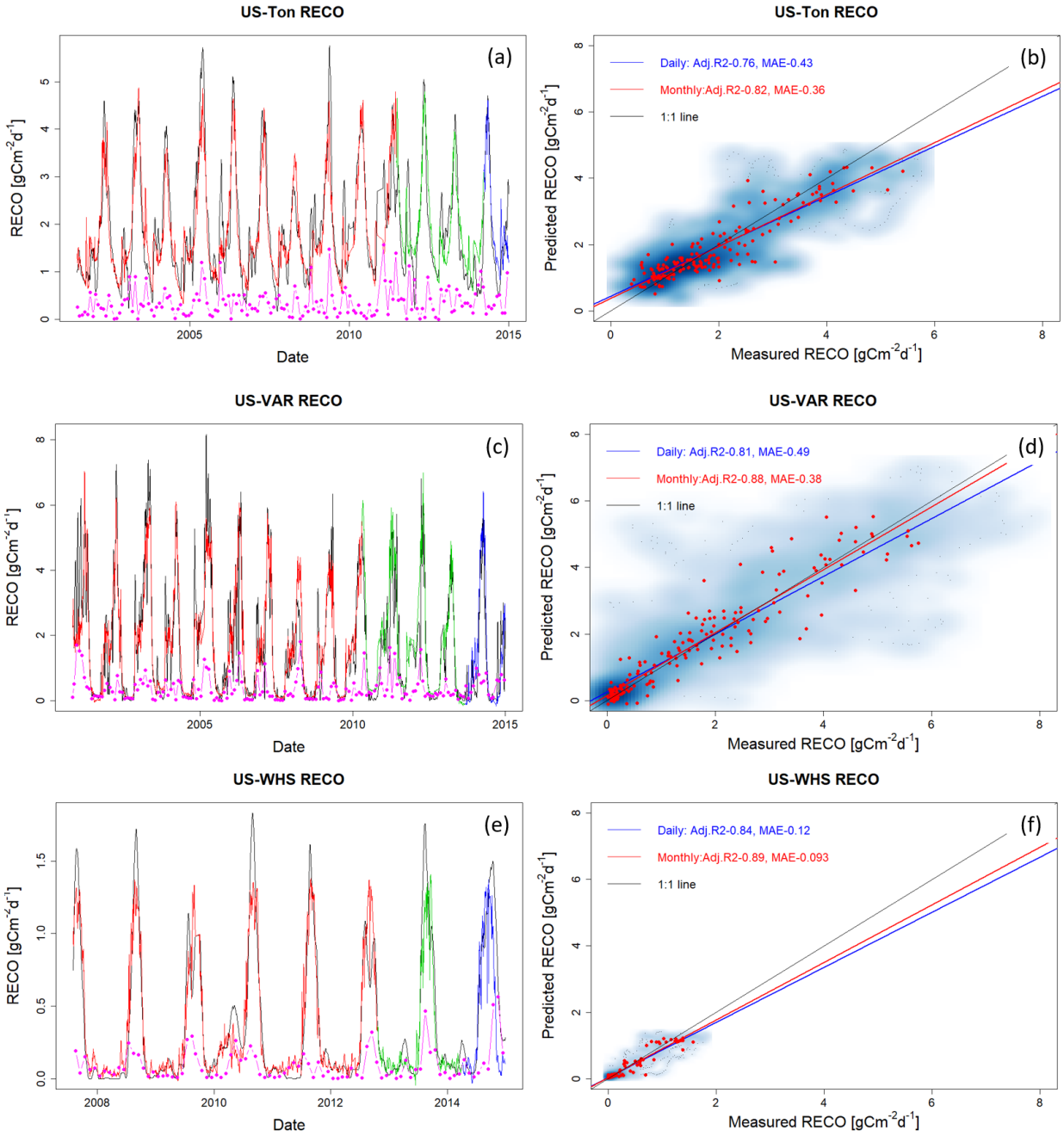

Figure A.4 R_{ECO} estimation with data from selected FLUXNET sites at US-Ton, US-Var, and US-Whs. Panels (a), (c), and (e) present daily estimations of R_{ECO} with red, green, and blue lines representing data used for training, validation, and prediction, respectively, and the black line representing the eddy covariance measurement. Pink points describe monthly mean difference between HPM estimation and measured data. Panels (b), (d), and (f) show the scatter plots of daily (blue) and monthly (red) R_{ECO}. Darker blue clouds represent greater density of data points.

Appendix B

HPM and MOD16A2 Comparison

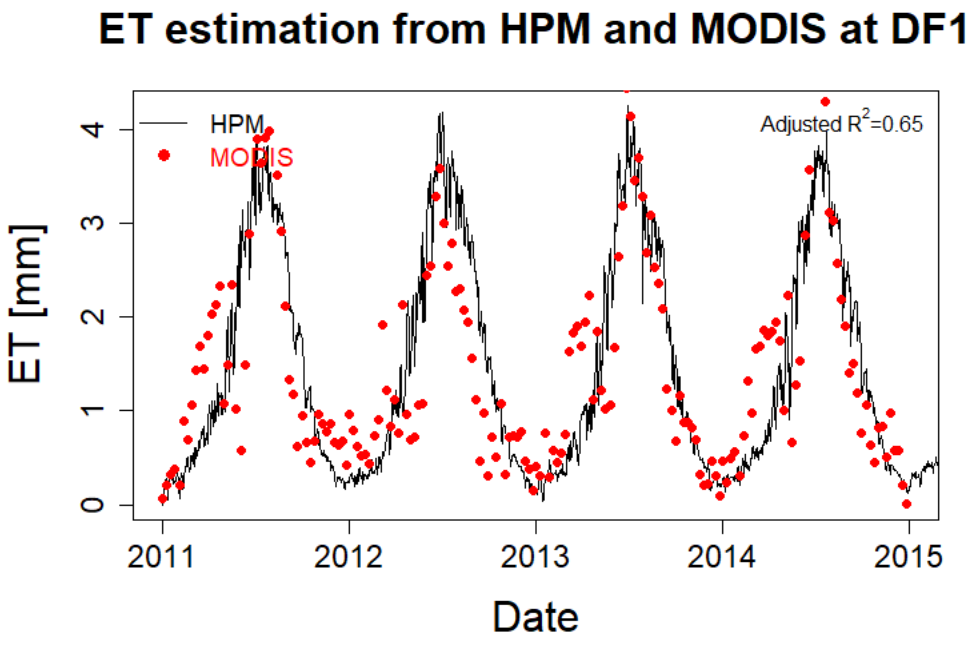

Figure B.1 Comparison of 8-day averaged ET estimation from HPM and Mu et al. (2013) at deciduous forests site in East River Watershed.

Appendix C

Meteorological Forcing Heterogeneity at East River Watershed

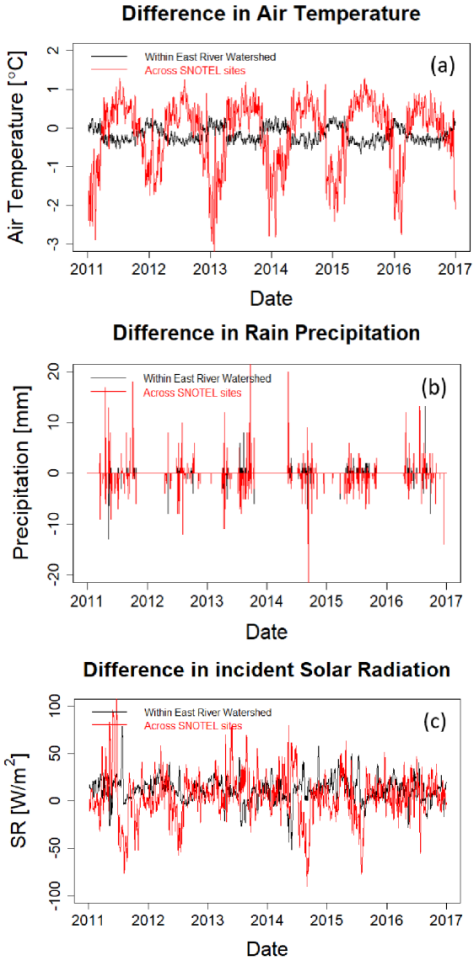

Figure C.1 Meteorological forcings heterogeneity within East River Watersheds (DF1 and EF1, black lines) with DAYMET data and across SNOTEL stations (ER-BT and ER-PK, red lines) with SNOTEL data.

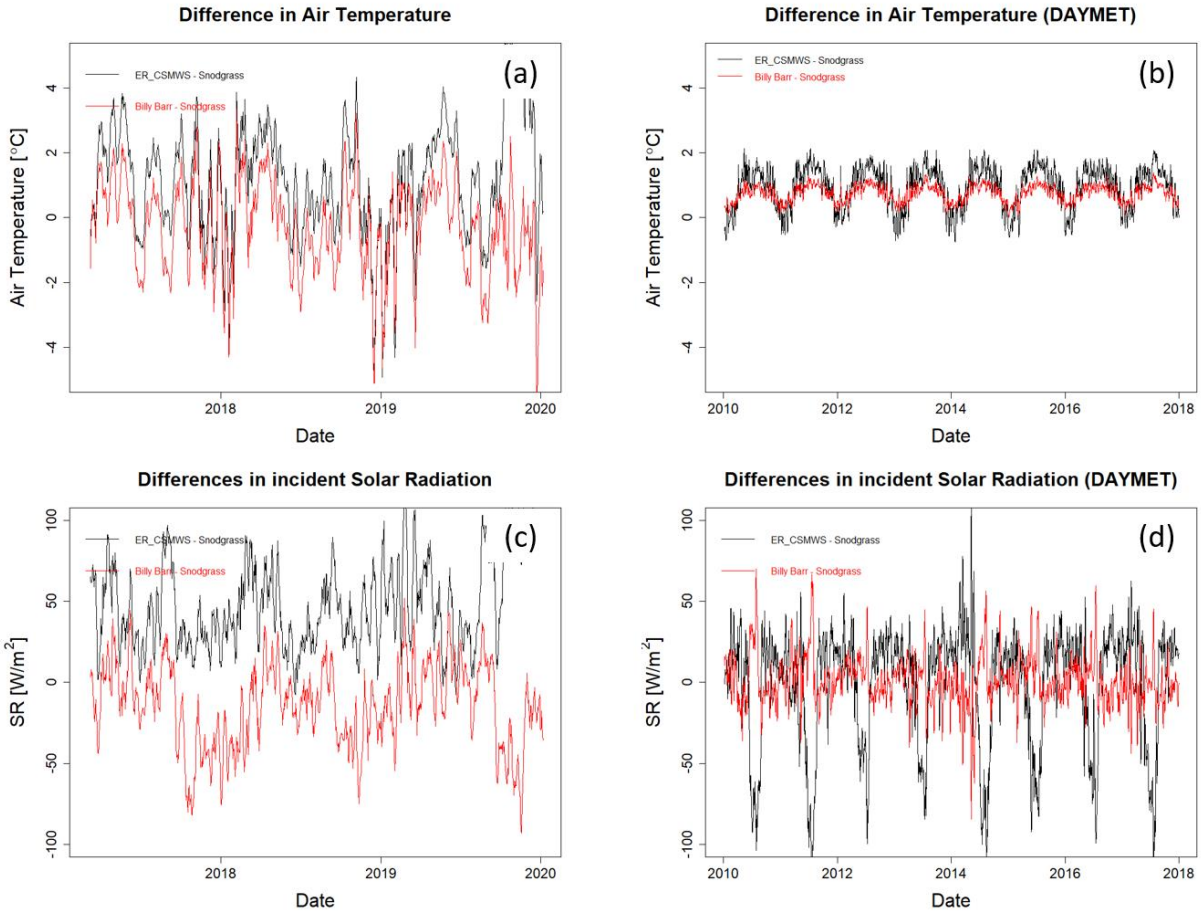

Figure C.2 Differences in air temperature and incident solar radiation among three weather stations (ER_CSMWS, Snodgrass and Billy Barr) locations within the East River Watershed. Panel (a) and (c) present data from weather stations obtained from https://wfsfa-data.lbl.gov/**. Panel (b) and (d) present data obtained from DAYMET.**

Appendix D

Community Land Model Performance

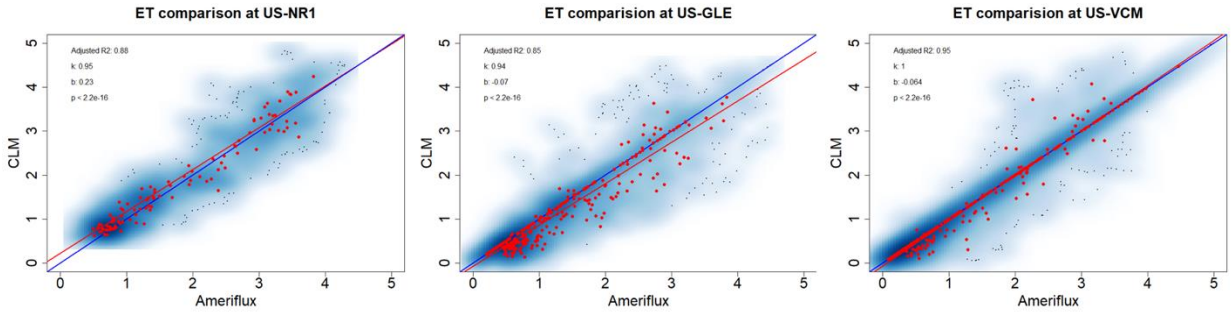

Figure D.1 Comparison between ET estimation from CLM and measurement from flux tower. MAE are $0.22, 0.25, 0.11mm$ for US-NR1, US-GLE and US-VCM, respectively. Red points represent monthly mean values and blue clouds represent the density of scattered points. Units are mm/day for both axis.

Appendix E

Temporal Distribution of Regimes

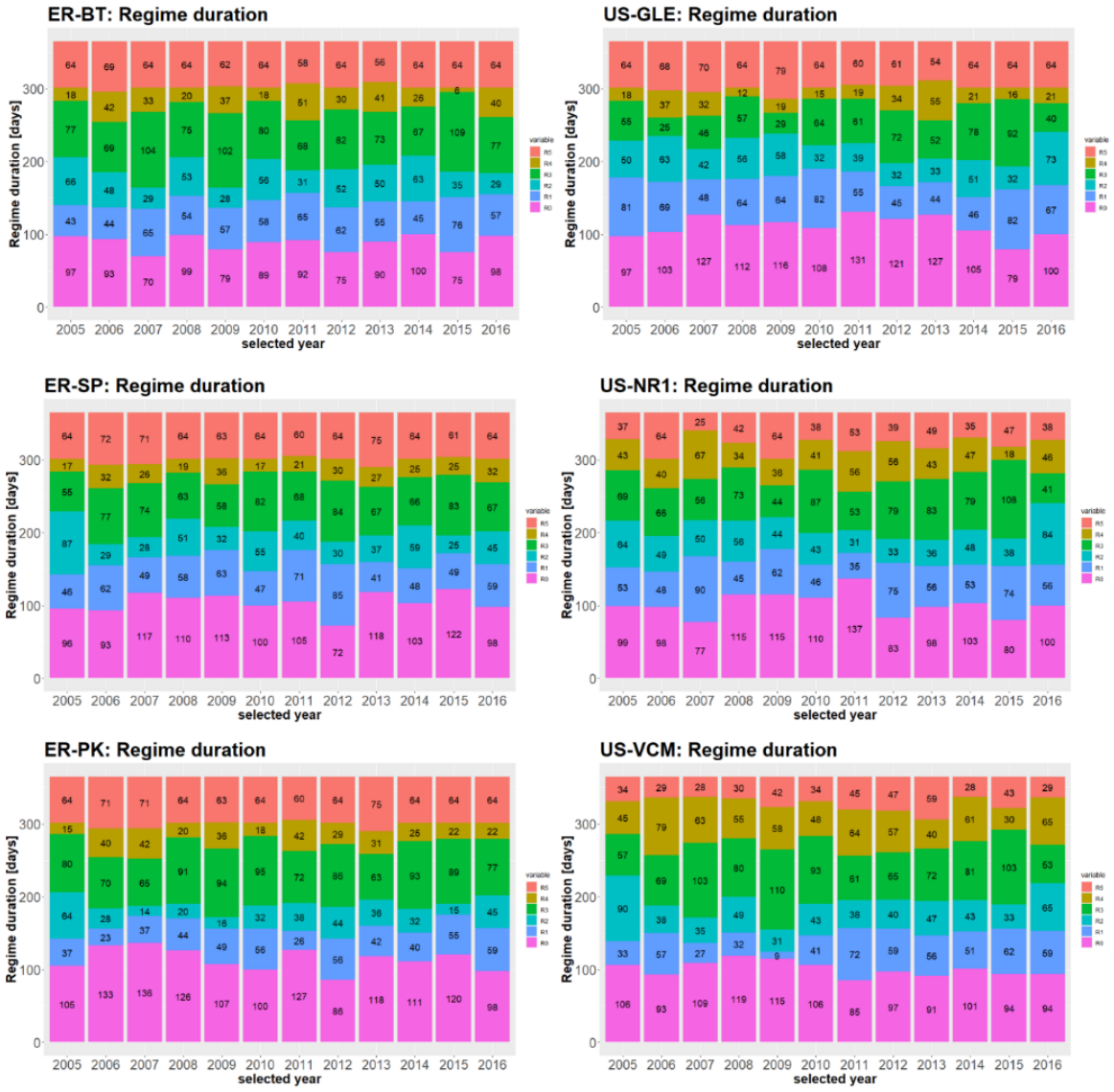

Figure E.1 Temporal distribution of hydroclimate regimes at the six sites between 2005 and 2016

Bibliography

Abatzoglou, J. T., Barbero, R., Wolf, J. W., & Holden, Z. A. (2014). Tracking Interannual Streamflow Variability with Drought Indices in the U.S. Pacific Northwest. *Journal of Hydrometeorology*. https://doi.org/10.1175/jhm-d-13-0167.1

Ai, J., Jia, G., Epstein, H. E., Wang, H., Zhang, A., & Hu, Y. (2018). MODIS-Based Estimates of Global Terrestrial Ecosystem Respiration. *Journal of Geophysical Research: Biogeosciences*, *123*(2), 326–352. https://doi.org/10.1002/2017JG004107

Akaike, H. (1974). A New Look at the Statistical Model Identification. *IEEE Transactions on Automatic Control*. https://doi.org/10.1109/TAC.1974.1100705

Allen, R. G., Pereira, L. S., Raes, D., & Smith, M. Crop evapotranspiration: Guidelines for computing crop requirements, Irrigation and Drainage Paper No. 56, FAO (1998). https://doi.org/10.1016/j.eja.2010.12.001

Anderson, M. C., Allen, R. G., Morse, A., & Kustas, W. P. (2012). Use of Landsat thermal imagery in monitoring evapotranspiration and managing water resources. *Remote Sensing of Environment*. https://doi.org/10.1016/j.rse.2011.08.025

Andrews, D. M., Lin, H., Zhu, Q., Jin, L., & Brantley, S. L. (2011). Hot spots and hot moments of dissolved organic carbon export and soil organic carbon storage in the shale hills catchment. *Vadose Zone Journal*, *10*(3), 943–954. https://doi.org/10.2136/vzj2010.0149

Arora, B., Dwivedi, D., Hubbard, S. S., Steefel, C. I., & Williams, K. H. (2016). Identifying geochemical hot moments and their controls on a contaminated river floodplain system using wavelet and entropy approaches. *Environmental Modelling and Software*, *85*, 27–41. https://doi.org/10.1016/j.envsoft.2016.08.005

Arora, B., Spycher, N. F., Steefel, C. I., Molins, S., Bill, M., Conrad, M. E., et al. (2016a). Influence of hydrological, biogeochemical and temperature transients on subsurface carbon fluxes in a flood plain environment. *Biogeochemistry*, *127*(2–3), 367–396. https://doi.org/10.1007/s10533-016-0186-8

Arora, B., Spycher, N. F., Steefel, C. I., Molins, S., Bill, M., Conrad, M. E., et al. (2016b). Influence of hydrological, biogeochemical and temperature transients on subsurface carbon fluxes in a flood plain environment. *Biogeochemistry*, *127*(2–3), 367–396. https://doi.org/10.1007/s10533-016-0186-8

Arora, B., Briggs, M. A., Zarnetske, J., Stegen, J., Gomez-Valez, J., Dwivedi, D., & Steefel, C. (2020). *Hot Spots and Hot Moments in the Critical Zone: Identification of and Incorporation into Reactive Transport Models*. (A. Wymore, W. Yang, W. Silver, B. McDowell, & J. Chorover, Eds.). Biogeochemistry of the Critical Zone, Springer-Nature, Accepted.

Aulenbach, B. T., & Peters, N. E. (2018). Quantifying Climate-Related Interactions in Shallow and Deep Storage and Evapotranspiration in a Forested, Seasonally Water-Limited Watershed in the Southeastern United States. *Water Resources Research*, 1–25. https://doi.org/10.1002/2017WR020964

Avanzi, F., Rungee, J., Maurer, T., Bales, R., Ma, Q., Glaser, S., & Conklin, M. (2019). Evapotranspiration feedbacks shift annual precipitation-runoff relationships during multi-year droughts in a Mediterranean mixed rain-snow climate. *Hydrology and Earth System Sciences Discussions*, (August), 1–35. https://doi.org/10.5194/hess-2019-377

Baldocchi, D. (2014). Measuring fluxes of trace gases and energy between ecosystems and the atmosphere - the state and future of the eddy covariance method. *Global Change Biology*. https://doi.org/10.1111/gcb.12649

Baldocchi, D. D., Ma, S., Rambal, S., Misson, L., Ourcival, J. M., Limousin, J. M., et al. (2010). On the differential advantages of evergreenness and deciduousness in mediterranean oak woodlands: A flux perspective. *Ecological Applications*, *20*(6), 1583–1597. https://doi.org/10.1890/08-2047.1

Bao, C., Wu, H., Li, L., Newcomer, D., Long, P. E., & Williams, K. H. (2014). Uranium bioreduction rates across scales: Biogeochemical hot moments and hot spots during a biostimulation experiment at Rifle, Colorado. *Environmental Science and Technology*. https://doi.org/10.1021/es501060d

Baum, R., Bartram, J., & Hrudey, S. (2016). The Flint Water Crisis Confirms That U.S. Drinking Water Needs Improved Risk Management. *Environmental Science and Technology*, *50*(11), 5436–5437. https://doi.org/10.1021/acs.est.6b02238

Bellin, A., & Rubin, Y. (2004). On the use of peak concentration arrival times for the inference of hydrogeological parameters. *Water Resources Research*. https://doi.org/10.1029/2003WR002179

Bellin, A., Salandin, P., & Rinaldo, A. (1992). Simulation of dispersion in heterogeneous porous formations: Statistics, first-order theories, convergence of computations. *Water Resources Research*. https://doi.org/10.1029/92WR00578

Bellin, A., Rubin, Y., & Rinaldo, A. (1994). Eulerian-Lagrangian approach for modeling of flow and transport in heterogeneous geological formations. *Water Resources Research*, *30*(11), 2913–2924. https://doi.org/10.1029/94WR01489

Bernhardt, E. S., Blaszczak, J. R., Ficken, C. D., Fork, M. L., Kaiser, K. E., & Seybold, E. C. (2017). Control Points in Ecosystems: Moving Beyond the Hot Spot Hot Moment Concept. *Ecosystems*, *20*(4), 665–682. https://doi.org/10.1007/s10021-016-0103-y

Berryman, E. M., Vanderhoof, M. K., Bradford, J. B., Hawbaker, T. J., Henne, P. D., Burns, S. P., et al. (2018). Estimating Soil Respiration in a Subalpine Landscape Using Point, Terrain, Climate, and Greenness Data. *Journal of Geophysical Research: Biogeosciences*, *123*(10), 3231–3249. https://doi.org/10.1029/2018JG004613

Beven, K. J., & Kirkby, M. J. (1979). A physically based, variable contributing area model of basin hydrology. *Hydrological Sciences Bulletin*. https://doi.org/10.1080/02626667909491834

Biology, G. C., Biology, O., Science, E., Division, A. C., Center, N., & Research, A. (2002). Carbon sequestration in a high-elevation, subalpine forest. *Global Change Biology*, (October 2001), 459–478.

Blankinship, J. (2014). Water Resources Research. *Water Resources Research*, *50*, 1448–1456. https://doi.org/10.1002/2013WR014541.Received

Bodesheim, P., Jung, M., Gans, F., Mahecha, M. D., & Reichstein, M. (2018). Upscaled diurnal cycles of land-Atmosphere fluxes: A new global half-hourly data product. *Earth System Science Data*, *10*(3), 1327–1365. https://doi.org/10.5194/essd-10-1327-2018

Bohn, T. J., & Vivoni, E. R. (2016). Process-based characterization of evapotranspiration sources over the North American monsoon region. *Water Resources Research*. https://doi.org/10.1002/2015WR017934

Boulton, A. J. (2007). Hyporheic rehabilitation in rivers: Restoring vertical connectivity. *Freshwater Biology*, *52*(4), 632–650. https://doi.org/10.1111/j.1365-2427.2006.01710.x

Bracken, C., Rajagopalan, B., & Zagona, E. (2014). A hiddenMarkovmodel combined with climate indices formultidecadal streamflow simulation. *Water Resources Research*, *50*, 1–11. https://doi.org/10.1002/2014WR015567.Received

Bracken, C., Rajagopalan, B., & Woodhouse, C. (2016). A Bayesian hierarchical nonhomogeneous hidden Markov model for multisite streamflow reconstructions. *Water Resources Research*, *52*(10), 7837–7850. https://doi.org/10.1002/2016WR018887

Breshears, D. D., Cobb, N. S., Rich, P. M., Price, K. P., Allen, C. D., Balice, R. G., et al. (2005). Regional vegetation die-off in response to global-change-type drought. *Proceedings of the National Academy of Sciences of the United States of America*. https://doi.org/10.1073/pnas.0505734102

De Bruin, H. A. R. (1983). A model for the Priestley-Taylor parameter alpha. *Journal of Climate & Applied Meteorology*. https://doi.org/10.1175/1520-0450(1983)0222.0.CO;2

Budyko, M. I. (1961). The Heat Balance of the Earth's Surface. *Soviet Geography*, *2*(4), 3–13. https://doi.org/10.1080/00385417.1961.10770761

Bundt, M., Widmer, F., Pesaro, M., Zeyer, J., & Blaser, P. (2001a). Preferential flow paths: Biological "hot spots" in soils. *Soil Biology and Biochemistry*, *33*(6), 729–738. https://doi.org/10.1016/S0038-0717(00)00218-2

Bundt, M., Widmer, F., Pesaro, M., Zeyer, J., & Blaser, P. (2001b). Preferential flow paths: Biological "hot spots" in soils. *Soil Biology and Biochemistry*, *33*(6), 729–738. https://doi.org/10.1016/S0038-0717(00)00218-2

Carpenter, S. R., Booth, E. G., Gillon, S., Kucharik, C. J., Loheide, S., Mase, A. S., et al. (2015). Plausible futures of a social-ecological system: Yahara watershed, Wisconsin, USA. *Ecology and Society*. https://doi.org/10.5751/ES-07433-200210

Chen, J., Hubbard, S. S., & Williams, K. H. (2013). Data-driven approach to identify field-scale biogeochemical transitions using geochemical and geophysical data and hidden Markov models: Development and application at a uranium-contaminated aquifer. *Water Resources Research*, *49*(10), 6412–6424. https://doi.org/10.1002/wrcr.20524

Condon, L. E., & Maxwell, R. M. (2019). Simulating the sensitivity of evapotranspiration and streamflow to large-scale groundwater depletion. *Science Advances*, *5*(6). https://doi.org/10.1126/sciadv.aav4574

Copty, N., Rubin, Y., & Mavko, G. (1993). Geophysical-hydrological identification of field permeabilities through Bayesian updating. *Water Resources Research*, *29*(8), 2813–2825. https://doi.org/10.1029/93WR00745

Cox, P. M., Betts, R. A., Jones, C. D., Spall, S. A., & Totterdell, I. J. (2000). Acceleration of global warming due to carbon-cycle feedbacks in a coupled climate model. *Nature*. https://doi.org/10.1038/35041539

Cvetkovic, V., Shapiro, A. M., & Dagan, G. (1992). A solute flux approach to transport in heterogeneous formations: 2. Uncertainty analysis. *Water Resources Research*, *28*(5),

1377–1388. https://doi.org/10.1029/91WR03085
Cvetkovic, V. D., & Shapiro, A. M. (1990). Mass arrival of sorptive solute in heterogeneous porous media. *Water Resources Research*, *26*(9), 2057–2067. https://doi.org/10.1029/WR026i009p02057
Dagan, G., & Nguyen, V. (1989). A comparison of travel time and concentration approaches to modeling transport by groundwater. *Journal of Contaminant Hydrology*, *4*(1), 79–91. https://doi.org/10.1016/0169-7722(89)90027-2
Dagan, G. (1989). *Flow and Transport in Porous Formations.* Springer Verlag, Berlin.
Dagan, Gedeon. (1984). Solute transport in heterogeneous porous formations. *Journal of Fluid Mechanics*, *145*(2), 151–177. https://doi.org/10.1017/S0022112084002858
Dagan, Gedeon, & Rubin, Y. (1992). Conditional estimation of solute travel time in heterogeneous formations: Impact of transmissivity measurements. *Water Resources Research*, *28*(4), 1033–1040. Retrieved from http://www.agu.org/pubs/crossref/1992.../91WR02759.shtml
Daggers, T. D., Kromkamp, J. C., Herman, P. M. J., & van der Wal, D. (2018). A model to assess microphytobenthic primary production in tidal systems using satellite remote sensing. *Remote Sensing of Environment*, *211*(April), 129–145. https://doi.org/10.1016/j.rse.2018.03.037
Dempster, A. P., Laird, N. M., & Rubin, D. B. (1977). Maximum Likelihood from Incomplete Data via the EM Algorithm. *Journal of the Royal Statistical Society. Series B*, *39*(1), 1–38. https://doi.org/10.2307/2984875
Destouni, G., & Cvetkovic, V. (1991). Field scale mass arrival of sorptive solute into the groundwater. *Water Resources Research*, *27*(6), 1315–1325. https://doi.org/10.1029/91WR00182
Duncan, J. M., Groffman, P. M., & Band, L. E. (2013a). Towards closing the watershed nitrogen budget: Spatial and temporal scaling of denitrification. *Journal of Geophysical Research: Biogeosciences*, *118*(3), 1105–1119. https://doi.org/10.1002/jgrg.20090
Duncan, J. M., Groffman, P. M., & Band, L. E. (2013b). Towards closing the watershed nitrogen budget: Spatial and temporal scaling of denitrification. *Journal of Geophysical Research: Biogeosciences*, *118*(3), 1105–1119. https://doi.org/10.1002/jgrg.20090
Dwivedi, D. (2017). Hot Spots and Hot Moments of Nitrogen in a Riparian Corridor. *Water Resources Research*, 1–43. https://doi.org/10.1002/2017WR022346
Ernakovich, J. G., Hopping, K. A., Berdanier, A. B., Simpson, R. T., Kachergis, E. J., Steltzer, H., & Wallenstein, M. D. (2014). Predicted responses of arctic and alpine ecosystems to altered seasonality under climate change. *Global Change Biology*. https://doi.org/10.1111/gcb.12568
Ezzedine, S., & Rubin, Y. (1996). A geostatistical approach to the conditional estimation of spatially distributed solute concentration and notes on the use of tracer data in the inverse problem. *Water Resources Research*. https://doi.org/10.1029/95WR02285
Falco, N., Wainwright, H., Dafflon, B., Léger, E., Peterson, J., Steltzer, H., et al. (2019). *Investigating Microtopographic and Soil Controls on a Mountainous Meadow Plant Community Using High-Resolution Remote Sensing and Surface Geophysical Data*. *Journal of Geophysical Research: Biogeosciences*. https://doi.org/10.1029/2018JG004394
Fatichi, S., & Ivanov, V. Y. (2014). Interannual variability of evapotranspiration and vegetation productivity. *Water Resources Research*. https://doi.org/10.1002/2013WR015044
Fiori, A., & Jankovic, I. (2012). On Preferential Flow, Channeling and Connectivity in

Heterogeneous Porous Formations. *Mathematical Geosciences*, *44*(2), 133–145. https://doi.org/10.1007/s11004-011-9365-2

Foufoula-Georgiou, E., & Lettenmaier, D. P. (1987). A Markov Renewal Model for rainfall occurrences. *Water Resources Research*. https://doi.org/10.1029/WR023i005p00875

Frank, J. M., Massman, W. J., Ewers, B. E., Huckaby, L. S., & Negrón, J. F. (2014). Tree Mortality From Spruce Bark Beetles. *Journal of Geophysical Research: Biogeosciences*, *119*(6), 1195–1215. https://doi.org/10.1002/2013JG002597.Received

Frei, S., Knorr, K. H., Peiffer, S., & Fleckenstein, J. H. (2012). Surface micro-topography causes hot spots of biogeochemical activity in wetland systems: A virtual modeling experiment. *Journal of Geophysical Research: Biogeosciences*, *117*(4), 1–18. https://doi.org/10.1029/2012JG002012

Gao, X., Mei, X., Gu, F., Hao, W., Li, H., & Gong, D. (2017). Ecosystem respiration and its components in a rainfed spring maize cropland in the Loess Plateau, China. *Scientific Reports*. https://doi.org/10.1038/s41598-017-17866-1

Gao, Y., Yu, G., Li, S., Yan, H., Zhu, X., Wang, Q., et al. (2015). A remote sensing model to estimate ecosystem respiration in Northern China and the Tibetan Plateau. *Ecological Modelling*. https://doi.org/10.1016/j.ecolmodel.2015.03.001

Godsey, S. E., Kirchner, J. W., & Tague, C. L. (2014). Effects of changes in winter snowpacks on summer low flows: Case studies in the Sierra Nevada, California, USA. *Hydrological Processes*, *28*(19), 5048–5064. https://doi.org/10.1002/hyp.9943

van Gorsel, E., Delpierre, N., Leuning, R., Black, A., Munger, J. W., Wofsy, S., et al. (2009). Estimating nocturnal ecosystem respiration from the vertical turbulent flux and change in storage of CO 2. *Agricultural and Forest Meteorology*, *149*(11), 1919–1930. https://doi.org/10.1016/j.agrformet.2009.06.020

Greve, P., Gudmundsson, L., Orlowsky, B., & Seneviratne, S. I. (2015). Introducing a probabilistic Budyko framework. *Geophysical Research Letters*, *42*(7), 2261–2269. https://doi.org/10.1002/2015GL063449

Gu, C., Anderson, W., & Maggi, F. (2012). Riparian biogeochemical hot moments induced by stream fluctuations. *Water Resources Research*, *48*(9), 1–17. https://doi.org/10.1029/2011WR011720

Hargrove, W. W., & Hoffman, F. M. (1999). Using multivariate clustering to characterize ecoregion borders. *Computing in Science and Engineering*, *1*(4), 18–25. https://doi.org/10.1109/5992.774837

Hargrove, W. W., Hoffman, F. M., & Law, B. E. (2003). New analysis reveals representativeness of the amerflux network. *Eos*, *84*(48). https://doi.org/10.1029/2003EO480001

Harken, B., Chang, C. F., Dietrich, P., Kalbacher, T., & Rubin, Y. (2019). Hydrogeological Modeling and Water Resources Management: Improving the Link Between Data, Prediction, and Decision Making. *Water Resources Research*. https://doi.org/10.1029/2019WR025227

Harms, T. K., & Grimm, N. B. (2008). Hot spots and hot moments of carbon and nitrogen dynamics in a semiarid riparian zone. *Journal of Geophysical Research: Biogeosciences*, *113*(G1), n/a-n/a. https://doi.org/10.1029/2007JG000588

Harpold, A., & Molotch, N. P. (2015). Sensitivity of Soil Water Availability to Changing. *Geophysical Research Letters*, *42*(October), 8011–8020. https://doi.org/10.1002/2015GL065855

Henri, C. V., Fernàndez-Garcia, D., & de Barros, F. P. J. (2015). Probabilistic human health risk assessment of degradation-related chemical mixtures in heterogeneous aquifers: Risk

statistics, hot spots, and preferential channels. *Water Resources Research*, *51*(6), 4086–4108. https://doi.org/10.1002/2014WR016717

Hill, A. R., Devito, K. J., & Campagnolo, S. (2000). Subsurface Denitrification in a Forest Riparian Zone : Interactions between Hydrology and Supplies of Nitrate and Organic Carbon Author (s): Alan R . Hill , Kevin J . Devito , S . Campagnolo and K . Sanmugadas Published by : Springer Stable URL : http:/, *51*(2), 193–223.

Hochreiter, S., & Schmidhuber, J. (1997). Long Short-Term Memory. *Neural Computation*. https://doi.org/10.1162/neco.1997.9.8.1735

Homer, C., Dewitz, J., Yang, L., Jin, S., Danielson, P., Xian, G., et al. (2015). Completion of the 2011 national land cover database for the conterminous United States – Representing a decade of land cover change information. *Photogrammetric Engineering and Remote Sensing*. https://doi.org/10.1016/S0099-1112(15)30100-2

Hu, J., Moore, D. J. P., Burns, S. P., & Monson, R. (2010). Longer growing seasons lead to less carbon sequestration by a subalpine forest. *Global Change Biology*, *16*(2), 771–783. https://doi.org/10.1111/j.1365-2486.2009.01967.x

Hu, Z., Wang, G., Sun, X., Zhu, M., Song, C., Huang, K., & Chen, X. (2018). Spatial-Temporal Patterns of Evapotranspiration Along an Elevation Gradient on Mount Gongga, Southwest China. *Water Resources Research*. https://doi.org/10.1029/2018WR022645

Hubbard, S. S., Rubin, Y., & Majer, E. (1997). Ground-penetrating-radar-assisted saturation and permeability estimation in bimodal systems. *Water Resources Research*, *33*(5), 971–990. https://doi.org/10.1029/96WR03979

Hubbard, S. S., Williams, K. H., Agarwal, D., Banfield, J., Beller, H., Bouskill, N., et al. (2018). The East River, Colorado, Watershed: A Mountainous Community Testbed for Improving Predictive Understanding of Multiscale Hydrological–Biogeochemical Dynamics. *Vadose Zone Journal*, *17*(1), 0. https://doi.org/10.2136/vzj2018.03.0061

Immerzeel, W. W., Lutz, A. F., Andrade, M., Bahl, A., Biemans, H., Bolch, T., et al. (2019). Importance and vulnerability of the world ' s water towers. *Nature (in Press)*, *577*(May 2019), 1–43. https://doi.org/10.1038/s41586-019-1822-y

IPCC. (2019). IPCC 2019- Special report on climate change, desertification, land degradation, sustainable land management, food security, and greenhouse gas fluxes in terrestrial ecosystem. *Research Handbook on Climate Change and Agricultural Law*. https://doi.org/10.4337/9781784710644

Irons, J. R., Dwyer, J. L., & Barsi, J. A. (2012). The next Landsat satellite: The Landsat Data Continuity Mission. *Remote Sensing of Environment*. https://doi.org/10.1016/j.rse.2011.08.026

Jägermeyr, J., Gerten, D., Lucht, W., Hostert, P., Migliavacca, M., & Nemani, R. (2014). A high-resolution approach to estimating ecosystem respiration at continental scales using operational satellite data. *Global Change Biology*. https://doi.org/10.1111/gcb.12443

James, T., Evans, A., Madly, E., & Kelly, C. (2014). The economic importance of the Colorado River to the Basin region. *L William Seidman Research Institute, W. P. Carey School of Business, Arizona State University*.

Jasechko, S., Kirchner, J. W., Welker, J. M., & McDonnell, J. J. (2016). Substantial proportion of global streamflow less than three months old. *Nature Geoscience*, *9*(2), 126–129. https://doi.org/10.1038/ngeo2636

Jonas, T., Rixen, C., Sturm, M., & Stoeckli, V. (2008). How alpine plant growth is linked to snow cover and climate variability. *Journal of Geophysical Research: Biogeosciences*,

113(3), 1–10. https://doi.org/10.1029/2007JG000680

Jung, M., Reichstein, M., Ciais, P., Seneviratne, S. I., Sheffield, J., Goulden, M. L., et al. (2010). Recent decline in the global land evapotranspiration trend due to limited moisture supply. *Nature*. https://doi.org/10.1038/nature09396

Jung, M., Reichstein, M., Schwalm, C. R., Huntingford, C., Sitch, S., Ahlström, A., et al. (2017). Compensatory water effects link yearly global land CO 2 sink changes to temperature. *Nature*, *541*(7638), 516–520. https://doi.org/10.1038/nature20780

Kamidaira, Y., Uchiyama, Y., Kawamura, H., Kobayashi, T., & Furuno, A. (2018). Submesoscale Mixing on Initial Dilution of Radionuclides Released From the Fukushima Daiichi Nuclear Power Plant. *Journal of Geophysical Research: Oceans*, *123*(4), 2808–2828. https://doi.org/10.1002/2017JC013359

Kampf, S., Markus, J., Heath, J., & Moore, C. (2015). Snowmelt runoff and soil moisture dynamics on steep subalpine hillslopes. *Hydrological Processes*, *29*(5), 712–723. https://doi.org/10.1002/hyp.10179

Keenan, T. F., Migliavacca, M., Papale, D., Baldocchi, D., Reichstein, M., Torn, M., & Wutzler, T. (2019). Widespread inhibition of daytime ecosystem respiration. *Nature Ecology and Evolution*, *3*(3), 407–415. https://doi.org/10.1038/s41559-019-0809-2

Knowles, J. F., Burns, S. P., Blanken, P. D., & Monson, R. K. (2015). Fluxes of energy, water, and carbon dioxide from mountain ecosystems at Niwot Ridge, Colorado. *Plant Ecology and Diversity*. https://doi.org/10.1080/17550874.2014.904950

Knowles, J. F., Blanken, P. D., & Williams, M. W. (2016). Wet meadow ecosystems contribute the majority of overwinter soil respiration from snow-scoured alpine tundra. *Journal of Geophysical Research G: Biogeosciences*, *121*(4), 1118–1130. https://doi.org/10.1002/2015JG003081

Kratzert, F., Klotz, D., Brenner, C., Schulz, K., & Herrnegger, M. (2018). Rainfall–runoff modelling using Long Short-Term Memory (LSTM) networks. *Hydrology and Earth System Sciences*, *22*(11), 6005–6022. https://doi.org/10.5194/hess-22-6005-2018

Kratzert, F., Klotz, D., Herrnegger, M., Sampson, A. K., Hochreiter, S., & Nearing, G. S. (2019). Toward Improved Predictions in Ungauged Basins: Exploiting the Power of Machine Learning. *Water Resources Research*. https://doi.org/10.1029/2019WR026065

Krause, S., Lewandowski, J., Grimm, N. B., Hannah, D. M., Pinay, G., McDonald, K., et al. (2017). Ecohydrological interfaces as hot spots of ecosystem processes. *Water Resources Research*. https://doi.org/10.1002/2016WR019516

Kuzyakov, Y., & Blagodatskaya, E. (2015). Microbial hotspots and hot moments in soil: Concept & review. *Soil Biology and Biochemistry*, *83*, 184–199. https://doi.org/10.1016/j.soilbio.2015.01.025

Lasslop, G., Reichstein, M., Papale, D., Richardson, A., Arneth, A., Barr, A., et al. (2010). Separation of net ecosystem exchange into assimilation and respiration using a light response curve approach: Critical issues and global evaluation. *Global Change Biology*, *16*(1), 187–208. https://doi.org/10.1111/j.1365-2486.2009.02041.x

Li, L., Steefel, C. I., Kowalsky, M. B., Englert, A., & Hubbard, S. S. (2010). Effects of physical and geochemical heterogeneities on mineral transformation and biomass accumulation during biostimulation experiments at Rifle, Colorado. *Journal of Contaminant Hydrology*, *112*(1–4), 45–63. https://doi.org/10.1016/j.jconhyd.2009.10.006

Livingston, G. P., & Hutchinson, G. L. (1995). *Enclosure-based measurement of trace gas exchange: applications and sources of error*. *Biogenic Trace Gases: Measuring Emissions*

from Soil and Water.

Loschko, M., Woehling, T., Rudolph, D. L., & Cirpka, O. A. (2016). Cumulative relative reactivity: A concept for modeling aquifer-scale reactive transport. *Water Resources Research*, *52*(10), 8117–8137. https://doi.org/10.1002/2016WR019080

M Foster, L., A Bearup, L., P Molotch, N., D Brooks, P., & M Maxwell, R. (2016). Energy budget increases reduce mean streamflow more than snow-rain transitions: Using integrated modeling to isolate climate change impacts on Rocky Mountain hydrology. *Environmental Research Letters*. https://doi.org/10.1088/1748-9326/11/4/044015

Ma, Y., Liu, S., Song, L., Xu, Z., Liu, Y., Xu, T., & Zhu, Z. (2018). Estimation of daily evapotranspiration and irrigation water efficiency at a Landsat-like scale for an arid irrigation area using multi-source remote sensing data. *Remote Sensing of Environment*, *216*(August), 715–734. https://doi.org/10.1016/j.rse.2018.07.019

Maxwell, R. M., Kastenberg, W. E., & Rubin, Y. (1999). A methodology to integrate site characterization information into groundwater-driven health risk assessment. *Water Resources Research*. https://doi.org/10.1029/1999WR900103

McCabe, M. F., Aragon, B., Houborg, R., & Mascaro, J. (2017). CubeSats in Hydrology: Ultrahigh-Resolution Insights Into Vegetation Dynamics and Terrestrial Evaporation. *Water Resources Research*, *53*(12), 10017–10024. https://doi.org/10.1002/2017WR022240

McClain, M. E., Boyer, E. W., Dent, C. L., Gergel, S. E., Grimm, N. B., Groffman, P. M., et al. (2003). Biogeochemical Hot Spots and Hot Moments at the Interface of Terrestrial and Aquatic Ecosystems. *Ecosystems*. https://doi.org/10.1007/s10021-003-0161-9

Metzger, S., Junkermann, W., Mauder, M., Butterbach-Bahl, K., Trancón Y Widemann, B., Neidl, F., et al. (2013). Spatially explicit regionalization of airborne flux measurements using environmental response functions. *Biogeosciences*, *10*(4), 2193–2217. https://doi.org/10.5194/bg-10-2193-2013

Miall, A. D. (1985). Architectural-element analysis: A new method of facies analysis applied to fluvial deposits. *Earth Science Reviews*. https://doi.org/10.1016/0012-8252(85)90001-7

Miall, A. D. (1988). Facies Architecture in Clastic Sedimentary Basins. https://doi.org/10.1007/978-1-4612-3788-4_4

Migliavacca, M., Reichstein, M., Richardson, A. D., Mahecha, M. D., Cremonese, E., Delpierre, N., et al. (2015). Influence of physiological phenology on the seasonal pattern of ecosystem respiration in deciduous forests. *Global Change Biology*, *21*(1), 363–376. https://doi.org/10.1111/gcb.12671

Mitchell, C. P. J., Branfireun, B. A., & Kolka, R. K. (2008). Spatial characteristics of net methylmercury production hot spots in peatlands. *Environmental Science and Technology*, *42*(4), 1010–1016. https://doi.org/10.1021/es0704986

Mohanty, B. P., Cosh, M. H., Lakshmi, V., & Montzka, C. (2017). Soil moisture remote sensing: State-of-the-science. *Vadose Zone Journal*. https://doi.org/10.2136/vzj2016.10.0105

Moreno, L., & Tsang, C. -F. (1994). Flow channeling in strongly heterogeneous porous media: A numerical study. *Water Resources Research*. https://doi.org/10.1029/93WR02978

Morino, Y., Ohara, T., & Nishizawa, M. (2011). Atmospheric behavior, deposition, and budget of radioactive materials from the Fukushima Daiichi nuclear power plant in March 2011. *Geophysical Research Letters*, *38*(17), 1–7. https://doi.org/10.1029/2011GL048689

Mu, Q., Zhao, M., & Running, S. W. (2013). MODIS Global Terrestrial Evapotranspiration (ET) Product (MOD16A2/A3). *Algorithm Theoretical Basis Document*.

NASA. (2008). Moderate Resolution Imaging Spectroradiometer (MODIS) Overview.

Nelson, J. A., Carvalhais, N., Cuntz, M., Delpierre, N., Knauer, J., Ogée, J., et al. (2018). Coupling Water and Carbon Fluxes to Constrain Estimates of Transpiration: The TEA Algorithm. *Journal of Geophysical Research: Biogeosciences*, *123*(12), 3617–3632. https://doi.org/10.1029/2018JG004727

Ng, G., Bedford, D., & Miller, D. (2014). A mechanistic modeling and data assimilation framework for Mojave Desert ecohydrology. *Water Resources Research*, 4662–4685. https://doi.org/10.1002/2014WR015281.Received

Oleson, K. W., Lawrence, D. M., Bonan, G. B., Drewniak, B., Huang, M., Koven, C. D., et al. (2013). *Technical Description of version 4.5 of the Community Land Model (CLM)*. *NCAR Technical Note*. https://doi.org/10.5065/D6RR1W7M

Omernik, J. M. (2004). Perspectives on the nature and definition of ecological regions. *Environmental Management*. https://doi.org/10.1007/s00267-003-5197-2

Omernik, J. M., & Griffith, G. E. (2014). Ecoregions of the Conterminous United States: Evolution of a Hierarchical Spatial Framework. *Environmental Management*. https://doi.org/10.1007/s00267-014-0364-1

Oyler, J. W., Dobrowski, S. Z., Ballantyne, A. P., Klene, A. E., & Running, S. W. (2015a). Artificial amplification of warming trends across the mountains of the western United States. *Geophysical Research Letters*. https://doi.org/10.1002/2014GL062803

Oyler, J. W., Dobrowski, S. Z., Ballantyne, A. P., Klene, A. E., & Running, S. W. (2015b). Artificila amplification of warming trends across the mountains of the western United States. *Geophysical Research Letters*, 153–161. https://doi.org/10.1002/2014GL062803.Received

Paca, V. H. da M., Espinoza-Dávalos, G. E., Hessels, T. M., Moreira, D. M., Comair, G. F., & Bastiaanssen, W. G. M. (2019). The spatial variability of actual evapotranspiration across the Amazon River Basin based on remote sensing products validated with flux towers. *Ecological Processes*, *8*(1). https://doi.org/10.1186/s13717-019-0158-8

Pelletier, J. D., Barron-Gafford, G. A., Gutiérrez-Jurado, H., Hinckley, E. L. S., Istanbulluoglu, E., McGuire, L. A., et al. (2018). Which way do you lean? Using slope aspect variations to understand Critical Zone processes and feedbacks. *Earth Surface Processes and Landforms*. https://doi.org/10.1002/esp.4306

PRIESTLEY, C. H. B., & TAYLOR, R. J. (1972). On the Assessment of Surface Heat Flux and Evaporation Using Large-Scale Parameters. *Monthly Weather Review*. https://doi.org/10.1175/1520-0493(1972)100<0081:otaosh>2.3.co;2

Pumpanen, J., Kolari, P., Ilvesniemi, H., Minkkinen, K., Vesala, T., Niinistö, S., et al. (2004). Comparison of different chamber techniques for measuring soil CO 2 efflux. *Agricultural and Forest Meteorology*. https://doi.org/10.1016/j.agrformet.2003.12.001

Qiao, Z., Xu, X., Zhao, M., Wang, F., & Liu, L. (2016). The application of a binary division procedure to the classification of forest subcategories using MODIS time-series data during 2000–2010 in China. *International Journal of Remote Sensing*. https://doi.org/10.1080/01431161.2016.1176269

Rauscher, S. A., Pal, J. S., Diffenbaugh, N. S., & Benedetti, M. M. (2008). Future changes in snowmelt-driven runoff timing over the western US. *Geophysical Research Letters*. https://doi.org/10.1029/2008GL034424

Reichstein, M., Falge, E., Baldocchi, D., Papale, D., Aubinet, M., Berbigier, P., et al. (2005). On the separation of net ecosystem exchange into assimilation and ecosystem respiration: Review and improved algorithm. *Global Change Biology*. https://doi.org/10.1111/j.1365-2486.2005.001002.x

Reichstein, M., Camps-Valls, G., Stevens, B., Jung, M., Denzler, J., Carvalhais, N., & Prabhat. (2019). Deep learning and process understanding for data-driven Earth system science. *Nature*, *566*(7743), 195–204. https://doi.org/10.1038/s41586-019-0912-1

Ren, H., Cromwell, E., Kravitz, B., & Chen, X. (2019). Using Deep Learning to Fill Spatio-Temporal Data Gaps in Hydrological Monitoring Networks. *Hydrology and Earth System Sciences Discussions*, (May), 1–20. https://doi.org/10.5194/hess-2019-196

Ritzi, R. W., Dai, Z., Dominic, D. F., & Rubin, Y. N. (2004). Spatial correlation of permeability in cross-stratified sediment with hierarchical architecture. *Water Resources Research*. https://doi.org/10.1029/2003WR002420

Rood, S. B., Pan, J., Gill, K. M., Franks, C. G., Samuelson, G. M., & Shepherd, A. (2008). Declining summer flows of Rocky Mountain rivers: Changing seasonal hydrology and probable impacts on floodplain forests. *Journal of Hydrology*. https://doi.org/10.1016/j.jhydrol.2007.11.012

Rubin, Y. (2003). *Applied Stochastic Hydrogeology*. Oxford University Press, Oxford, UK.

Rubin, Y., Cushey, M. A., & Bellin, A. (1994). Modeling of transport in groundwater for environmental risk assessment. *Stochastic Hydrology and Hydraulics*. https://doi.org/10.1007/BF01581390

Rubin, Yoram. (1991a). Prediction of tracer plume migration in disordered porous media by the method of conditional probabilities. *Water Resources Research*. https://doi.org/10.1029/91WR00094

Rubin, Yoram. (1991b). The Spatial and Temporal Moments of Tracer Concentration in Disordered Porous Media. *Water Resources Research*. https://doi.org/10.1029/91WR01732

Rubin, Yoram. (1995). Flow and Transport in Bimodal Heterogeneous Formations. *Water Resources Research*. https://doi.org/10.1029/95WR01953

Rubin, Yoram, & Dagan, G. (1992). Conditional estimation of solute travel time in heterogeneous formations: Impact of transmissivity measurements. *Water Resources Research*. https://doi.org/10.1029/91WR02759

Rubin, Yoram, & Journel, A. G. (1991). Simulation of non-Gaussian space random functions for modeling transport in groundwater. *Water Resources Research*. https://doi.org/10.1029/91WR00838

Rubin, Yoram, Mavko, G., & Harris, J. (1992). Mapping permeability in heterogeneous aquifers using hydrologic and seismic data. *Water Resources Research*. https://doi.org/10.1029/92WR00154

Rungee, J., Bales, R., & Goulden, M. (2019). Evapotranspiration response to multiyear dry periods in the semiarid western United States. *Hydrological Processes*. https://doi.org/10.1002/hyp.13322

Ryu, Y., Baldocchi, D. D., Kobayashi, H., Van Ingen, C., Li, J., Black, T. A., et al. (2011). Integration of MODIS land and atmosphere products with a coupled-process model to estimate gross primary productivity and evapotranspiration from 1 km to global scales. *Global Biogeochemical Cycles*, *25*(4), 1–24. https://doi.org/10.1029/2011GB004053

Sassen, D. S., Hubbard, S. S., Bea, S. A., Chen, J., Spycher, N., & Denham, M. E. (2012). Reactive facies: An approach for parameterizing field-scale reactive transport models using geophysical methods. *Water Resources Research*, *48*(10). https://doi.org/10.1029/2011WR011047

Schiff, S. L., Devito, K. J., Elgood, R. J., McCrindle, P. M., Spoelstra, J., & Dillon, P. (2002). Two adjacent forested catchments: Dramatically different NO3− export. *Water*

Resour. Res., *38*(12), 1292. https://doi.org/10.1029/2000wr000170

Schimel, D., Kittel, T. G. F., Running, S., Monson, R., Turnipseed, A., & Anderson, D. (2002). Carbon sequestration studied in Western U.S. mountains. *Eos*. https://doi.org/10.1029/2002EO000314

Schwarz, G. (1978). Estimating the Dimension of a Model. *The Annals of Statistics*. https://doi.org/10.1214/aos/1176344136

Seneviratne, S. I., Lüthi, D., Litschi, M., & Schär, C. (2006). Land-atmosphere coupling and climate change in Europe. *Nature*. https://doi.org/10.1038/nature05095

Showstack, R. (2014). Fukushima Nuclear Accident Report Calls for More Focus on Threats From Extreme Events. *Eos, Transactions American Geophysical Union*, *95*(31), 279–279. https://doi.org/10.1002/2014eo310003

Shrestha, N. K., & Wang, J. (2018). Current and future hot-spots and hot-moments of nitrous oxide emission in a cold climate river basin. *Environmental Pollution*, *239*, 648–660. https://doi.org/10.1016/j.envpol.2018.04.068

Sloat, L. L., Henderson, A. N., Lamanna, C., & Enquist, B. J. (2015). The Effect of the Foresummer Drought on Carbon Exchange in Subalpine Meadows. *Ecosystems*, *18*(3), 533–545. https://doi.org/10.1007/s10021-015-9845-1

Sørensen, R., Zinko, U., & Seibert, J. (2006). On the calculation of the topographic wetness index: Evaluation of different methods based on field observations. *Hydrology and Earth System Sciences*. https://doi.org/10.5194/hess-10-101-2006

Speckman, H. N., Frank, J. M., Bradford, J. B., Miles, B. L., Massman, W. J., Parton, W. J., & Ryan, M. G. (2015). Forest ecosystem respiration estimated from eddy covariance and chamber measurements under high turbulence and substantial tree mortality from bark beetles. *Global Change Biology*. https://doi.org/10.1111/gcb.12731

Stocker, T. F., Qin, D., Plattner, G. K., Tignor, M. M. B., Allen, S. K., Boschung, J., et al. (2013). *Climate change 2013 the physical science basis: Working Group I contribution to the fifth assessment report of the intergovernmental panel on climate change*. *Climate Change 2013 the Physical Science Basis: Working Group I Contribution to the Fifth Assessment Report of the Intergovernmental Panel on Climate Change*. https://doi.org/10.1017/CBO9781107415324

Strachan, S., Kelsey, E. P., Brown, R. F., Dascalu, S., Harris, F., Kent, G., et al. (2016). Filling the Data Gaps in Mountain Climate Observatories Through Advanced Technology, Refined Instrument Siting, and a Focus on Gradients. *Mountain Research and Development*, *36*(4), 518–527. https://doi.org/10.1659/mrd-journal-d-16-00028.1

Suleau, M., Moureaux, C., Dufranne, D., Buysse, P., Bodson, B., Destain, J. P., et al. (2011). Respiration of three Belgian crops: Partitioning of total ecosystem respiration in its heterotrophic, above- and below-ground autotrophic components. *Agricultural and Forest Meteorology*. https://doi.org/10.1016/j.agrformet.2011.01.012

Teh, Y. A., Silver, W. L., Sonnentag, O., Detto, M., Kelly, M., & Baldocchi, D. D. (2011). Large Greenhouse Gas Emissions from a Temperate Peatland Pasture. *Ecosystems*, *14*(2), 311–325. https://doi.org/10.1007/s10021-011-9411-4

Teuling, A. J., Van Loon, A. F., Seneviratne, S. I., Lehner, I., Aubinet, M., Heinesch, B., et al. (2013). Evapotranspiration amplifies European summer drought. *Geophysical Research Letters*. https://doi.org/10.1002/grl.50495

Thornton, P. E., Thornton, M. M., Mayer, B. W., Wei, Y., Devarakonda, R., Vose, R. S., & Cook, R. B. (2017). Daymet: Daily Surface Weather Data on a 1-km Grid for North America,

Version 3.

Tran, A. P., Rungee, J., Faybishenko, B., Dafflon, B., & Hubbard, S. S. (2019). Assessment of spatiotemporal variability of evapotranspiration and its governing factors in a mountainous watershed. *Water (Switzerland), 11*(2). https://doi.org/10.3390/w11020243

Tukey, J. W. (1949). Comparing Individual Means in the Analysis of Variance. *Biometrics*. https://doi.org/10.2307/3001913

U.S. Environmental Protection Agency. (2003). Level III Ecoregions of the Continental United States. *Environmental Protection*.

USEPA. (2001). *Risk Assessment Guidance for Superfund*. *Office of Emergency and Remedial Response U.S. Environmental Protection Agency*.

Vidon, P., Allan, C., Burns, D., Duval, T. P., Gurwick, N., Inamdar, S., et al. (2010). Hot spots and hot moments in riparian zones: Potential for improved water quality management. *Journal of the American Water Resources Association*, *46*(2), 278–298. https://doi.org/10.1111/j.1752-1688.2010.00420.x

Visser, I., & Speekenbrink, M. (2010). depmixS4: An R Package for Hidden Markov Models. *Journal Of Statistical Software*, *36*(7), 1–21. https://doi.org/10.18637/jss.v036.i07

Viviroli, D., & Weingartner, R. (2008). "Water towers"—A global view of the hydrological importance of mountains. In *Advances in Global Change Research*. https://doi.org/10.1007/978-1-4020-6748-8_2

Viviroli, D., Dürr, H. H., Messerli, B., Meybeck, M., & Weingartner, R. (2007). Mountains of the world, water towers for humanity: Typology, mapping, and global significance. *Water Resources Research*, *43*(7), 1–13. https://doi.org/10.1029/2006WR005653

Voepel, H., Ruddell, B., Schumer, R., Troch, P. A., Brooks, P. D., Neal, A., et al. (2011). Quantifying the role of climate and landscape characteristics on hydrologic partitioning and vegetation response. *Water Resources Research*, *47*(8). https://doi.org/10.1029/2010WR009944

Vogelmann, J. E., Howard, S. M., Yang, L., Larson, C. R., Wylie, B. K., & Van Driel, N. (2001). Completion of the 1990s National Land Cover Data set for the conterminous United States from Landsat thematic mapper data and ancillary data sources. *Photogrammetric Engineering and Remote Sensing*.

Wainwright, H. M., Orozco, A. F., Bucker, M., Dafflon, B., Chen, J., Hubbard, S. S., & Williams, K. H. (2015). Hierarchical Bayesian method for mapping biogeochemical hot spots using induced polarization imaging. *Water Resources Research*, *51*, 9127–9140. https://doi.org/10.1002/2014WR016259

Wainwright, H. M., Steefel, C., Trutner, S. D., Henderson, A. N., Nikolopoulos, E. I., Wilmer, C. F., et al. (2020). Satellite-derived foresummer drought sensitivity of plant productivity in Rocky Mountain headwater catchments: spatial heterogeneity and geological-geomorphological control. *Environmental Research Letters*. https://doi.org/10.1088/1748-9326/ab8fd0

Wang, B., Zha, T. S., Jia, X., Wu, B., Zhang, Y. Q., & Qin, S. G. (2014). Soil moisture modifies the response of soil respiration to temperature in a desert shrub ecosystem. *Biogeosciences*, *11*(2), 259–268. https://doi.org/10.5194/bg-11-259-2014

Webb, R. W., Fassnacht, S. R., & Gooseff, M. N. (2018). Hydrologic flow path development varies by aspect during spring snowmelt in complex subalpine terrain. *Cryosphere*, *12*(1), 287–300. https://doi.org/10.5194/tc-12-287-2018

Wieder, W. R., Knowles, J. F., Blanken, P. D., Swenson, S. C., & Suding, K. N. (2017).

Ecosystem function in complex mountain terrain: Combining models and long-term observations to advance process-based understanding. *Journal of Geophysical Research: Biogeosciences*. https://doi.org/10.1002/2016JG003704

Williams, C. A., & Albertson, J. D. (2004). Soil moisture controls on canopy-scale water and carbon fluxes in an African savanna. *Water Resources Research*. https://doi.org/10.1029/2004WR003208

Wilson, A., & Rubin, Y. (2002). Characterization of aquifer heterogeneity using indicator variables for solute concentrations. *Water Resources Research*, *38*(12), 19-1-19–12. https://doi.org/10.1029/2000wr000116

Wilson, K. B., Hanson, P. J., Mulholland, P. J., Baldocchi, D. D., & Wullschleger, S. D. (2001). A comparison of methods for determining forest evapotranspiration and its components: Sap-flow, soil water budget, eddy covariance and catchment water balance. *Agricultural and Forest Meteorology*, *106*(2), 153–168. https://doi.org/10.1016/S0168-1923(00)00199-4

Xiao, J., Ollinger, S. V., Frolking, S., Hurtt, G. C., Hollinger, D. Y., Davis, K. J., et al. (2014). Data-driven diagnostics of terrestrial carbon dynamics over North America. *Agricultural and Forest Meteorology*. https://doi.org/10.1016/j.agrformet.2014.06.013

Xu, L., Baldocchi, D. D., & Tang, J. (2004). How soil moisture, rain pulses, and growth alter the response of ecosystem respiration to temperature. *Global Biogeochemical Cycles*, *18*(4), 1–10. https://doi.org/10.1029/2004GB002281

Xu, T., Guo, Z., Liu, S., He, X., Meng, Y., Xu, Z., et al. (2018). Evaluating Different Machine Learning Methods for Upscaling Evapotranspiration from Flux Towers to the Regional Scale. *Journal of Geophysical Research: Atmospheres*, *123*(16), 8674–8690. https://doi.org/10.1029/2018JD028447

Zeng, R., & Cai, X. (2015). Assessing the temporal variance of evapotranspiration considering climate and catchment storage factors. *Advances in Water Resources*, *79*, 51–60. https://doi.org/10.1016/j.advwatres.2015.02.008

Zeng, R., & Cai, X. (2016). Climatic and terrestrial storage control on evapotranspiration temporal variability: Analysis of river basins around the world. *Geophysical Research Letters*, *43*(1), 185–195. https://doi.org/10.1002/2015GL066470

Zhang, D., Liu, X., Zhang, Q., Liang, K., & Liu, C. (2016). Investigation of factors affecting intra-annual variability of evapotranspiration and streamflow under different climate conditions. *Journal of Hydrology*, *543*, 759–769. https://doi.org/10.1016/j.jhydrol.2016.10.047

Zhang, L., Potter, N., Hickel, K., Zhang, Y., & Shao, Q. (2008). Water balance modeling over variable time scales based on the Budyko framework - Model development and testing. *Journal of Hydrology*, *360*(1–4), 117–131. https://doi.org/10.1016/j.jhydrol.2008.07.021

Zhang, Y., Kong, D., Gan, R., Chiew, F. H. S., McVicar, T. R., Zhang, Q., & Yang, Y. (2019). Coupled estimation of 500 m and 8-day resolution global evapotranspiration and gross primary production in 2002–2017. *Remote Sensing of Environment*, *222*(May 2018), 165–182. https://doi.org/10.1016/j.rse.2018.12.031

Zucchini, W., & Guttorp, P. (1991). A Hidden Markov Model for Space-Time Precipitation. *Water Resources Research*, *27*(8), 1917–1923. https://doi.org/10.1029/91WR01403

Zucchini, W., & MacDonald, I. L. (2009). Hidden Markov Models for Time Series: An Introduction using R. *South African Actuarial Journal*, *10*(1), 265. https://doi.org/10.4314/saaj.v10i1.61717